

Field-Responsive ('Smart') Fluids for Advanced Automotive Applications

by

Suraj Sharadchandra Deshmukh

B.Tech., Chemical Engineering (2001)

Indian Institute of Technology, Bombay

Submitted to the Department of Mechanical Engineering  
in Partial Fulfillment of the Requirements for the Degree of  
Master of Science in Mechanical Engineering

at the

Massachusetts Institute of Technology

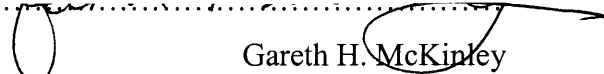
August 2003  
[September 2003]

© 2003 Massachusetts Institute of Technology  
All rights reserved

Signature of Author.....

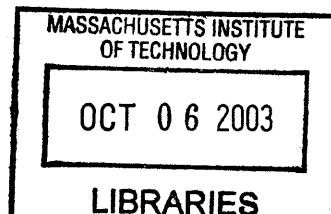
Department of Mechanical Engineering  
August 21, 2003

Certified by.....

  
Gareth H. McKinley  
Professor of Mechanical Engineering  
Thesis Supervisor

Accepted by.....

Ain A. Sonin  
Chairman, Department Committee on Graduate Students



ARCHIVES

# Field-Responsive ('Smart') Fluids for Advanced Automotive Applications

by

Suraj Sharadchandra Deshmukh

Submitted to the Department of Mechanical Engineering  
on August 21, 2003 in partial fulfillment of the  
requirements for the Degree of Master of Science in  
Mechanical Engineering

## ABSTRACT

Energy management is of vital concern in the automotive industry and many components need to satisfy stringent 'impact-safe' requirements. These energy absorption requirements conflict with the design demands for more compliant, thinner materials leading to a *conflict of stiffness* problem. A 'novel' energy absorbing material that adapts to environmental conditions and user specifications has been conceptualized, designed, modeled and tested in the present work. This adaptive energy absorbing material consists of an elastomeric foam impregnated with a field-responsive fluid such as a magnetorheological fluid or a shear-thickening fluid.

Stable and inexpensive magnetorheological (MR) fluids based on carbonyl iron powder have been synthesized in the laboratory. The rheological properties, including the field-dependent yield-stress, of the fluid have been measured at magnetic fields varying from 0.0 to 0.4 Tesla using a custom-built fixture for the AR 2000/ 1000N rheometers. Steady shear rheological experiments and transient creep tests have also been performed on a shear-thickening fluid consisting of 56% w/w corn-starch in water.

The large, reversible changes in the rheological behavior of field-responsive fluids have been utilized for controlling the stress-strain behavior and energy absorption characteristics of cellular solids. The mechanical properties of 'dry' and field-responsive fluid-impregnated cellular solids have been determined using Texture Analyzer modified with a custom-built attachment. Foams impregnated with MR fluids have shown a tremendous improvement in the energy-absorption capacity. The energy absorbed per unit volume at moderate magnetic fields ( $B \approx 0.2$  T) has been found to increase by 30 to 50 times as compared to the energy absorbed at zero-field.

A 'two-layer' scaling model has been proposed to explain the increase in the foam plateau stress based on an assumption that the MR fluid forms a secondary layer on the solid edges of the foam and determines the composite elastic modulus. Experiments have been carried out to determine the effect of control parameters such as the magnetic field, volume fraction of the fluid impregnating the foam and the strain rate on the mechanical

behavior of the composite. The magnetic field has been varied from 0.0 to 0.2 T, the volume fraction from 0% to 60% and the strain rate from 0.02 to 2.0 s<sup>-1</sup>. All the experimental data has been found to collapse onto a single master curve using appropriate shift factors based on the proposed theoretical model.

Impact testing using a 'drop-ball' test apparatus, built in-house, has been performed for a scaled down headrest model. Designs for an adaptive headrest and various automotive components have also been described in detail. The present work has thus presented a 'novel' class of conformable field-responsive fluid based composites that can be used for rapidly switching energy absorbing applications.

Thesis Supervisor: Gareth H. McKinley

Title: Professor of Mechanical Engineering

## **Acknowledgements**

I would like to express my deepest gratitude to my advisor, Prof. Gareth McKinley, for his expert guidance and constant encouragement. I have learned a lot from his vast knowledge and will always admire his friendly nature and witty humor.

This thesis would not have been possible without the support of my family and friends throughout these years. I am indebted to my friends who have made every moment of my life here exciting and precious.

I would like to thank the Non-Newtonian Fluids group for their invaluable suggestions and all the people at Hatsopoulos Microfluids Laboratory for making this lab such a fun place to be in. Finally, I would like to extend my sincere thanks to CC++ Media Labs, Lear Corporation and the Institute of Soldier Nanotechnology (ISN) for providing financial support.

# Table of Contents

<b>Abstract</b>	<b>2</b>
<b>Acknowledgements</b>	<b>4</b>
<b>Chapter 1 Introduction And Motivation</b>	<b>8</b>
1.1 BACKGROUND: ENERGY ABSORBING MATERIALS	8
1.2 MOTIVATION: ‘CONFLICT OF STIFFNESS’ PROBLEM	10
1.3 ADAPTIVE ENERGY-ABSORBING MATERIAL: CONCEPT AND CHALLENGES	14
<b>Chapter 2 Field – Responsive Fluids: Introduction And Literature Review</b>	<b>16</b>
2.1 MAGNETO- AND ELECTRO – RHEOLOGICAL FLUIDS	16
2.1.1 <i>Introduction</i>	16
2.1.2 <i>Composition</i>	16
2.1.3 <i>Properties</i>	18
2.1.4 <i>Polarization Model for Electrorheology / Magnetorheology</i>	21
2.1.5 <i>Testing Apparatus for ‘Smart’ Fluids: Shear Rheometer</i>	24
2.1.6 <i>Rheology of Field Responsive Fluids</i>	25
2.1.7 <i>Applications of Field-Responsive Fluids</i>	28
2.1.8 <i>Comparison of MR and ER fluids</i>	31
2.1.9 <i>Challenges for Field – Responsive Fluids</i>	32
2.2 SHEAR–THICKENING FLUIDS	33
2.2.1 <i>Description and Composition</i>	33
2.2.2 <i>Parameters Controlling Shear – Thickening</i>	34
2.2.3 <i>Mechanisms responsible for Shear – Thickening</i>	37
2.2.4 <i>Rheology and Viscoelasticity of Shear – Thickening Fluids</i>	40
2.2.5 <i>Applications of Shear – Thickening Fluids</i>	43
<b>Chapter 3 Cellular Solids: Review</b>	<b>44</b>
3.1 STRUCTURE AND PROPERTIES OF FOAMS	44

3.1.1	<i>Introduction and Cell Structure</i>	44
3.1.2	<i>Properties of Cellular Solids</i>	45
3.2	MECHANICS OF FOAMS	47
3.2.1	<i>Foams in Compression</i>	47
3.2.2	<i>Fluid-filled foams in compression</i>	49
3.2.3	<i>Energy absorption in Foams</i>	51
3.2.4	<i>Testing Apparatus for foams</i>	53
3.3	APPLICATIONS OF CELLULAR SOLIDS	55
<b>Chapter 4</b>	<b>Field-Responsive Fluids: Rheology And Characterization</b>	<b>56</b>
4.1	MAGNETORHEOLOGICAL FLUID RHEOLOGY	56
4.1.1	<i>Experimental setup</i>	56
4.1.2	<i>Steady shear rheology</i>	61
4.1.3	<i>Time-dependent rheology: Creep</i>	69
4.2	SHEAR-THICKENING FLUIDS	71
4.2.1	<i>Experimental Methods and Materials</i>	71
4.2.2	<i>Steady Shear Rheology</i>	72
4.2.3	<i>Time-dependent rheology: Creep</i>	74
4.3	SUMMARY	75
<b>Chapter 5</b>	<b>Fluid-Filled Cellular Solids: Mechanical Properties And Theoretical Modeling</b>	<b>76</b>
5.1	EXPERIMENTAL SETUP: MECHANICAL PROPERTIES	76
5.2	MECHANICAL PROPERTIES: DRY AND IMPREGNATED FOAMS	78
5.2.1	<i>Dry foams under compression</i>	78
5.2.2	<i>Foams Impregnated with Newtonian Fluids</i>	79
5.2.3	<i>Shear-thickening Fluid Impregnated Foam</i>	82
5.2.4	<i>Magnetorheological Fluid Impregnated Foam</i>	84
5.3	'NOVEL' ENERGY-ABSORBING MATERIAL: MRF IMPREGNATED FOAM	87
5.3.1	<i>Effect of Magnetic field strength</i>	88
5.3.2	<i>Effect of volume fraction of the MR fluid</i>	91
5.3.3	<i>Effects of strain-rate on mechanical properties</i>	93

5.4 THEORETICAL MODELING: PROPOSED SCALING MODEL	94
5.5 SUMMARY	102
<b>Chapter 6 Applications: Concept And Design</b>	<b>104</b>
6.1 APPLICATION POTENTIAL	104
6.2 IMPACT ABSORBING HEADREST	105
6.3 IMPACT TESTING: DROP BALL TEST APPARATUS	108
6.4 AUTOMOTIVE ENERGY MANAGEMENT STRUCTURES	112
6.5 SUMMARY	115
<b>Chapter 7 Conclusions And Future Work</b>	<b>116</b>
7.1 CONCLUSIONS	116
7.2 FUTURE WORK	120
<b>Bibliography</b>	<b>122</b>

# CHAPTER 1

## Introduction and Motivation

“Advanced materials are moving out of the lab and into the commercial world. Once regarded as laboratory curiosities, smart materials are beginning to make their mark on some high profile commercial applications” (*Quoted from ‘Feature Focus’ in Mechanical Engineering (2002)*).

### **1.1 Background: Energy Absorbing Materials**

Energy absorbing materials and structures are used in a number of applications ranging from vehicles, ballistic armor to helmets, sporting equipment and clothing. Such materials will shunt (divert and distribute the impact energy to sturdier areas), convert or dissipate energy via viscosity, friction, visco-elasticity or plasticity. Open or closed-cell foams, fibrous materials, springs or piston-cylinder arrangements are generally used as energy-absorbing structures.

Automobiles require a wide array of energy absorbing structures and a few of them are illustrated in figure 1.1. The seat backrest and headrest provide comfort to the passenger by absorbing small shock energies under normal driving conditions. The knee bolster located below the steering wheel absorbs impact from the passenger’s knee during a frontal crash. The A/B/C pillar trims (shown in green color in the figure) cushion the shock to the passenger head in a frontal or side car impact. Also, crumple zones or deliberate weak spots in strategic locations that collapse in a controlled manner during a crash to dissipate energy are shown in the figure.



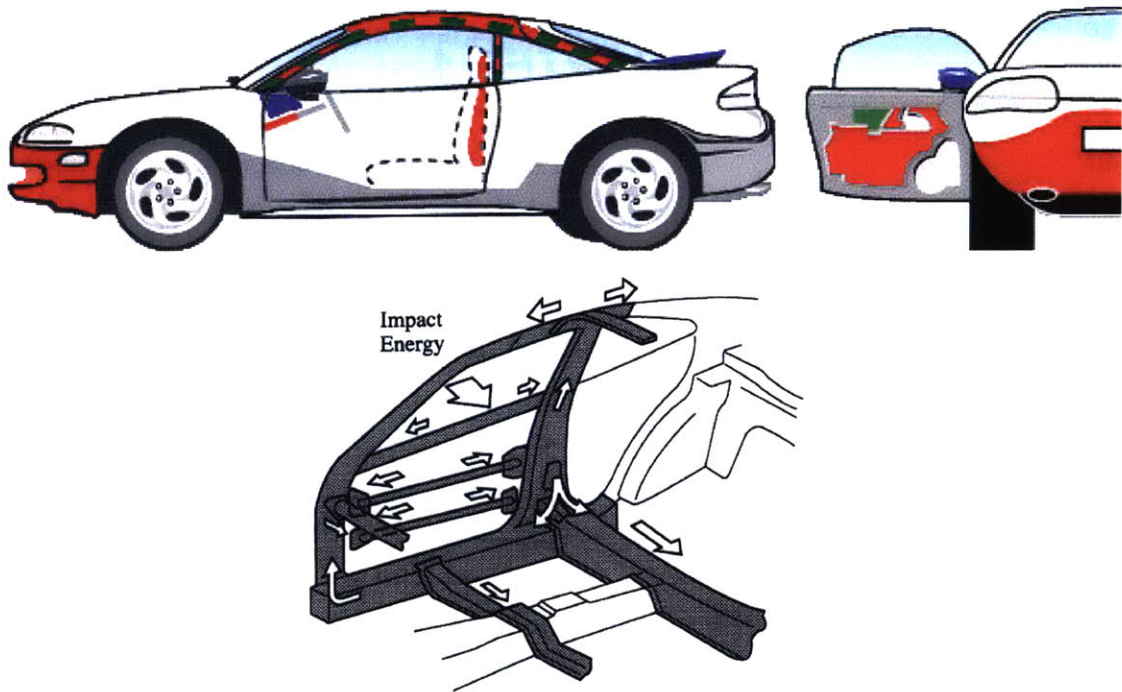


Figure 1.1 Examples of vehicle energy absorption structures like A/B/C pillar trims, headrest, seat backrest, knee bolsters, dampers, bumpers etc.

Thus, energy management in occupant protection components for vehicle and passenger safety is an important concern. As an example, NHTSA estimated that there were 805,851 occupants with whiplash injuries alone, annually between 1988 and 1996 in the United States resulting in a total annual cost of \$5.2 billion. Whiplash associated disorders are influenced mainly by seat and head-restraint properties and their positions with respect to the head and torso (Jakobsson *et al.*, 2000). The number and extent of injuries can be reduced by maximizing the amount of energy absorption, by minimizing the occupant acceleration or by reducing the relative movement between the head and the torso. Similarly, in side crashes, NHTSA simulation studies<sup>1</sup> have shown that structural stiffness and energy management through padding in doors or pillar trims can significantly reduce chest, head or pelvic injuries.

<sup>1</sup> <http://www.nhtsa.dot.gov/cars/rules/CrashWorthy/status9.html#13>

## **1.2 Motivation: 'Conflict of Stiffness' Problem**

The energy absorption capacity of the material is its defining characteristic and if it is too low the material “bottoms out” providing no additional protection or if it is too high, the force exerted exceeds the critical value beyond which it causes damage or injury. Thus, a more compliant material generates low forces and is comfortable but absorbs very little energy and vice versa indicating a trade-off in the optimal stiffness property of a given material. This is commonly referred to as the *conflict of stiffness* problem. Also bulkier, thicker materials will absorb more energy but this conflicts with design demands for slim, narrow structures. Further in accordance with new incoming legislations, due to European Experimental Vehicles Committee Working Group (EEVC WG 17) and European New Car Assessment Program (EURO NCAP), vehicle designs (exterior parts) need to minimize pedestrian injuries due to impact. The coincidence of the adult upper leg impact zone with the child head impact zone indicates again a “conflict of stiffness” problem (Courtney and Oyadiji 2001). Energy absorbing materials implemented previously usually meet either the child passenger impact criteria or the adult passenger impact criteria but not both sets of criteria (figure 1.2).

The Federal Motor Vehicle Safety Standard (FMVSS 201/202) further specifies special requirements for the interior parts of the vehicle such as A/B/C pillar trims, head-liners, knee and side impact foam parts. These impact parts are required to satisfy a number of energy absorption criteria under different impact conditions and constraints of interior/exterior space and design (Ullrich, 2003).

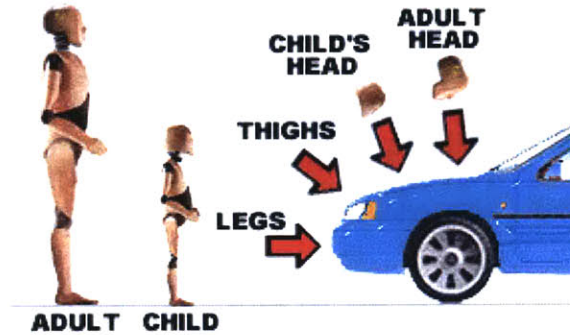


Figure 1.2 ‘Conflict of stiffness’ problem arising due to coincidence of the adult leg and the child head impact zone requiring varying degrees of energy absorption (<http://www.euroncap.com>).

A “conflict of stiffness” problem is evident in all the above cases and an adaptive structure that can be controlled to absorb varying amounts of energy depending on the impact conditions is required. Development of such a “smart” (externally adjustable or user-controllable) energy absorbing material has been the motivation behind this work.

Numerous studies and patents earlier have been concerned with the development of materials for energy management systems. As an example, U.S. Pat. Nos. 5,915,819, 5,564,535, 3,672,657 disclose a structure made of series of fluid-filled cells or reservoirs, wherein energy absorption is achieved through restriction to fluid-flow through orifices or in-between cells and reservoirs. A number of other devices disclose an energy absorbing pad or bladder with fluid-filled envelopes or compartments, for example, U.S. Pat. No. 5,545,128 utilizes a shear-thickening fluid-filled garment for bone fracture prevention. The major drawback in these devices is that there is no external adjustment to the amount of energy absorbed and the impact energy is simply shunted to another region due to incompressibility of fluid in compartments. Some attempts have been made to make an adaptive structure, like World Patent No. 09949236 that describes an energy absorbing material with permeable fluid-filled cells. The structure described in U.S. Pat. Nos. 5,915,819 is adaptive to a small extent as it has two states; either open or closed

cell state. This is realized by the use of pressure responsive seals, which convert the material from open to closed cell structure to absorb high levels of energy. However, none of these materials can be user-controlled to give desired energy management.

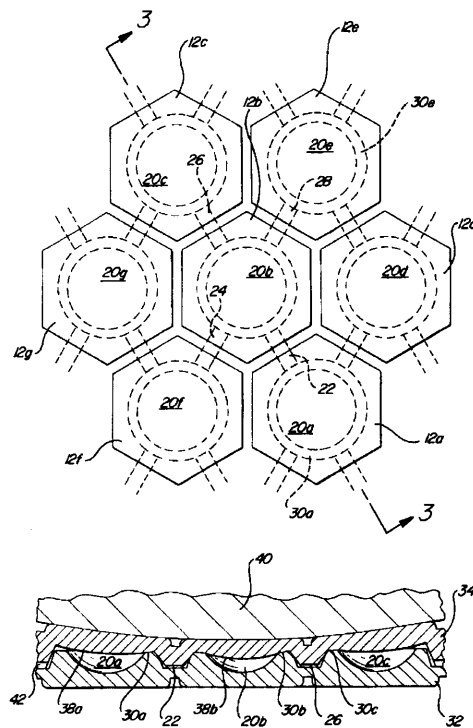
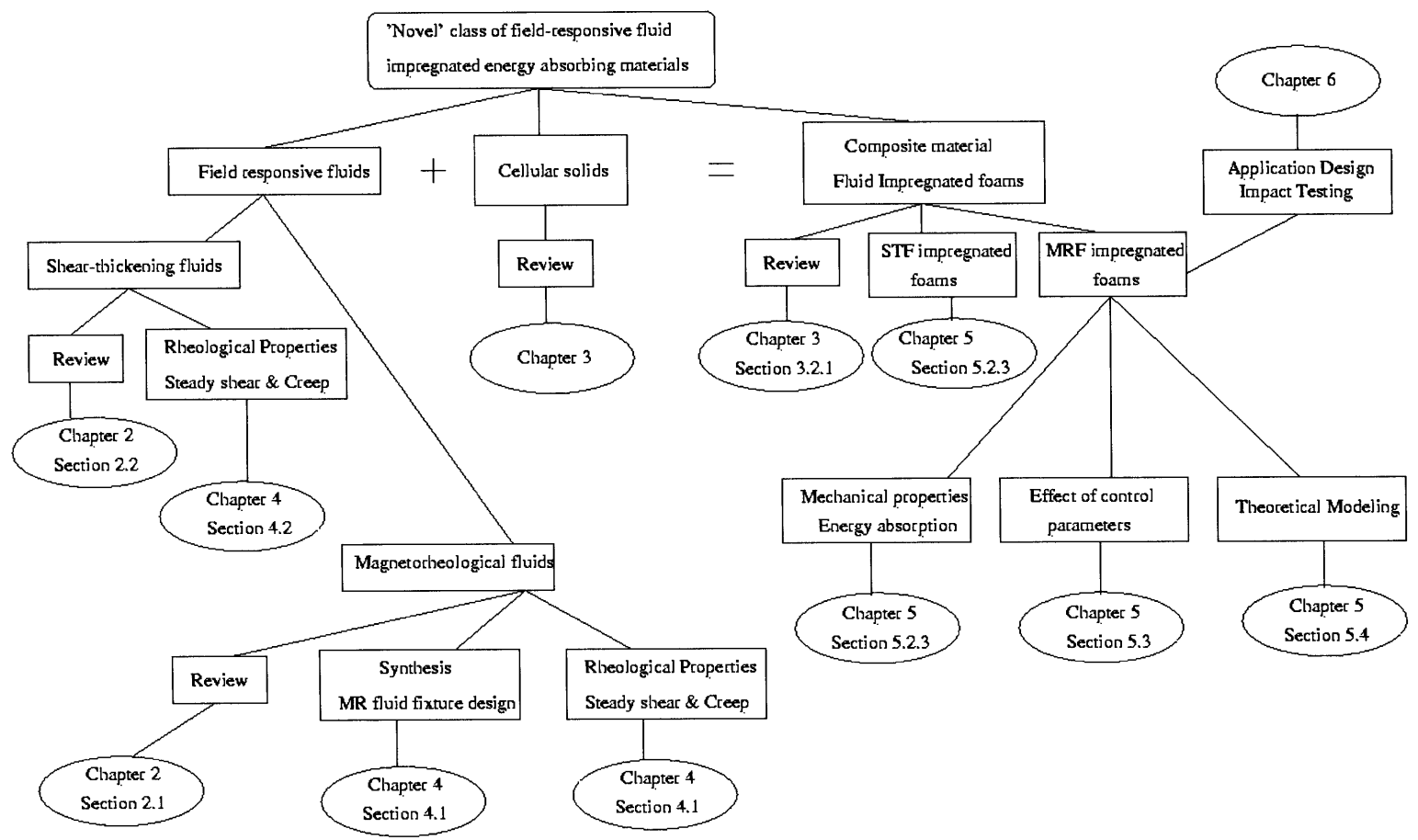


Figure 1.3 Adaptive energy absorbing structure consisting of a plurality of fluid-filled cells with pressure-responsive seals (*U.S. Pat. No. 5,915,819*).

Figure 1.4 Thesis organization flowchart



### **1.3 Adaptive Energy-absorbing Material: Concept and Challenges**

A fluid-solid composite as a possible solution to this problem has been envisaged, developed and studied extensively in this thesis. This energy absorbing material consists of a porous interconnected network of solid material forming edges and faces of cells such as an open-cell reticulated or closed-cell foam. The network structure can alternatively be formed from fibres or other cellular solids. The matrix is impregnated with a field responsive fluid such as a magneto- or electro- rheological fluid (Larson, 1999). Controlling and adjusting the external field in the vicinity of the material can then vary the energy absorbing properties of the fluid-solid composite.

A number of issues need to be resolved before commercial use of the material would be possible and many of them have been tackled in the present work, as shown in figure 1.4. The properties of the fluid as a function of the field determine the adaptive properties of the energy absorbing material. Hence, a review of earlier theories and experiments related to field-responsive fluids is presented in chapter 2. Results in rheology and testing of commercial and laboratory-synthesized fluids on a modified rheometer are reported and discussed in chapter 4.

A major limitation has been the cost of the commercially available fluid (\$600/ liter). Further, this fluid is prone to settling and has proprietary formulation techniques. A field-responsive fluid hence has been developed in the laboratory and is discussed in detail in chapter 4. Alternative field-responsive fluids like shear-thickening fluids could have a definite advantage for certain applications and conditions and hence, prior studies are reviewed in chapter 2 and results are reported in chapter 4.

Cellular solids form the base of the energy absorbing material and prior theory and mechanical properties of these materials are reviewed in chapter 3. Chapter 5 describes the development and characterization of the adaptive energy absorbing material. The energy

absorption capacity and other mechanical properties of the fluid-solid composite are a function of a number of control variables and experimental results illustrating their dependence are reported and discussed in chapter 5. The functional dependence of all these parameters can only be fully understood with a suitable model. Hence, a scaling model is also proposed and described in chapter 5. Finally, chapter 5 deals with the comparison of theoretical predictions and experimental results in the form of master plots using scaled or 'reduced' variables, which can be used for tuning the material according to the application requirements.

## CHAPTER 2

# Field – Responsive Fluids: Introduction and Literature Review

Field-responsive fluids (FRFs) may be characterized as materials that undergo large changes in their rheological (i.e. flow) properties such as viscosity, elasticity or plasticity in response to changes in magnetic, electric or stress fields.

### ***2.1 Magneto- and Electro – Rheological Fluids***

#### **2.1.1 Introduction**

Magnetorheological fluids ('MR fluids') belong to the class of so-called "smart" or controllable materials. They can reversibly change between a free-flowing liquid and semi-solid state within few tens of milliseconds in the presence of a magnetic field. These fluids have been the focus of many studies since they can provide a simple, rapid-response interface between electronic controls and mechanical systems. They were first discovered and developed by Jacob Rabinow (1948) at the US National Bureau of Standards. Electrorheological fluids ('ER' fluids) are electric field analogs of MR fluids and show rapid and large changes in their rheological behavior in response to an applied electric field. W. M. Winslow (1949) is credited with the initial development of ER fluids.

#### **2.1.2 Composition**

These field controllable fluids are typically 20–50 % by volume, suspensions of colloidal particles, usually 1-10 microns in size, in a carrier fluid like mineral oil, silicone oil, water,



glycerol etc. The colloidal particles are soft magnetic in case of MR fluids while in case of ER fluids they have a high dielectric constant and a suitable conductivity (e.g. alumina).

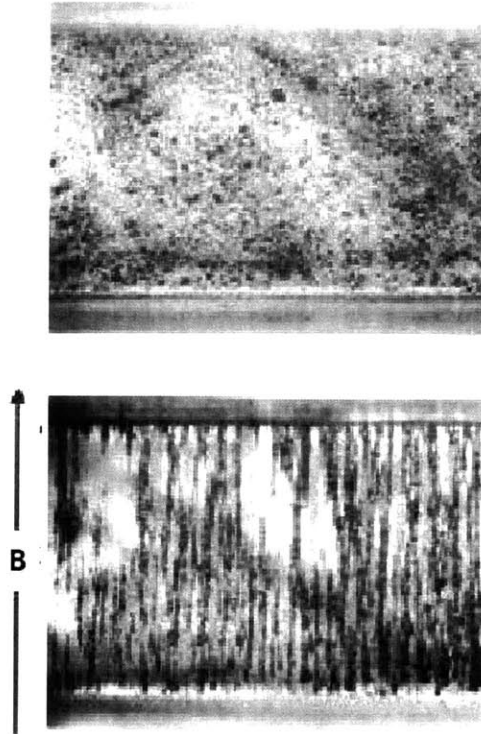


Figure 2.1 MR suspensions (2 vol%, 50  $\mu\text{m}$  dia. iron particles in silicone oil) before and after applying a magnetic field (Klingenberg 2001).

Mostly, carbonyl iron particles have been used in preparation of MR suspensions though other formulations using ferromagnetic or ferrimagnetic particles, like magnetite ( $\text{Fe}_3\text{O}_4$ ),  $\text{Fe}-\text{Co}$  alloy and  $\text{Ni}-\text{Zn}$  ferrites have also been described. Ferromagnetic materials exhibit a long-range ordering phenomenon at the atomic level, which causes the unpaired electron spins to line up parallel with each other in a region called a domain. Kormann *et al.* (1996) have studied magnetorheological fluids made of nanosized ferrite particles, which usually comprise a ferrofluid. MR fluids have also been made from superparamagnetic particles (e.g. polystyrene particles studded with nanometer size iron oxide inclusions) dispersed in a solvent (Fermigier and

Gast, 1992). Superparamagnetic particles are soft ferromagnetic or antiferromagnetic particles that do not possess any residual magnetization. A number of proprietary additives such as surfactants and thixotropic agents are added to promote stabilization of particles and enhance lubrication. Chin *et al.* (2001) have used nanosized ferromagnetic particles ( $Co-\gamma-Fe_2O_3$ ) and  $CrO_2$  particles to enhance dispersion stability. Nanostructured silica and surfactants like oleates, stearates have been added in earlier works for improving redispersibility (Phule and Ginder 1999, U.S. Patent No. 5,985,168). For improved stabilization of MR fluids against gravity, a viscoelastic medium having a low yield stress like grease has also been used as the continuous phase (Park *et al.* 2001). LORD Corp commercially produces numerous formulations of MR fluids using different types of carrier fluids<sup>1</sup>.

### 2.1.3 Properties

Normally, MR fluids are in the liquid state with the consistency (viscosity  $\sim 0.1-1$  Pa.s) of motor oil but when a magnetic field is applied, the soft magnetic particles acquire a dipole moment. The induced dipolar particles then align with the external field relative to the non-magnetized dispersed phase to form fibrous columns or aggregates as shown in figure 2.1. The columns need to be broken for the suspension to flow which gives rise to a yield stress (i.e. the magnitude of stress at which appreciable deformation takes place without any appreciable change in the stress (Barnes, 1999)) as a function of the magnetic flux density.

The Herschel -Bulkley viscoplastic model is often used to describe this yield stress and the non-newtonian behavior observed in FRFs, after yield, due to the presence of many additives

---

<sup>1</sup> <http://www.rheonetic.com>

$$\tau = \tau_0(B) + \eta \dot{\gamma} \quad \tau > \tau_0$$

$$\eta = k |\dot{\gamma}|^{n-1}$$
(1.1)

where  $\tau_0$  is the yield stress of the material,  $\eta$  is the viscosity,  $\dot{\gamma}$  is the shear rate,  $B$  is the magnetic field strength,  $k$  is the ‘consistency index’ and  $n$  is the power-law exponent.

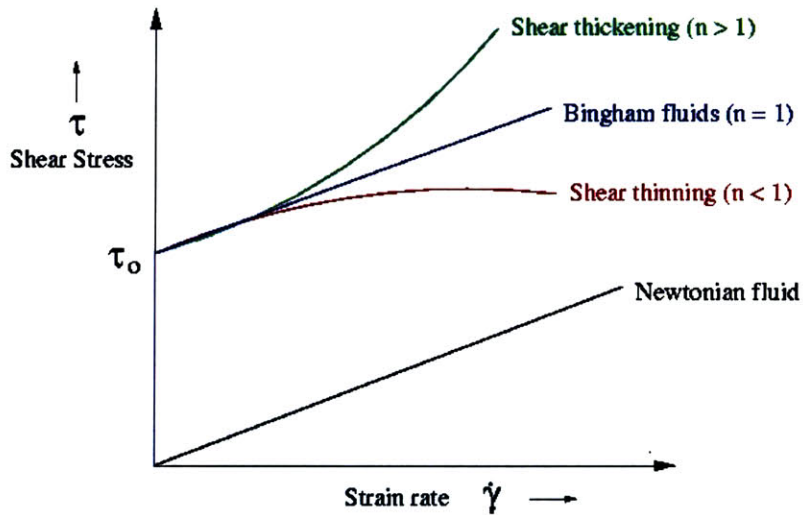


Figure 2.2 Herschel Bulkley viscoplastic model for Field-Responsive fluids where  $\tau_0$  is the yield stress at which the fluid starts flowing and the exponent  $n$  describes the non-Newtonian behavior observed after yield.

At small field strengths the field-induced yield stress is proportional to the square of magnetic flux density but becomes sub-quadratic with increasing field strength, as the particles tend to reach their saturation magnetization and is shown in figure 2.3.

The saturation magnetization is the maximum induced magnetic moment that can be obtained in a magnetic field. The magnetic properties of any material are represented by B-H curves and are described by the equation

$$B = \mu_0 \mu_r H \quad (1.2)$$

where  $B$  is the magnetic induction,  $H$  is the magnetic field,  $\mu_0$  is the permeability of free space and  $\mu_r$  is the relative permeability of the material.

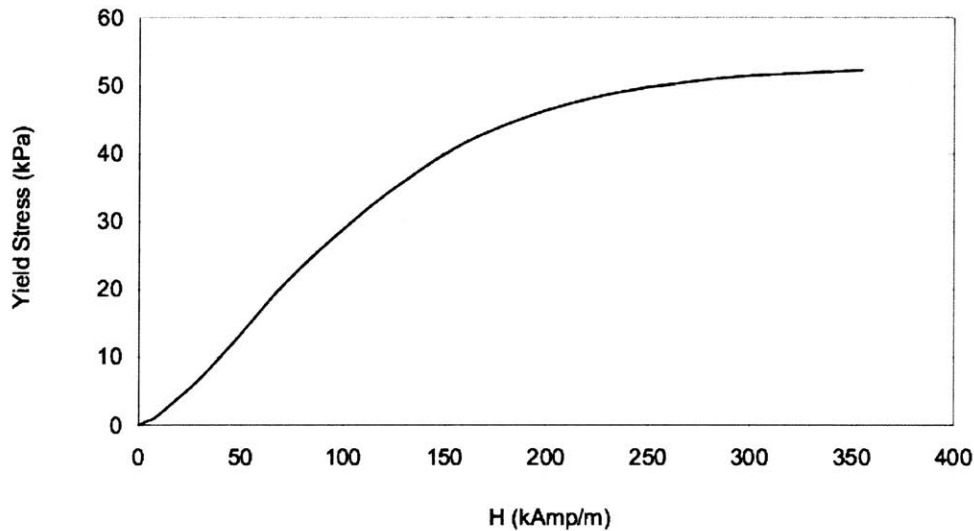


Figure 2.3 Graph showing the sub-quadratic dependence of yield stress on the magnetic field strength for Lord Corp.'s commercially available MR fluid, MRF – 336AG<sup>2</sup>.

Below the yield stress, the fluid shows viscoelastic behavior characterized by the linear viscoelastic properties  $G'$  and  $G''$ . Measurements show that at low frequencies the shear modulus  $G$  becomes constant. A more detailed discussion of the rheological properties of these externally controllable fluids is presented in section 2.1.5. The response time of these fluids, as determined by the response time for the changes in rheological properties to occur, is of the order of a few milliseconds. The field-responsive fluids (FRFs) are thus some of the fastest responding smart materials.

<sup>2</sup> <http://www.rheonetic.com>

## 2.1.4 Polarization Model for Electrorheology / Magnetorheology

The chaining of particles, brought about by their polarization in the presence of a field, is responsible for the ‘smart’ properties of these fluids. This chaining occurs if there is a dielectric or a magnetization mismatch between the particles and the carrier liquid. The polarization model can, in principle, predict the aggregation dynamics and the associated yield stress. Electrostatic/magneto static, hydrodynamics, steric and Brownian forces are together used to compute the aggregation dynamics of these particles, which are themselves typically modeled as hard spheres (Larson, 1999).

The electrostatic force  $(\bar{F}_j^e)$  acting on a particle is obtained from the interaction potential  $(W_{ij}^e)$  between two particles  $i$  and  $j$  assuming a point-dipole approximation. This approximation is valid for widely separated particles and enables considerable simplifications

$$W_{ij}^e = -\left(\frac{4\pi\epsilon_0\epsilon_s u^2}{r_{ij}^3}\right)(3\cos^2\theta_{ij} - 1) \quad (1.3)$$

$$\bar{F}_{ij}^e = -\left(\frac{\partial W_{ij}^e}{\partial \bar{r}_i}\right) \quad \bar{F}_i^e = \sum_{i \neq j} \bar{F}_{ij}^e$$

where  $\bar{F}_j^e$  is the force on particle  $i$  produced by particle  $j$ ,  $u$  is the dipole moment of an isolated particle,  $\epsilon_0$  is the permittivity of the space,  $\epsilon_s$  is the permittivity of the suspending medium and  $\theta_{ij}$  is the angle between the field and the line joining the centers of mass of particles  $i$  and  $j$ .

The dipole moment  $\bar{u}$  of an isolated particle is given by the Clausius-Mossotti relationship as

$$\bar{u} = \beta a^3 \bar{E} \quad \beta = \frac{(\epsilon_r - 1)}{(\epsilon_r + 2)} \quad (1.4)$$

$$\bar{r}_j - \bar{r}_i = r_{ij} \hat{e}_r^{ij}$$

where  $\beta$  is the effective polarizability of the particle,  $\epsilon_r$  is the relative permittivity of the particle,  $a$  is the particle radius and  $\hat{e}_r^{ij}$  is a unit vector oriented parallel to the line joining the centers of the two spheres.

Magneto static forces in the case of MR fluids are determined in a similar manner from a magnetic interaction potential given by

$$W_{ij}^m = - \left( \frac{m^2}{4\pi\mu_0 r_{ij}^3} \right) (3 \cos^2 \theta_{ij} - 1) \quad (1.5)$$

$$\bar{m} = \frac{4}{3} \pi a^3 \mu_0 \chi \bar{H}$$

where  $\bar{m}$  is the magnetic dipole moment acquired by an isolated magnetizable particle of radius  $a$  in the presence of a magnetic field  $\bar{H}$ ,  $\chi$  is the magnetic susceptibility of the particles and  $\mu_0$  is the permeability of free space.

The particle evolution equation also considers a number of other important forces such as hydrodynamic forces, short-range repulsive forces (arising from phenomena such as Born repulsion, solvation forces or steric interactions), Brownian forces and colloidal forces (van der Waals' attraction, DLVO type electrostatic repulsion) (Parthasarthy and Klingenberg 1996). Aggregation phenomena of the particles can then be studied using simulation of this evolution equation. The structure and rheology of the field-responsive fluid is determined by the competition between all these forces and can be conveniently represented in the form of dimensionless groups as

$$\begin{aligned}
Mn &= \frac{\text{hydrodynamic forces}}{\text{electro/ magnetostatic forces}} \\
Mn_{erf} &= \frac{\eta_s \dot{\gamma}}{2\epsilon_0 \epsilon_s \beta^2 E_0^2} \quad Mn_{mrf} = \frac{9\eta_s \dot{\gamma}}{2\mu_0 \chi^2 H^2} \\
Pe &= \frac{\text{hydrodynamic forces}}{\text{brownian forces}} \quad Pe_{erf} = \frac{6\pi a^3 \eta_s \dot{\gamma}}{k_B T} = Pe_{mrf} \quad (1.6) \\
\lambda &= \frac{Pe}{Mn} = \frac{\text{electro/ magnetostatic forces}}{\text{brownian forces}} \\
\lambda &= \frac{4\pi\mu_0 \chi^2 a^3 H^2}{3k_B T}
\end{aligned}$$

where  $Mn$  is the Mason number,  $Pe$  is the Peclet number,  $\eta_s$  is the solvent viscosity and  $\dot{\gamma}$  is the shear rate .

Mason number ( $Mn$ ), which is the ratio of viscous to magnetic forces, governs the aggregation phenomena and the dynamics of field-induced dipolar chains. Peclet number ( $Pe$ ), which describes the relative importance of advection to diffusion, determines how fast the structure or the field induced chains form and if thermal motion causes them to deform or collapse. The parameter  $\lambda$  is independent of the shear rate ( $\dot{\gamma}$ ) and takes into account the change in the yield stress coming from magnetostatic forces due to Brownian motion. Brownian motion will not only prevent the particles from settling but also from forming aggregates and chains, hence reducing the yield stress. An increase in yield stress with particle size is thus evident at the cost of decreased stability of the suspensions (Lemaire *et al.* 1995). Magnetorheological fluids based on nanometer-sized particles have been proposed and studied, because of their increased stability, but with an order of magnitude smaller yield stress (Rosenfeld *et al.* 2002). An estimate of the yield stress for ER and MR fluids can be obtained from a balance of the hydrodynamic, Brownian and magnetostatic forces and is given as

$$\begin{aligned}\sigma_y^{erf} &\sim 18 f_m \phi \varepsilon_0 \varepsilon_s \beta^2 E^2 \\ \sigma_y^{mrf} &\sim \sqrt{6} \phi \mu_0 M_s^{0.5} H^{1.5}\end{aligned}\tag{1.7}$$

where  $\sigma_y$  is the yield stress,  $f_m$  is a dimensionless force equal to 0.057 in the point-dipole approximation and  $M_s$  is the saturation magnetization for the particles (Larson, 1999).

### 2.1.5 Testing Apparatus for ‘Smart’ Fluids: Shear Rheometer

Field-responsive fluids are characterized by their steady-shear and linear viscoelastic properties which can be determined using rheological and optical techniques. A number of instruments such as capillary viscometer, Couette viscometer, parallel-plate type rheometer or a cone and plate type rheometer are used to measure these desired material functions.

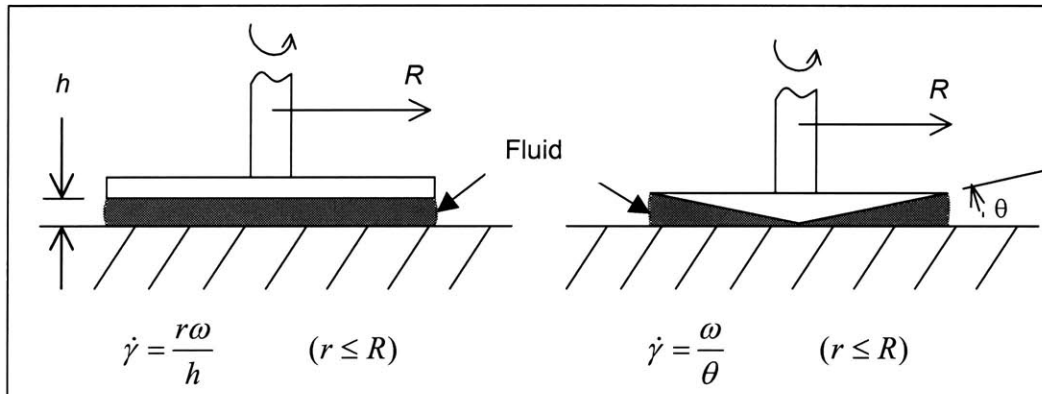


Figure 2.4 ‘Parallel-disk’ and a ‘Cone and Plate’ type arrangements used for determining material properties of complex fluids.

The two most widely used configurations are shown in figure 2.4, in which small volumes of fluid sample are tested between two coaxial circular parallel plates or between a small angle cone and plate, under shear, oscillatory or creep flows. A more detailed discussion relating the mechanical, or the measured quantities, with the desired material functions can be found in the treatise by Bird *et al.* (1987).



Rheological properties of MR fluids are also dependent on the magnetic field and custom-made or commercial attachments to standard rheometers have been used for this purpose. Li *et al.* (1999, 2002) have used a commercially available MR cell for the UDS 200 rheometer with parallel-plate geometry, which generates a magnetic field perpendicular to the shear direction. Rankin *et al.* (1999) used a Bohlin VOR rheometer modified by inserting the rheometer plate shafts through holes drilled into an electromagnetic iron yoke (figure 2.5). Helmholtz coils have been used by Cutillas *et al.* (1998) to generate a uniform but low strength magnetic field in the fluid sample space. Chin *et al.* (2001) have designed a solenoidal coil for creating a homogenous but weak magnetic field between the two plates of the rheometer. A MR fluid fixture has been custom-built in our laboratory for TA instruments' AR 2000/ 1000N rheometers in order to test fluids under high magnetic fields and is described in detail in section 4.1.1.

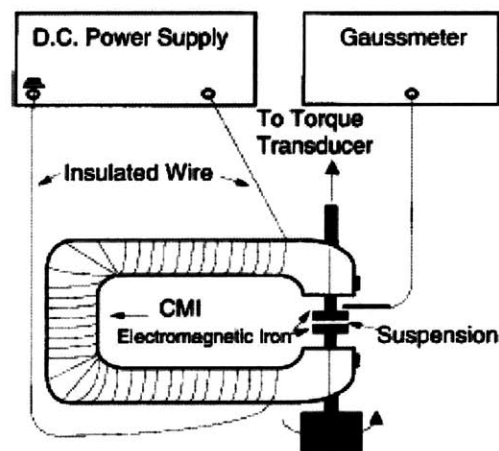


Figure 2.5 Schematic diagram of a Bohlin VOR rheometer modified using a iron yoke electromagnet (Rankin *et al.* 1999).

## 2.1.6 Rheology of Field Responsive Fluids

MR fluids in their 'off-state' (i.e. zero magnetic field) appear similar to oils or paint in consistency (0.1-1.0 Pa.s) and develop a yield stress in the presence of a magnetic field as

discussed in earlier sections. The yield stress is a function of the applied magnetic field and can be increased up to  $\sim 120$  kPa for micron size particles. Tang *et al.* (2000) have observed a yield stress of 800 kPa under enhanced structures obtained by compressing the MR fluid along the field direction. Compression of field-induced dipolar chains pushes them together to form thick columns that yield at stresses as high as 800 kPa. MR fluids have been studied extensively under steady shear flow and representative data is shown in figure 2.6. The dynamic yield stresses can be determined from such measurements by extrapolating to zero shear-rate (Genc and Phule 2002).

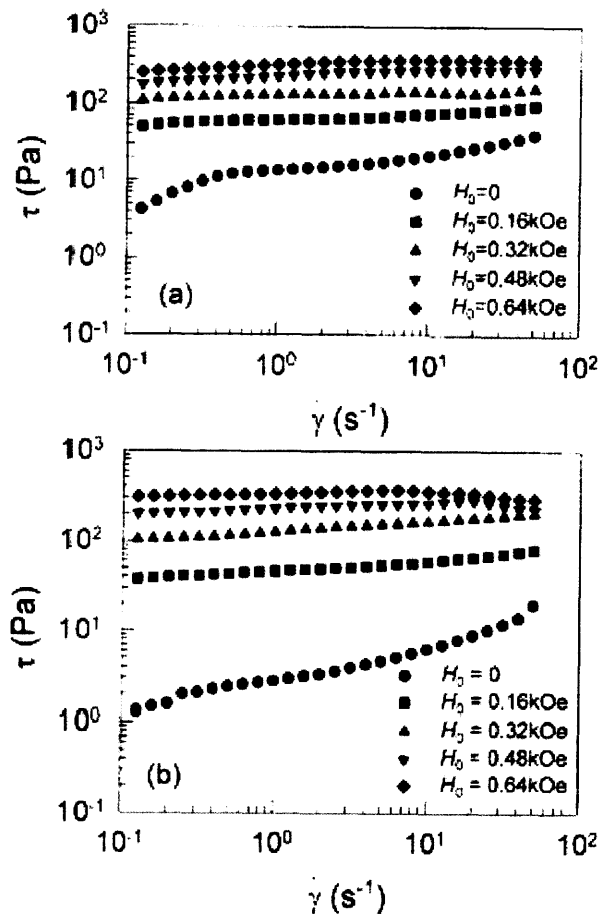


Figure 2.6 Steady shear flow data for,  $Fe_3O_4$  in silicone oil MR fluid, showing dependence of yield stress on the magnetic field strength a)  $\phi = 20\%$  b)  $\phi = 40\%$  (Chin *et al.* 2001).

The effect of particle volume fraction on the dynamic yield stress is also evident from figure 2.6 and is observed to increase almost linearly with volume fraction at a constant magnetic field (Chin *et al.* 2001). Experiments have also been carried out for various dispersing mediums, notably the use of a viscoplastic medium, like grease, to prevent sedimentation of the constituent particles (Rankin *et al.* 1999).

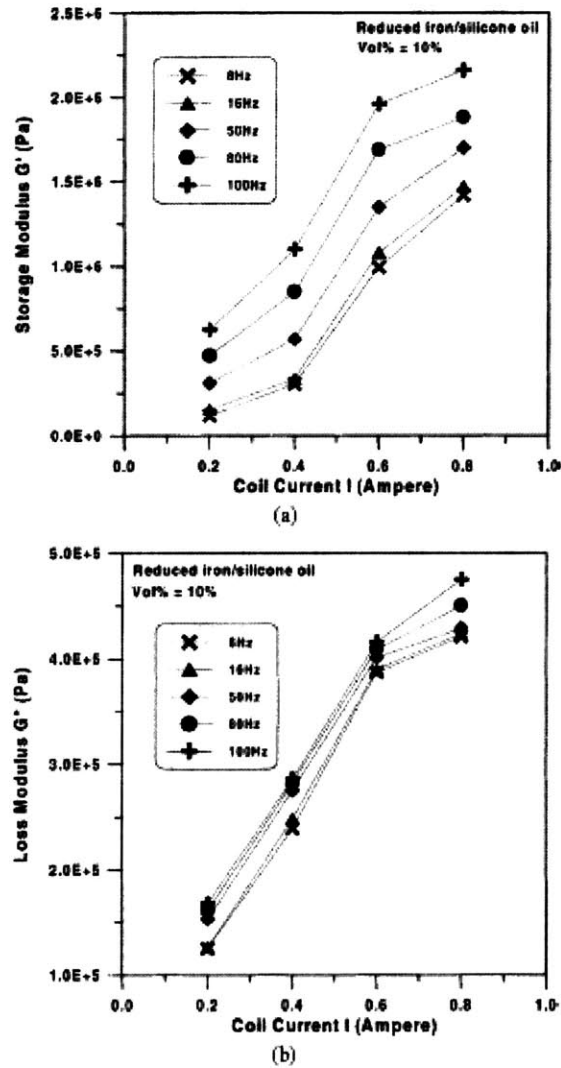


Figure 2.7 Dependence of the linear viscoelastic moduli ( $G'$ ,  $G''$ ) on the magnetic field strength (represented by current flowing through the electromagnet in amperes) and the frequency of the oscillatory flow for 10% suspensions of iron powders (Li *et al.* 1999).

Since ER and MR fluids exhibit a yield stress, they are considered viscoplastic materials and small-amplitude oscillatory shear experiments in which the upper plate or cone undergoes small-amplitude sinusoidal oscillations in its own plane with a frequency ( $\omega$ ) and displacement ( $\gamma \ll 1$ ) so that the instantaneous velocity is almost linear, are often used to obtain characteristic material functions. Representative measurements of linear viscoelastic properties,  $G'$  (storage modulus) and  $G''$  (loss modulus) obtained for MR fluids from such experiments are shown in figure 2.7. In the linear viscoelastic region, both  $G'$  and  $G''$  increase with magnetic field and volume fraction of particles (Li *et al.* 1999). A very limited number of investigations have also looked at a number of other unsteady shear-flow material functions obtained from creep, recovery or step-strain experiments (Li *et al.* 2002). We pursue similar studies that are described in chapter 4.

### 2.1.7 Applications of Field-Responsive Fluids

Field responsive materials whose properties can be continuously, rapidly and reversibly varied are used in a number of applications. In the last few years, MR fluids have enjoyed considerable commercial success and Lord Corporation has brought a number of products in the market<sup>3</sup>.

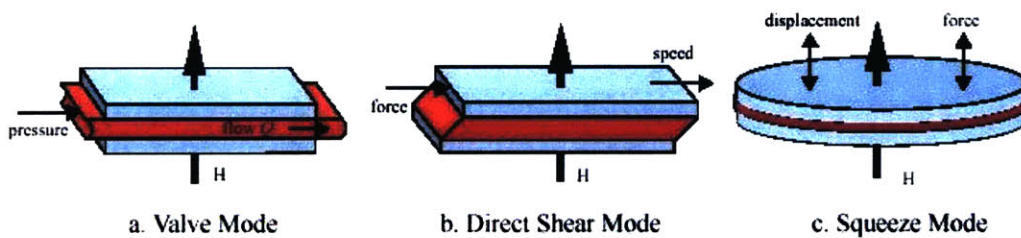


Figure 2.8 The 3 basic operation modes a) valve mode b) direct shear mode c) squeeze mode for field-responsive fluids (Carlson and Jolly, 2000).

<sup>3</sup> <http://www.rheonetic.com>

All the devices utilizing these fluids operate in one of three modes, as shown in figure 2.8, a) valve mode in which the flow rate decreases with magnetic field for the same pressure drop due to resistance to flow provided by chain formation b) shear mode in which the field-induced dipolar chains are sheared to obtain a magnetic field dependent force c) squeeze mode in which the displacement compresses the dipolar chains to obtain a variable damping force.

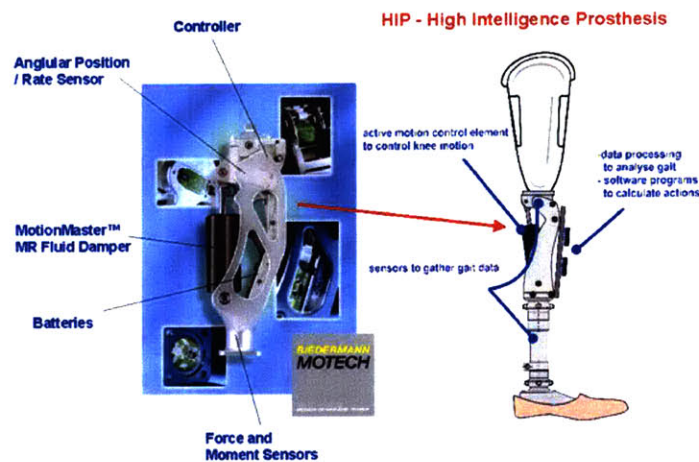
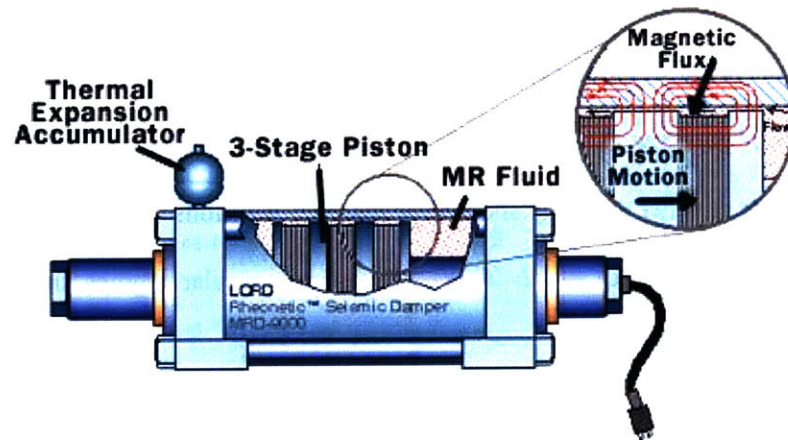


Figure 2.9 a) Lord Corporation's 20 ton seismic damper MRD-9000 utilizing a 3-stage piston and 6 litres of MR fluid (Dyke *et al.* 1998) b) A prosthetic knee utilizing a MR fluid based damper for active motion control <sup>4</sup>.

<sup>4</sup> <http://www.rheonetic.com>

Many applications utilize these variable flow rate or force characteristics in either damping or torque transfer scenarios and proposed applications include shock absorbers, clutches, brakes, actuators and artificial joints (Klingenberg 2001). A MR fluid damper or shock absorber utilizes the viscous dissipation of energy of vibration due to the forced flow of the fluid in one or more channels as shown in figure 2.9. The damping force can be regulated using a varying magnetic field and semi-active suspension systems have been developed using this controllable phenomenon as a basis (Yang *et al.* 2002, Li *et al.* 2000, Kelso 2001).

MR fluid damping devices have also been used in space applications, prosthetic knees, industrial engine mounts, exercise equipment and even washing machines (Chrzan and Carlson 2001). In washing machines, MR fluid, filled inside an absorbent matrix such as a sponge or foam has been used in shear mode as shown in figure 2.10. This decreases the moving parts and also the active fluid required in the device, which makes it an excellent cost-cutting solution. Furthermore, the absorbent matrix holds the fluid in place due to capillary forces and thus prevents the particles from settling.

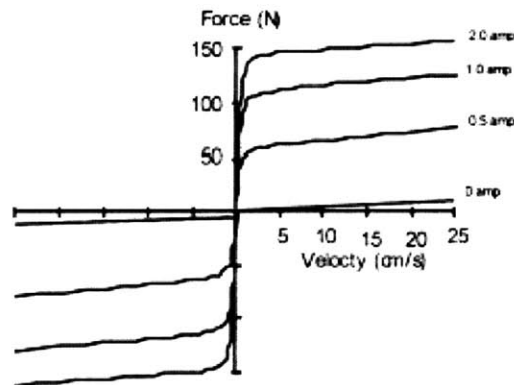


Figure 2.10 Force versus velocity curves with varying magnetic field for a semi-active MR foam damping system developed by LORD Corp. for washing machine applications (Carlson and Jolly 2000).

Clutches and brakes and a number of other applications utilize the nonlinear and switchable torque transfer capabilities of these materials. The torque is transferred between two members by utilizing the variable viscosity of these fluids and can be varied from 0% to almost 100% using a varying magnetic field. This provides for a smoother transmission, improved heat-transfer capabilities and reduced power-train transients with no intermediate moving parts. Pneumatic actuators can be improved or completely replaced using MR fluid technology, by controlling the flow of fluid with a large magnetic field, making the use of valves unnecessary. FRFs have also been used in the polishing industry wherein the mechanical force exerted on the workpiece is actively controlled using a magnetic field (Klingenberg 2000).

Magnetorheological elastomers, comprising of natural or synthetic rubber filled with micron-sized iron particles, cured in the presence of a magnetic field, have also been formulated and studied. Davis (1999) predicts the change in the modulus of typical elastomers to be approximately 50% in the presence of high magnetic fields. This variable stiffness property of elastomers, controlled by a magnetic field, can be used in various applications like automotive bushings, variable impedance surfaces, tuned vibration absorbers and engine mounts (Ginder 1996).

### **2.1.8 Comparison of MR and ER fluids**

The ultimate strength of MR fluids depends on the saturation magnetization of the dispersed particles and hence pure iron (saturation magnetization 2.15 T), or iron/cobalt alloy (saturation magnetization 2.4 T) particles are chosen. The maximum energy density in ER fluids, on the other hand, is determined by the dielectric breakdown (i.e. critical electric field when conduction paths within the fluid lead to destructive breakdown) for the particles and is about 2 orders of magnitude less than the MR fluids. The yield strength of ER fluids is hence around 2–5

kPa as compared to nearly 100 kPa obtained for MR fluids<sup>5</sup>. The active fluid needed for MR devices is thus much less as compared to ER devices resulting in much smaller devices.

Also, the constituent particles are stabilized in the medium by the use of surfactants and other additives. ER fluids are sensitive to these additives and other impurities, while these do not affect the polarization mechanism in MR fluids leading to enhanced stability, lubricity etc. Further, temperature variations do not have a strong effect on magnetic polarization so that MR fluids can operate over a much larger temperature range (-40 °C to 150 °C) as compared to ER fluids. Hence, though MR fluids have appeared in number of commercial applications, ER fluid based applications have remained elusive.

However, since iron particles comprise most of the MR fluids, the fluids tend to be much heavier as compared to ER fluids and particle settling becomes an important concern.

### **2.1.9 Challenges for Field – Responsive Fluids**

ER fluids have been plagued by a number of problems and their inferior rheological properties and poor long-time stability as compared to MR fluids have prevented their use in commercial products. MR fluids on the other hand have a huge cost limitation and many more applications would quickly become commercial if the material cost could be reduced (Klingenberg 2001).

The saturation magnetization of MR particles, which is a material property attained when all the magnetic moments in the sample are aligned, is the limiting factor for determining the strength of MR fluids and a higher strength would clearly make many new applications viable. Since iron particles usually comprise an MR fluid, particle settling is an important concern though a viscoplastic medium or an absorbent matrix has been used to overcome these problems to a certain extent. In-use-thickening (IUT) or increase in the off-state force with time, as particles undergo wear and tear, is a significant challenge for the use of these fluids (Carlson

---

<sup>5</sup> <http://www.rheonetic.com>



2001). Some recent patents (U.S. Patent No. 0045540) have claimed the development of durable MR fluids, which reduce the agglomeration of particles with time, by use of mechanically hard magnetic particles and some anti-wear additives. However, much research effort is needed in understanding field-responsive fluid rheology before these limitations and challenges can be overcome and commercialization of new applications can be facilitated.

## **2.2 Shear–Thickening Fluids**

### **2.2.1 Description and Composition**

Shear–thickening is defined as the increase in viscosity, sometimes discontinuous, with increase in shear rate. It is related, but not the same as ‘dilatancy’, which is the increase of volume (hence viscosity) with deformation, or ‘rheopexy’, which means increase in viscosity with time at a fixed shear-rate. A number of colloidal dispersions, almost all concentrated suspensions of nonaggregating solid particles show shear thickening under certain conditions. Besides suspensions, concentrated dispersions of polymer particles, wormlike micelles and associative polymers also show the shear-thickening phenomenon. The general behavior of a shear-thickening fluid, wherein viscosity normally decreasing with shear-rate starts increasing at a critical shear rate  $\dot{\gamma}_c$  is shown in figure 2.11. The viscosity after reaching a maximum (at a shear rate  $\dot{\gamma}_m$ ) usually decreases again or levels out to a plateau region.

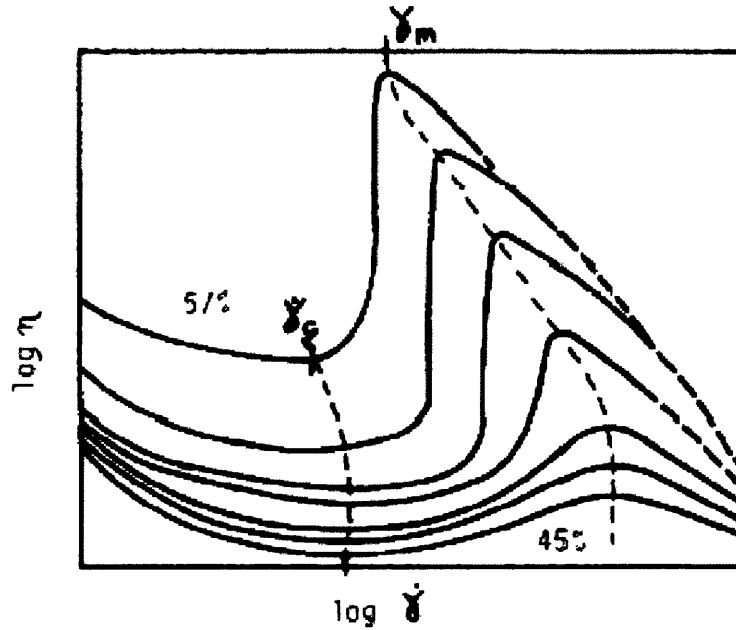


Figure 2.11 Schematic representation of viscosity versus shear rate for shear-thickening systems, with approximate phase volume as parameter (Barnes 1989).

## 2.2.2 Parameters Controlling Shear – Thickening

A number of parameters are crucial to shear-thickening especially the onset point (i.e. the critical shear rate  $\dot{\gamma}_c$ ) and these have been well summarized in the review article by Barnes (1989). The critical shear-rate has been found to vary with changes in volume fraction, though the dependence becomes small near around 50% as shown in figure 2.11. Below 50% volume fraction of the particles, the critical shear rate increases dramatically, while it reaches a near zero shear-rate value as the volume fraction approaches the maximum.

The critical shear rate also goes up higher with a reduction in particle size, as shown in figure 2.12 and a quadratic dependence has also been proposed when the phase volume is near 50%. The severity of shear – thickening is highly dependent on the monodispersity of the particles. A broad particle size distribution decreases the severity of the jump in viscosity, besides

increasing the critical shear-rate, and is a common industrial practice used to reduce shear thickening or ‘jamming’ of pipelines (Boersma *et al.* 1990).

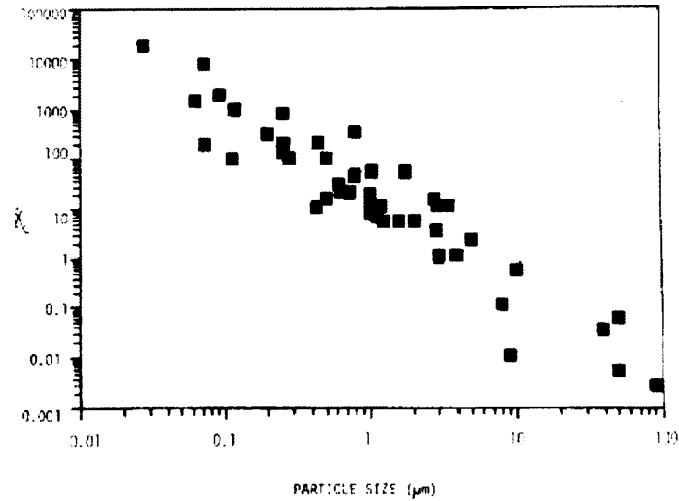


Figure 2.12 Critical shear-rate as a function of the average particle size (Barnes 1989).

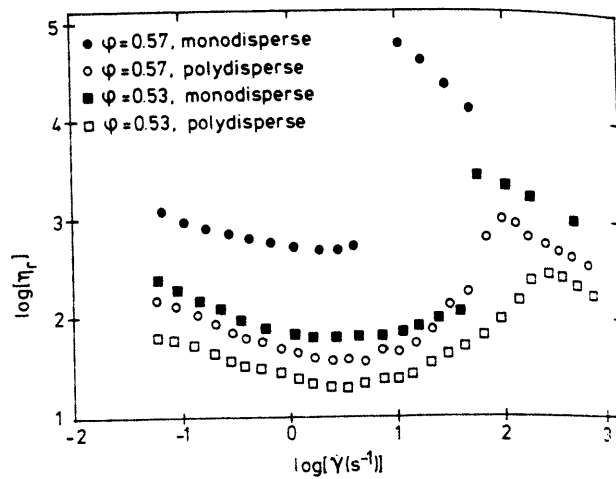


Figure 2.13 Effect of particle size distribution on the critical shear rate and the severity of the jump in shear-thickening (Hoffman 1972, Boersma *et al.* 1990).

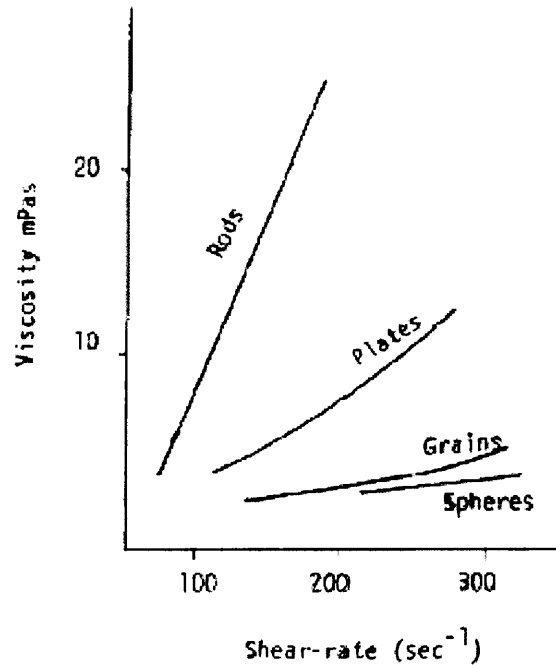


Figure 2.14 Particle shape effects on shear thickening for 20% suspensions of inorganic mineral crystals (Barnes, 1989).

Particle shape effects are complicated by various other factors and hence are not well documented, though, as figure 2.14 shows clearly, more anisotropic particles tend to increase the severity of shear thickening even at comparatively lower particle volume fractions (Barnes, 1989). Also, only suspensions stabilized with electrostatic or steric repulsions between the particles show pronounced shear-thickening and in this sense interactions between particles becomes an important consideration for shear-thickening. Deflocculated suspensions are found to be shear thickening while flocculation causes the suspensions to become shear thinning. A number of other factors including continuous phase viscosity, time and type of deformation applied also affect shear-thickening and have been well documented (Barnes 1989).

### 2.2.3 Mechanisms responsible for Shear – Thickening

Shear thickening has been a well-observed phenomenon for a century now but little progress has been made in understanding the microstructural origins behind the phenomenon or developing models for predicting the onset of shear thickening. There are two schools of thought; one believing that an order to disorder transition (ODT) is responsible while the other believes that a ‘hydrocluster’ mechanism is responsible for shear thickening. Both, however, suggest changes in suspension microstructure are driven by the interplay of hydrodynamic, Brownian and interparticle forces as the cause behind shear thickening. Egmond (1998) has suggested that formation of hydrodynamic clusters is relevant in hard sphere suspensions while a shear – induced order disorder transition (ODT) precedes the cluster formation in electrostatically stabilized suspensions.

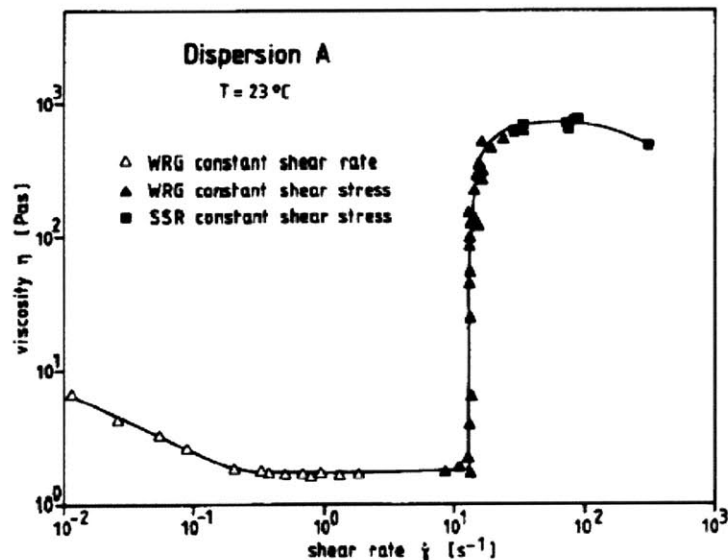


Figure 2.15 Viscosity versus shear rate curve showing the discontinuous jump in viscosity at a critical shear rate when the order in particles is disrupted (Laun *et al.* 1991).

The general model based on ODT, proposed by Hoffman (1972, 1974, 1982), supposes that particles are ordered into sliding layers parallel to surfaces of constant shear at low shear rates and at a critical shear rate pairs of particles rotate out of the shear plane forming eddies and disrupting the order. The extra energy required in this disorder transition manifests itself as a jump in the apparent viscosity leading to the phenomena of shear thickening, as depicted in figure 2.15.

Hoffman (1972) provides evidence of this ordering from diffraction patterns and Boersma *et al.* (1990) have developed a model based on interplay of shear and interparticle forces to support this hypothesis. A critical shear rate is predicted from the balance of these forces, as described below and compares well with the experimental results.

$$\dot{\gamma}_c \sim \left( \frac{2\pi\epsilon_0\epsilon_r\psi_0^2}{6\pi\eta_0 a^2} \right) \quad (1.8)$$

where  $\psi_0$  is the surface potential,  $\eta_0$  is the medium viscosity and  $a$  is the particle radius.

The ODT theory however predicts the presence of an ordered phase as a necessary condition for shear thickening and Laun *et al.* (1994) found suspensions exhibiting shear thickening in absence of ordered structures. Stokesian dynamics simulations (Brady and Bossis, 1988) and later on SANS and rheological experiments by Bender and Wagner (1996) suggested the formation of transient ‘hydrodynamic’ clusters i.e. stress bearing clusters formed by shear induced self-organization of particles. The hydrocluster mechanism predicts that shear thickening occurs when hydrodynamic shear forces overcome Brownian repulsive interactions (Maranzano and Wagner 2003) and the onset of shear thickening is determined by a critical stress ( $\sigma_{cr}$ ) obtained by the balance of these forces

$$\left( \frac{\sigma_{cr} a^3}{kT} \right) = - \frac{h}{3\pi} \frac{\eta}{\mu_0} \left( \frac{d \ln g(r)}{dx} \right) \quad (1.9)$$

where  $a$  is the particle radius,  $h$  is the separation distance between the particles,  $\mu_0$  is the solvent viscosity and  $g(r)$  represents the equilibrium radial distribution function.

The scaling laws based on this mechanism predict the dependence on various parameters like phase volume and particle size in well accordance with experimental results as shown in figure 2.16.

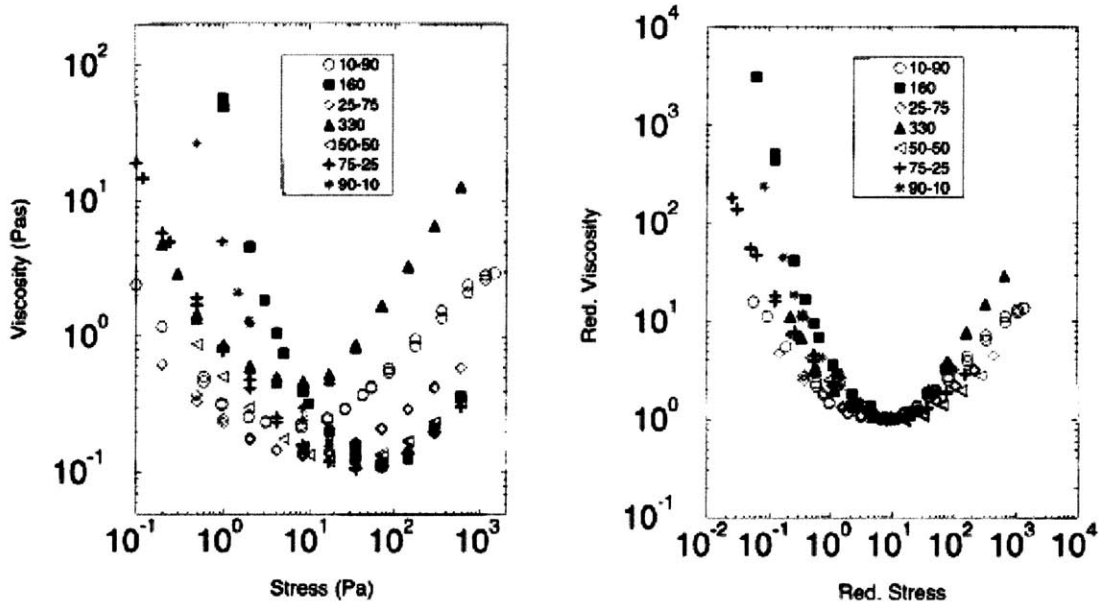


Figure 2.16 (a) Viscosity versus stress plotted for monodisperse hard-sphere shear

thickening suspensions. (b) Reduced viscosity  $\left( \frac{\eta}{\mu_0} \right)$  (suspension viscosity reduced by the

viscosity minima) versus reduced stress  $\left( \frac{\sigma_{crit} a^3}{kT} \right)$  for depicting the critical stress as

defined by the hydrocluster mechanism (Bender and Wagner 1996).

## 2.2.4 Rheology and Viscoelasticity of Shear – Thickening Fluids

Steady shear rheology of shear thickening fluids, as shown in figures 2.11, 2.15 and 2.16 earlier, shows a large increase in viscosity with increasing shear rate and the onset is defined by a critical shear rate or a shear stress.

The increase in viscosity, especially for monodisperse polymer dispersions, is almost discontinuous and is associated with a strong increase in normal forces (Laun, 1994). Transient shear rheology shows strong time effects accompanying shear thickening and a number of authors have reported the presence of flow instabilities in these dispersions (Boersma *et al.*, 1991, Head *et al.*, 2002). These effects are usually complicated by the presence of ‘dilatancy’ besides wall slip and cluster formation. Chow and Zukoski (1995) have extracted the effect of wall slip in shear thickening suspensions through careful experiments at varying gap sizes as shown in figure 2.17.

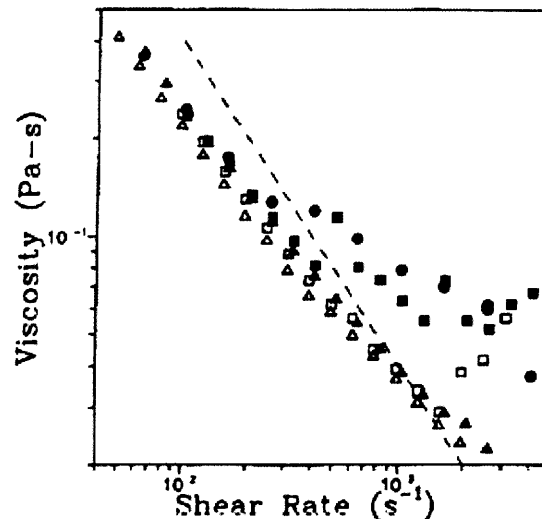


Figure 2.17 Viscosity as a function of shear rate with increasing shear rate in the tapered plug geometry with gaps of 20, 15, 10, 7.5, 4.8 microns (Chow and Zukoski, 1995).



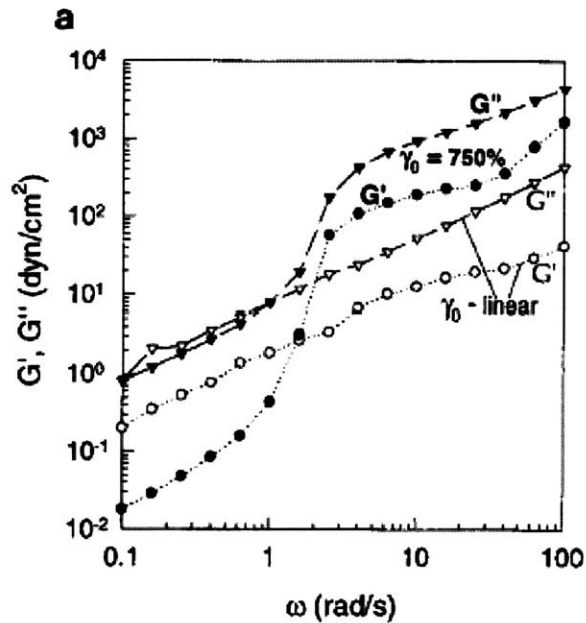
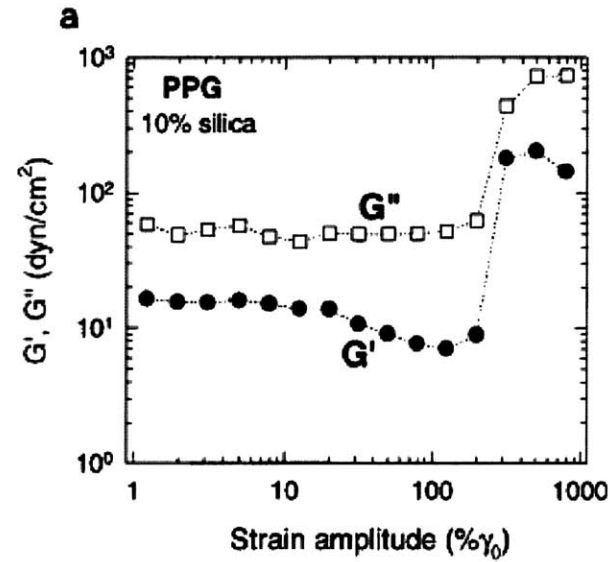


Figure 2.18 Storage  $G'$  and loss  $G''$  moduli as functions of strain amplitude and frequency for 10% fumed silica suspension in PPG (Raghavan and Khan, 1997).

Linear viscoelastic properties of shear thickening fluids reflect the behavior observed in steady shear data.  $G'$  (elastic modulus) lags  $G''$  (viscous modulus) in magnitude indicating that the suspensions are largely viscous in nature. Also, deflocculated suspensions show strain

thickening at high deformations or high frequencies when both  $G'$  and  $G''$  increase almost abruptly (Boersma *et al.*, 1992) as shown in figure 2.18.

The dynamic shear rate in these oscillatory flows marking the transition to strain thickening matches well with the critical shear rate denoting the onset of shear thickening in steady shear flow, as given by the modified Cox-Merz rule (Raghavan and Khan, 1997; Lee and Wagner, 2003).

$$\eta^*(\gamma_0\omega) = \eta(\dot{\gamma})_{\dot{\gamma}=\gamma_0\omega} \quad (1.10)$$

where  $\gamma_0$  is the strain amplitude,  $\omega$  is the frequency,  $\eta^*$  is the complex viscosity and  $\eta$  is the steady shear viscosity.

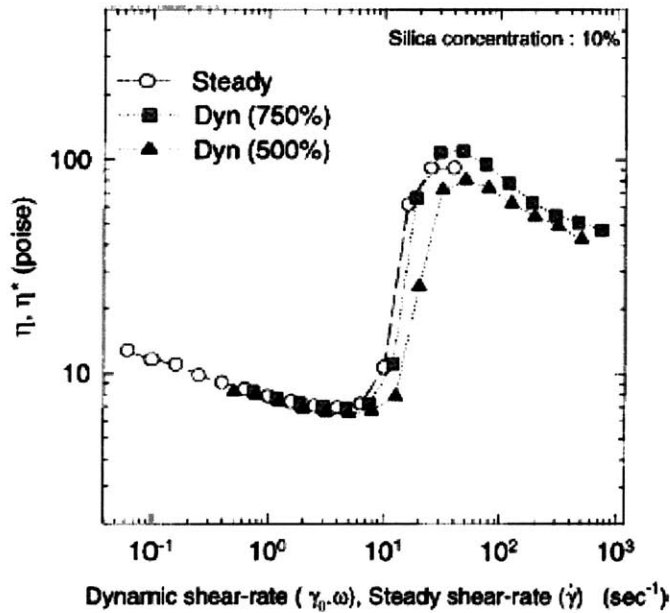


Figure 2.19 Comparison of steady and oscillatory shear data for 10% fumed silica suspensions in PPG in accordance with the modified Cox-Merz rule (Raghavan and Khan 1997).

## 2.2.5 Applications of Shear – Thickening Fluids

Shear thickening is known to cause many problems in industrial processes, especially ‘jamming’ of pipelines at higher flow rates and most efforts are directed towards minimizing this phenomenon. However, Laun *et al.* (1991) has described mechanical elements such as speed controllers and non-linear dampers utilizing extremely shear thickening monodisperse polymer dispersions. A recent U.S. Patent (5545128) describes a bone fracture prevention garment, utilizing compartments filled with a shear thickening fluid, which shunts the energy of a fall or an impact. These fluid formulations have also been used in sports shoe cushioning materials, shock absorber fillings and renewed efforts are being made to make a stable, storable shear thickening fluid (Maranzano and Wagner 2003).

Shear thickening fluids are cheap and much easier to formulate but stability is an important issue since, particles tend to flocculate with use and time. Also, properties are dependent on the deformation history and much research effort is required to make these fluids viable for repeated use in commercial applications.

## CHAPTER 3

### Cellular Solids: Review

A cellular solid is an interconnected network of solid struts or plates that form the edges and faces of cells (Gibson and Ashby, 1997). ‘Honeycombs’ are two-dimensional cellular materials while three-dimensional materials are known as ‘foams’.

#### 3.1 Structure and Properties of Foams

##### 3.1.1 Introduction and Cell Structure

A ‘cellular solid’ or an assembly of cells can have two types of cell structure, open-cell or closed-cell. An open-celled foam has open faces and all the solid material is contained in the cell edges while closed cell foam has solid in cell faces isolating cells from each other (figure 3.1). The cells are polyhedra of different shapes and the cell shape, cell edge length and the edge thickness, characterize the cellular material and define its properties.

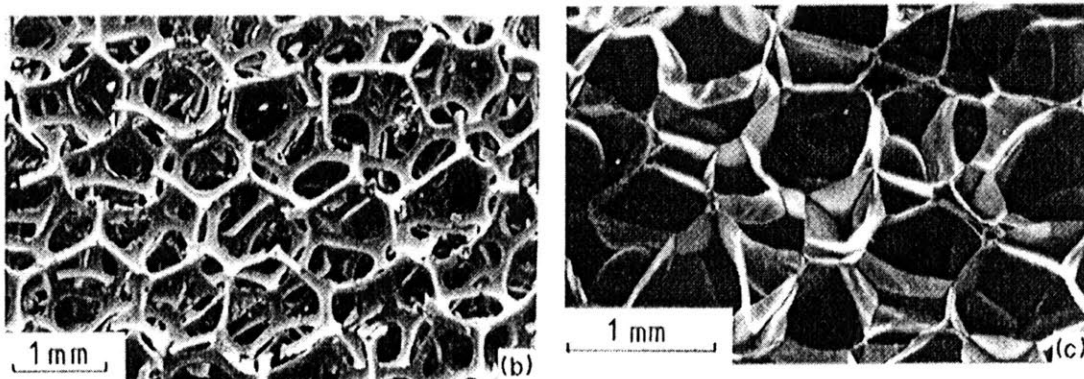


Figure 3.1 a) Open cell foam b) Closed cell foam (Gibson and Ashby, 1997)

A number of materials, polymers, metals, ceramics and composites, can be 'foamed'. The foaming process involves introducing a gas or a blowing agent throughout the fluid (constituent material) phase and stabilizing, cooling the resultant foam. These may also be prepared by leaching of a fugitive phase, such as a water-soluble salt, from a polymer; by sintering small particles dispersed in a heat stable matrix; by fusing initially discrete polymer particles or by forming a polymer matrix around hollow spheres. Reticulated foams are very low density, high porosity open cell foams formed from closed cell foams by breaking the cell walls by secondary processing. Microcellular foams, with cell sizes on the order of 10 microns, are made by heating a polymer supersaturated with inert gas to its glass transition temperature to cause cell nucleation and growth (Klempner and Frisch, 1991). Besides man-made materials, natural substances like wood, cancellous bone, sponge and cork are also cellular solids.

### 3.1.2 Properties of Cellular Solids

Cellular solids have physical, mechanical and thermal properties dependent on the intrinsic properties of the solid material and the geometrical parameters. The relative density ( $\rho^*/\rho_s$ ) is the most defining characteristic of a cellular solid, where  $\rho^*$  is the density of the cellular material and  $\rho_s$  is the density of the solid. The porosity of the cellular solid is determined simply from its relative density as  $1 - (\rho^*/\rho_s)$ . True cellular solids have porosity greater than 0.7 and can have porosities as high as 0.97 for ultra-low density foams. They have low stiffness, strength and can absorb large compressive strains, as compared to true solids, making them ideal for a wide variety of applications. The porosity or the relative density is determined by the cell dimensions, namely the cell edge length  $l$  and the cell wall thickness  $t$  as given by the following equation

$$\left(\frac{\rho^*}{\rho_s}\right) = C \left(\frac{t}{l}\right)^n \quad (3.1)$$

where the constant  $n$  is equal to 2 for open cell foams, 1 for closed cell foams and honeycombs and the constant  $C$  depends on the cell shape.

Unit cells in cellular solids are of different shapes and sizes but follow certain topological laws to fill the complete space. Figure 3.2 shows a packing of tetrakaidehedra cells usually observed in open cell polyurethane foams. The properties of the cellular solids depend on these cell structures and the geometric features have been well documented by Weaire (2000).

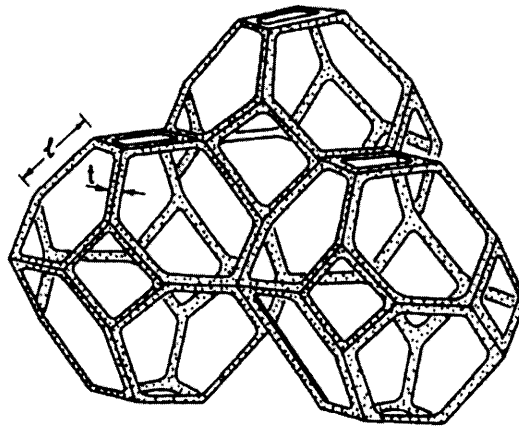


Figure 3.2 The packing of tetrakaidehedra cells in foam with the cell edge length and the wall thickness shown (Gibson and Ashby, 1997).

The characteristic properties of the solid material forming the cell such as density  $\rho_s$ , Young's modulus  $E_s$ , plastic yield strength  $\sigma_{ys}$ , thermal expansion coefficient  $\alpha_s$  and the specific heat  $C_{ps}$  also define properties of the cellular material such as the thermal conductivity, modulus and strength. Foams have exceptionally low thermal conductivity due to the low volume fraction of the solid phase and also a low specific heat per unit mass making them a popular

choice for thermal insulations. These materials also have a high electrical resistivity, which increases with decreasing relative density and a very low dielectric constant.

## 3.2 Mechanics of Foams

Foams are widely used as energy absorbing materials and hence understanding of their mechanical properties under various deformations becomes vital. Foams can be subject to either compression or tension and show varied stress-strain data under the two deformation mechanisms.

### 3.2.1 Foams in Compression

The typical stress-strain behavior for elastomeric foams under compression is shown in figure 3.3.

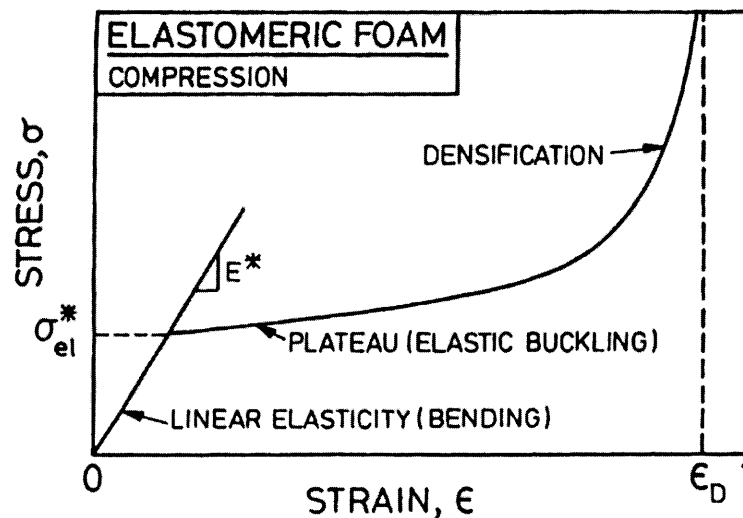


Figure 3.3 Schematic compressive stress – strain curve for elastomeric foam showing the three regions of linear elasticity, collapse and densification (Gibson and Ashby, 1997).

The figure shows three distinct regions: an elastic region where the curve is linear due to bending of cell walls and the slope is given by the Young's modulus of the foam ( $E^*$ ), a plateau

region where the cells start collapsing and the stress remains at a constant value ( $\sigma^*$ ) and a densification region when the opposing cell walls touch and the solid itself is compressed. The elastic buckling in case of elastomeric foams is responsible for a nearly constant stress plateau region while the stress rises up rapidly in the densification region due to solid incompressibility effects. The limiting strain when the opposing walls are crushed together so that the stress-strain curve rises steeply is known as the densification strain ( $\varepsilon_D$ ). Flexible foams have a low plateau stress ( $\sigma^*$ ) because of elastic buckling but regain their original form when the stress is removed. Rigid foams, on the other hand, usually have a high plateau stress because of a longer linear elastic region but the plateau region involves plastic yielding of cells and the original shape is permanently lost.

The mechanical properties are thus determined by the moduli in the linear elastic region and the plateau stress. These are obtained by a scaling approach assuming the cell edges to be beams under a compressive load undergoing bending or fracture and the equations obtained for open-cell foams are given by (Gibson and Ashby, 1997).

$$\frac{E^*}{E_S} \approx \left(\frac{\rho^*}{\rho_S}\right)^2 \quad \frac{G^*}{E_S} \approx \frac{3}{8} \left(\frac{\rho^*}{\rho_S}\right)^2 \quad \nu^* \approx \frac{1}{3} \quad (3.2)$$

$$\frac{\sigma^*}{E_S} \approx 0.03 \left(\frac{\rho^*}{\rho_S}\right)^2 \left(1 + \left(\frac{\rho^*}{\rho_S}\right)^{0.5}\right)^2$$

where  $E^*$  is the elastic modulus,  $G^*$  is the shear modulus and  $\nu^*$  is the Poisson's ratio of a open-cell foam. The prefactors, 0.03 and  $3/8$ , have been obtained by approximately fitting the experimental data. The plateau modulus  $\sigma^*$  is proportional to the relative density squared and the final correction factor only considers the extra complications of geometry arising when the density is not small.



In closed cell foams, the solid fraction  $\phi$  in the cell faces also determines its stiffness. Thus, besides cell edge bending, the contribution due to compression of the cell fluid and membrane stresses in the cell faces is also considered.

$$\frac{E^*}{E_s} \approx \phi^2 \left( \frac{\rho^*}{\rho_s} \right)^2 + (1-\phi) \frac{\rho^*}{\rho_s} + \frac{p_0 (1-2\nu^*)}{E_s \left( 1 - \frac{\rho^*}{\rho_s} \right)} \quad (3.3)$$

$$\frac{G^*}{E_s} \approx \frac{3}{8} \left\{ \phi^2 \left( \frac{\rho^*}{\rho_s} \right)^2 + (1-\phi) \frac{\rho^*}{\rho_s} \right\} \quad \nu^* \approx \frac{1}{3}$$

where  $p_0$  is the initial gas pressure, usually atmospheric pressure and  $\phi$  is the solid fraction in cell edges.

The densification region is reached when the cell material is itself compressed and occurs at a limiting strain ( $\varepsilon_D$ ) that is slightly higher than its porosity, since in reality, at this strain itself the cell walls jam together

$$\varepsilon_D = 1 - 1.4 \left( \frac{\rho^*}{\rho_s} \right) \quad (3.4)$$

### 3.2.2 Fluid-filled foams in compression

Many types of foam, natural and man-made, are filled partially or are completely saturated with fluids. The expulsion of cell fluids adds to the peak stress of the foam, as energy is required to force fluids with viscosity through channels and this effect is more pronounced at higher strain rates as shown in figure 3.4.

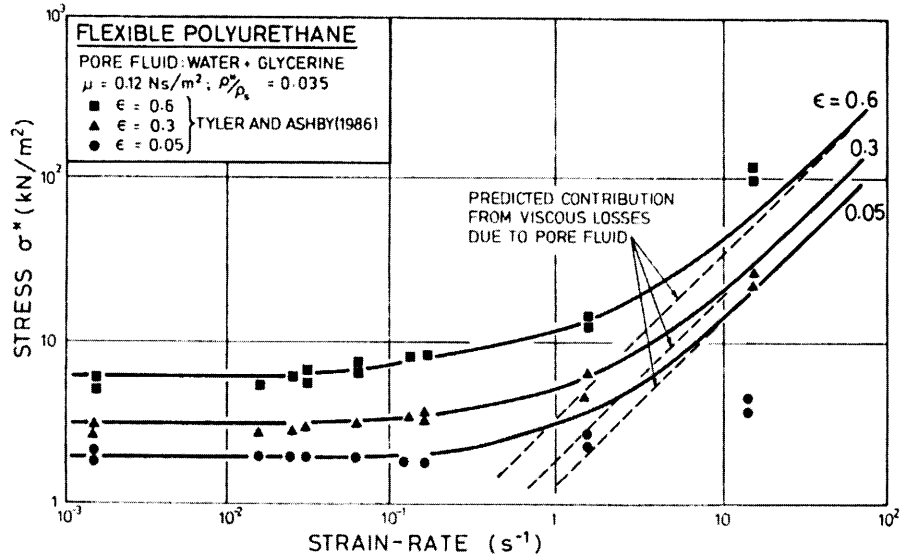


Figure 3.4 Plateau stress as a function of strain rate for a flexible polyurethane foam saturated with a water-glycerin mixture. The broken lines are theoretical predictions for Newtonian fluids (Gibson and Ashby, 1997).

Gibson and Ashby (1997) treat foam as a porous medium and apply Darcy's law and a scaling approach to obtain the contribution of pore fluid as

$$u = \frac{K dp}{\mu dx} \tag{3.5}$$

$$\sigma_f^* = \frac{C\mu\dot{\epsilon}}{1-\epsilon} \left(\frac{L}{l}\right)^2$$

where  $u$  is the fluid velocity,  $K$  is the absolute permeability,  $\mu$  is the viscosity of the fluid,  $p$  is the pressure,  $\sigma_f^*$  is the fluid contribution to plateau stress,  $\dot{\epsilon}$  is the strain rate and  $L$  is the characteristic length of the material.

Warner and Edwards (1988) and later Warner *et al.* (2000) extended this approach to closed cell cellular solids, wherein the incompressibility of the cell fluid results in stretching of walls, explaining the elasticity and failure of many foodstuffs like carrots. Micromechanical

models for filled foams have been developed to explain coupling of rheological and poroelastic effects using Biot – Frenkel theory (Lopatnikov, 1998, Lopatnikov and Cheng, 1998, Dunger *et al.*, 1999).

Non-Newtonian fluid effects, however, have not been considered in these micromechanical foam models. Pearson and Tardy (2002) have reviewed the flow of non-Newtonian fluids in porous media, modeling them as a bundle of capillaries of varying diameter and length and have developed equations for the pressure drop and flow rates.

### 3.2.3 Energy absorption in Foams

Foams are widely used in the packaging industry due to their superior energy absorption capabilities as compared to true solids. The plateau region during compression of foams, as shown in figure 3.5, is responsible for higher energy absorption even at low stress levels. The kinetic energy of impact is dissipated, absorbed by foams while keeping the peak stress on the object below the injury or failure limit.

The mechanisms responsible for this large energy absorption ( $W$ ) include the elastic, plastic or brittle deformations of the cell walls and the flow of fluid within cells or through channels. These contributions for open cell elastomeric foam can be written as functions of the mechanical properties of the foam and is found to be largely dependent on the relative density, plateau stress and the fluid viscosity.

$$\begin{aligned}
 W_{dry} &\approx \sigma^* \varepsilon_f = C_1 E_s \left( \frac{\rho^*}{\rho_s} \right)^2 \\
 W_{fluid} &= \int_0^{\varepsilon_f} \sigma_f^* d\varepsilon = C_2 \mu \dot{\varepsilon} \left( \frac{L}{l} \right)^2 \left( \frac{1}{1.4 \rho^* / \rho_s} \right)
 \end{aligned} \tag{3.6}$$

where  $\varepsilon_f$  is the strain at peak stress and  $W_{dry}$ ,  $W_{fluid}$  are the contributions to the amount of energy absorbed ( $W$ ) by the elastic buckling and the fluid flow respectively.

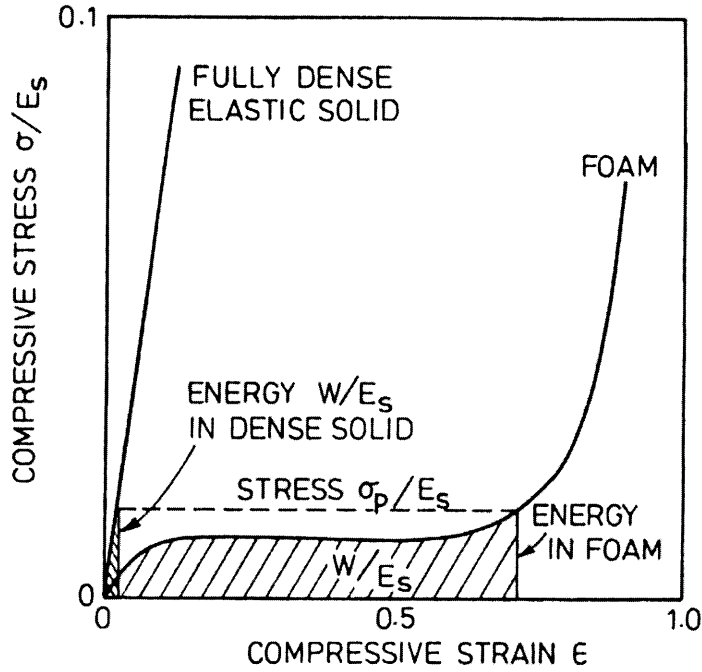


Figure 3.5 Comparison of energy absorbed, as the area under the stress – strain curve, between a true solid and a foam for the same levels of stress (Gibson and Ashby, 1997).

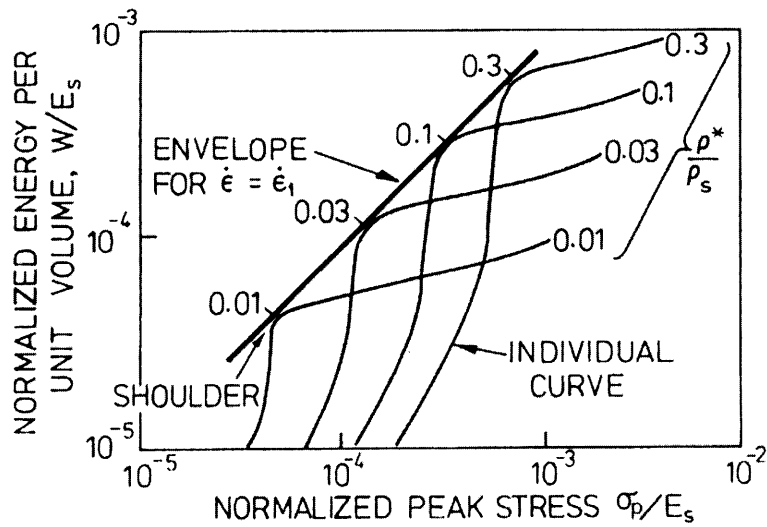


Figure 3.6 Energy absorbed, given as area under the stress – strain curve, normalized and plotted against the stress for varying relative densities to obtain an optimum energy envelope for a given strain rate (Maiti *et al.*, 1984).

Energy absorption characteristics of foams can be represented by various approaches such as plotting the Janssen factor, the cushion factor, the Rusch curve or an energy absorption diagram (Gibson and Ashby, 1997). The energy absorption diagram, as shown in figure 3.6, is a representation of a series of curves, obtained by varying parameters like strain rate or relative density, of normalized energy absorbed versus peak stress as an envelope of optimum energy (Maiti *et al.* 1984). These diagrams are especially useful in selecting the best foam for a given peak stress, since the envelope represents the optimum density and maximum energy absorption for a given peak stress and strain rate.

Energy is absorbed in closed cell foams also as cell walls bend, buckle and stretch but the contribution due to incompressibility of the cell fluid as it is compressed is relatively much higher and may even dominate for low density foams. The cell fluid contribution is much less for a plastic or rigid foam and energy absorption is largely due to the fracture and collapse of the cell walls in the plateau region.

### **3.2.4 Testing Apparatus for foams**

Foam properties, namely moduli and energy absorption capacity, are functions of strain rate and also temperature to some extent. At very high strain rates, dynamic (inertial) effects such as localization of deformation and micro-inertia drive up the peak stress and the compressive strength of foams (Gibson and Ashby, 1997). Laboratory compression testing equipments provide 'low' strain rates ( $10^{-8}$  to  $10^{-2}$   $s^{-1}$ ) while higher strain rate testing ( $10^{-2}$  to  $40$   $s^{-1}$ ) can be done using high-speed servo hydraulic and dynamic loading devices.

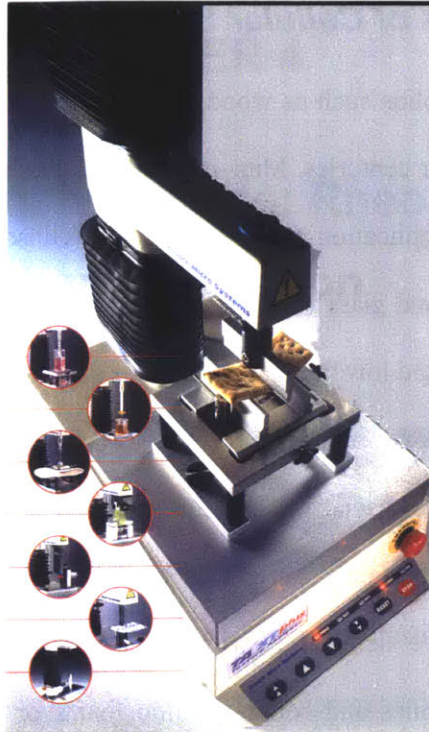


Figure 3.7 The Texture Analyzer, a low strain rate testing equipment for material and mechanical characterization of foams and semi–solid materials with interchangeable fixtures<sup>1</sup>.

The Texture Analyzer, a programmable low strain rate testing equipment has been widely used for solid foam and solid-fluid composite characterization. The instrument, manufactured by Stable Microsystems Inc., has a force range of up to 50 kg with a resolution of  $10^{-4}$  kg and hence provides accurate, repeatable information on mechanical properties of semi - solid substances. Figure 3.7 shows a picture of the instrument, with interchangeable fixtures that allow for a range of mechanical and rheological tests to be carried out. The velocity range of 0.01–40 mm/sec allows ‘low strain rate’ measurements with a high resolution in velocity (0.1%) and displacement ( $10^{-3}$  mm).

---

<sup>1</sup> <http://www.stablemicrosystems.com>

### **3.3 Applications of Cellular Solids**

Natural cellular solids such as wood, bone, honeycomb and many foodstuffs have been put to a variety of uses for centuries. Man-made foams like polymer or metallic foams are also widely used, and their application potential is huge (Gibson and Ashby, 1997). The largest application of polymeric and glass foams is in thermal insulation because of their exceptionally low thermal conductivity and low thermal mass.

Cellular solids have high impact energy absorption capacities, because of large compressive strains and low relative densities, and hence are used widely in the packaging industry. The strength of the foams can further be varied, to fulfill the application requirements, by controlling the relative density. Improvement of structural crashworthiness is a critical consideration for automobiles and hence metallic foams or honeycomb structures are used in ultralight impact absorbing components (Gotoh *et al.*, 1996). Also, sandwich panels made from cellular solids have excellent specific bending stiffness and strength and are used to provide a lightweight but strong structure in aircrafts, space vehicles and yachts (Goldsmith and Sackman, 1992).

Foams have an exceptionally low dielectric constant and this makes them critically important for microwave transmitting devices. Also, a high electrical resistivity makes them suitable for use in electrical components as insulators. Foams have high sound absorption coefficient at high frequencies (Gibson and Ashby, 1997) and are used for noise mitigation in sound absorbing panels.

The unique properties of cellular solids make them suitable for a number of applications and continued research in this field is expected to make many new applications viable. The large reversible changes in the rheological properties of field-responsive fluids, discussed earlier in chapter 2, have been used to modulate the energy absorption capacity and mechanical properties of elastomeric foams and discussed in detail in chapter 5.

## CHAPTER 4

# Field-Responsive Fluids: Rheology and Characterization

A number of commercially available and research-stage applications utilize the large, reversible changes in the rheological properties of field-responsive fluids. Understanding the rheological behavior of these fluids is vital to these applications and a number of previous studies have been reviewed in chapter 2. Fluid characterization and testing is again necessary for optimizing and designing the applications based on FRF impregnated cellular solid, the focus of this work.

### ***4.1 Magnetorheological Fluid Rheology***

#### **4.1.1 Experimental setup**

Two stress-controlled shear rheometers (TA instruments' AR 1000N and AR 2000) have been used to determine the steady-state rheological and linear viscoelastic properties of MR fluids. In general, a parallel plate (2cm diameter stainless steel plate with a gap height of 0.5 mm) arrangement and occasionally a cone-and-plate (2cm diameter 4° stainless steel cone) arrangement have been used for the experiments. Since the fluid properties are a strong function of the magnetic field, a custom-made fixture has been designed and built as a removable attachment to the rheometers for control and generation of a uniform magnetic field in the fluid sample space. The magnetic field generated is orthogonal to the direction in which the sample is sheared so that the MR fluid particle chains need to collapse before the sample starts flowing, thus allowing the measurement of magnetic field-dependent yield stress.



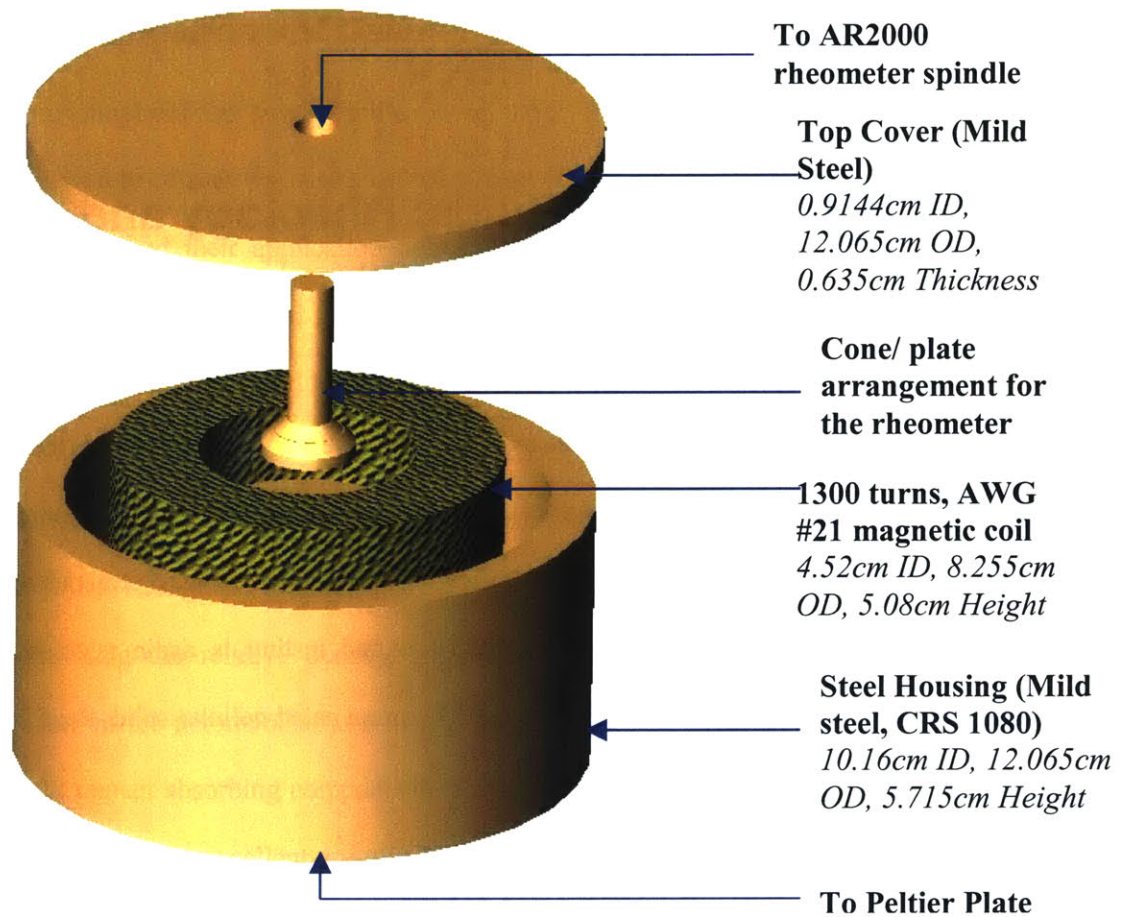


Figure 4.1 SOLIDWORKS model of the custom-built MR fluid fixture for the TA instruments' AR series rheometers.

An exploded view of the custom-built MR fluid rheometer fixture is shown in figure 4.1. The fixture is designed to allow a maximum gap of 1000 microns for the fluid sample between the top and the bottom plate. The bottom plate (4.52cm diameter) is formed from CRS (Cold Roll Steel)-1080 (McMaster Carr), which is a soft-magnetic (does not retain residual magnetism when the applied magnetic field is removed) but mechanically hard material. The outer and inner housing of the magnetic coil have been machined out of mild steel to concentrate the magnetic field lines through the sample. The fixture can also be made to snugly fit onto the Peltier plate of the rheometer, which allows for external temperature control. 1300 turns of wound AWG #21 (0.7329mm diameter) copper wire (RODON Products Inc.) form the base field-generating coil.

FEMM3.2 software has been used to determine the coil parameters such that a high magnetic field of up to 0.4 Tesla can be obtained in the fluid sample space<sup>1</sup>. Depending on the area of cross-section ( $A_{cs}$ ) available, the current density ( $J$ ) is determined as follows

$$I_{total} = JA_{cs} \quad (4.1)$$

where  $I_{total}$  is the total current that is required for the high magnetic field. The copper wire diameter and the number of turns ( $N$ ) is then chosen such that the current per turn ( $I_{turn}$ ) doesn't exceed its current carrying capacity as follows

$$I_{turn} = \frac{I_{total}}{N} \quad (4.2)$$

$$d_{wire} \approx \sqrt{\frac{1.15A_{cs}}{N}}$$

where  $d_{wire}$  is the copper wire diameter.

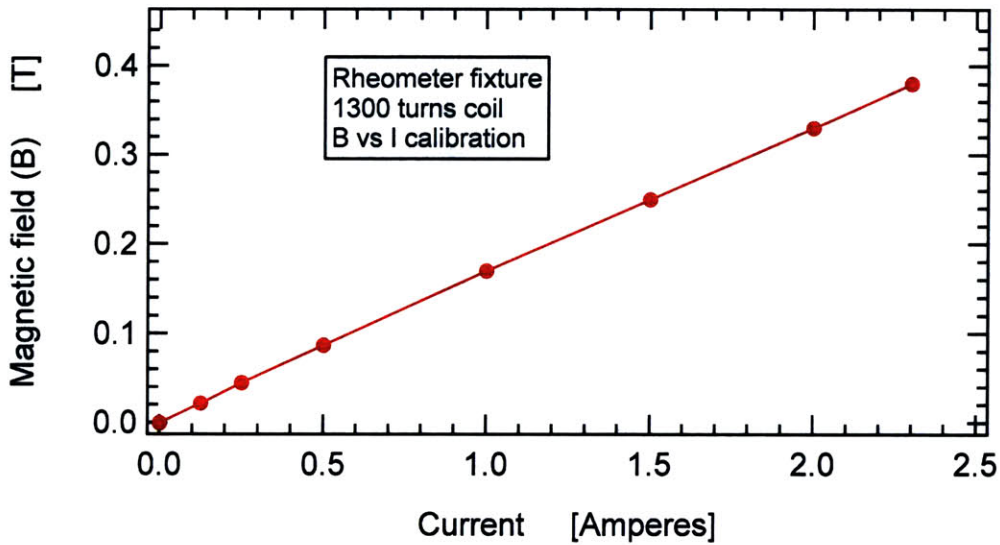


Figure 4.2 Magnetic field strength ( $B$ ) in Tesla, obtained in the fluid sample space using the custom-built MR fluid rheometer fixture, as a function of the DC current flowing through it.

<sup>1</sup> <http://mgc314.home.comcast.net/magnetics.htm>

This designed coil without the use of a cooling water system can then support a maximum current of 3.0A. A DC power supply (BK Precision Model 1670) provides a variable current from 0-2.5A and figure 4.2 shows the corresponding magnetic field obtained in the sample space.

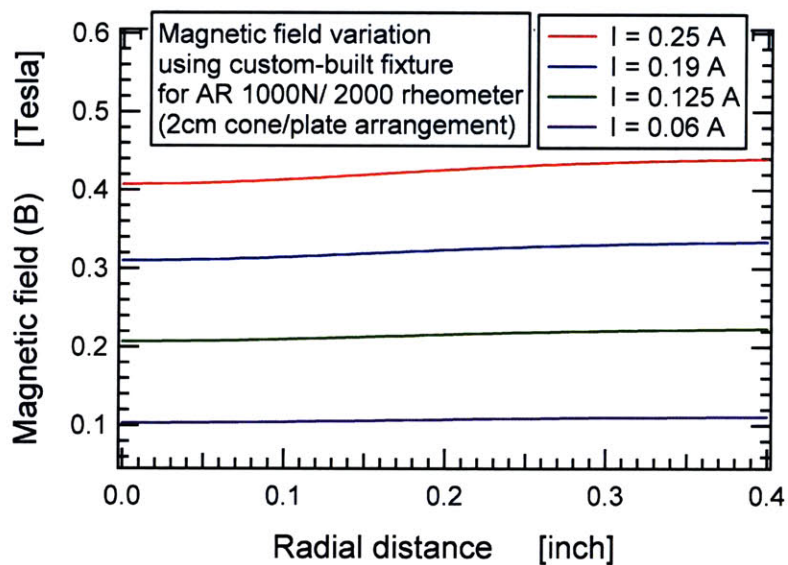
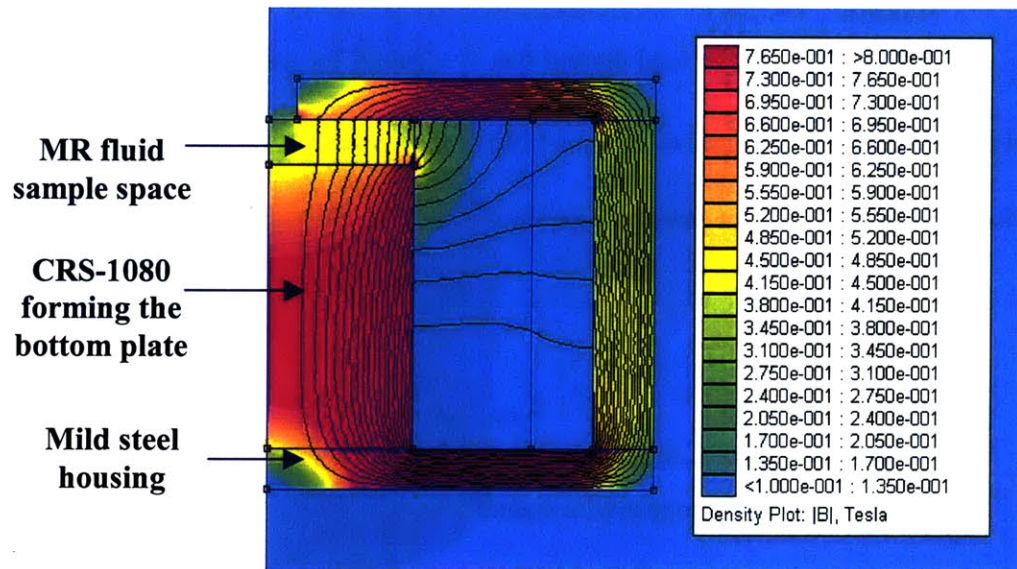


Figure 4.3 Magnetic field lines and gradients illustrated using a color-coded longitudinal section and fields against radial distance plot for the MR fluid AR 1000N/ 2000 rheometer fixture.

<b>Reference:</b>	<b>Rheometer Type of geometry</b>	<b>Fixture type and dimensions</b>	<b>Maximum magnetic field (B)</b>
Paar Physica Co.	UDS 200 Parallel plate geometry	Solenoidal coil Diameter = 20 mm N = 495 turns	0.34 T
Chin <i>et al.</i> (2001)	ARES (Rheometric Scientific Co.) Parallel plate geometry	Solenoidal Coil Diameter = 0.75 mm N = 2500 turns	~0.33 T
Cutillas <i>et al.</i> (1998)	Shear rheometer Parallel plate geometry	Helmholtz coil	0.025 T
Rankin <i>et al.</i> (1999)	Bohlin VOR rheometer Parallel plate geometry	Electromagnet wound with a coil N = 1000 turns	0.355 T
Deshmukh and McKinley (2003)	AR 2000/ 1000N rheometer (TA Instruments Co.) Parallel plate and cone and plate arrangement	Solenoidal Coil Diameter = 20 mm N = 1300 turns	0.4 T

Table 4.1 Comparison of fixtures, commercially available or custom-built, for determining the rheological properties of MR fluids with respect to various fixture parameters.

A gaussmeter (F.W. Bell Model 5060) with a transverse probe has been used to calibrate the magnetic field versus the input current. FEM analysis has been used to validate gaussmeter based experimental measurements and also to test the uniformity of the magnetic field. The magnetic field strength obtained from FEM analysis shows a maximum variation of 8% over the fluid sample space. Helmholtz coils could have been used to get a more uniform magnetic field but the field strengths obtained are typically very small and not suitable for complete characterization of fluid properties. Figure 4.3 depicts the magnetic field lines and flux gradient

for the rheometer fixture generated using FEMM 3.2 software. The axisymmetric planar view is color-coded, for example, the shades of yellow in the fluid sample space observed in the figure depict the magnetic field variation there. A comparison of the our in-house built MR fluid fixture for determining rheological properties with other commercial or custom-built fixtures from literature is presented in Table 4.1.

## 4.1.2 Steady shear rheology

Magnetorheological fluids, commercial and laboratory synthesized, have been characterized on the above described custom rheometer setup and compared with results from earlier studies (Genc and Phule 2002).

### 4.1.2.1 Commercial MR fluids

MRF-336AG, a silicone oil based magnetorheological fluid supplied by LORD Corp. and commonly used in the industry has been characterized under steady shear. It is composed of 36% v/v carbonyl iron particles ( $\sim 1 \mu\text{m}$ ) in a silicone oil carrier fluid and a number of proprietary additives. The rheological properties of the fluid under steady shear flow for different magnetic field strengths are shown in figure 4.4. The fluid has a weak yield stress ( $\sim 150 \text{ Pa}$ ) even in the absence of a magnetic field indicating the presence of a thixotropic additive. As the magnetic field is increased, the shear stress at which the fluid starts flowing also increases as can be observed from figure 4.4. The yield stress results are reproducible to within  $\pm 5\%$  and two different runs at each magnetic field are shown in the figure.

The experiments have been performed using a 2 cm diameter roughened plate arrangement. The top and bottom plates of the rheometer have been roughened by coating them with a very thin layer of carbonyl iron particles with a low viscosity glue (Permabond 910 cyanoacrylate) such that the roughness was of the order of the particle size. Roughening of plates was necessary to prevent slippage of MR fluid at higher shear rates. However, at higher shear

rates there is still migration of the sample out of the plates, which is commonly observed in samples with a yield stress (Citerne *et al.* 2001). A steady state viscosity after the yield point is thus not always observed in the samples and erroneous results are obtained at higher shear rates.

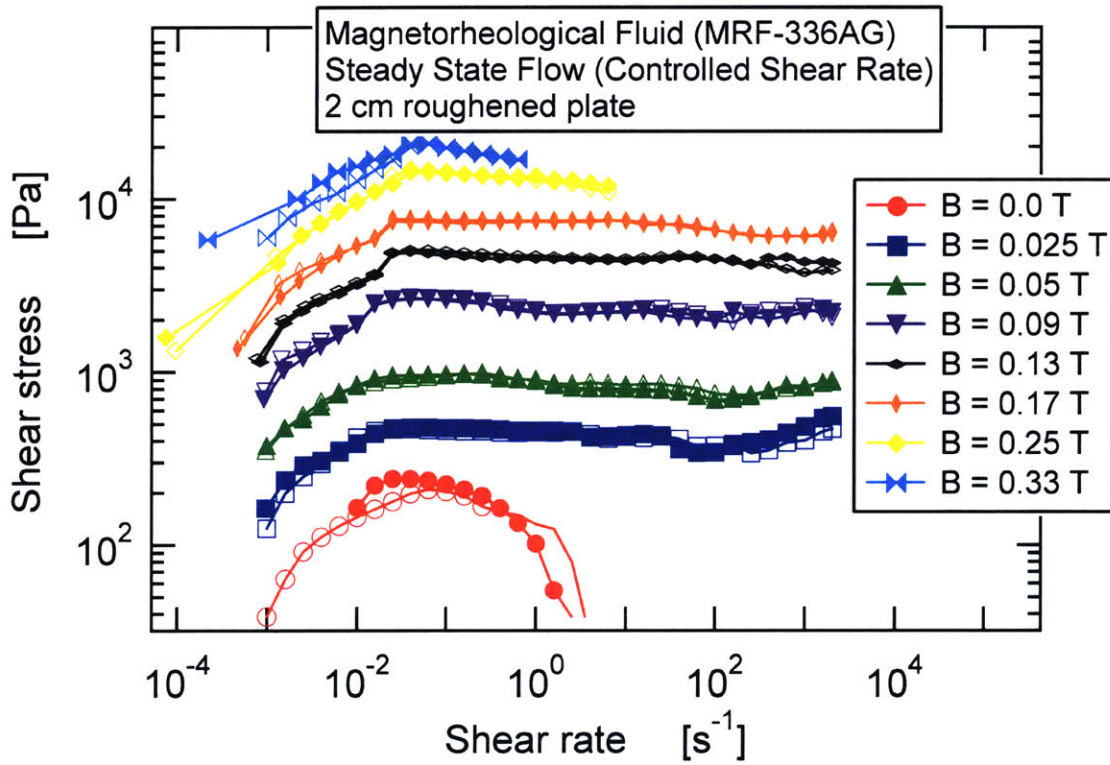


Figure 4.4 Steady shear rheology of MRF-336AG fluid using a 2cm roughened plate at a gap height of 0.5 mm for different magnetic field strengths.

A research-stage fluid formulated in Ossur with proprietary formulation technique has also been tested under steady shear. It is to be commercially used in prosthetic knees and is stable under much more stringent temperature and pressure conditions than LORD's MR fluid. Figure 4.5 shows its rheological properties plotted as viscosity against shear stress in steady shearing flow when the shear rate is controlled by the rheometer. The characteristics are similar to those exhibited by LORD's fluid with a sharp drop in viscosity at the yield point and loss of material at

higher shear rates is also observed. A discussion on yield stress calculation and comparison of these fluids with a in-house synthesized fluid is included in the next section.

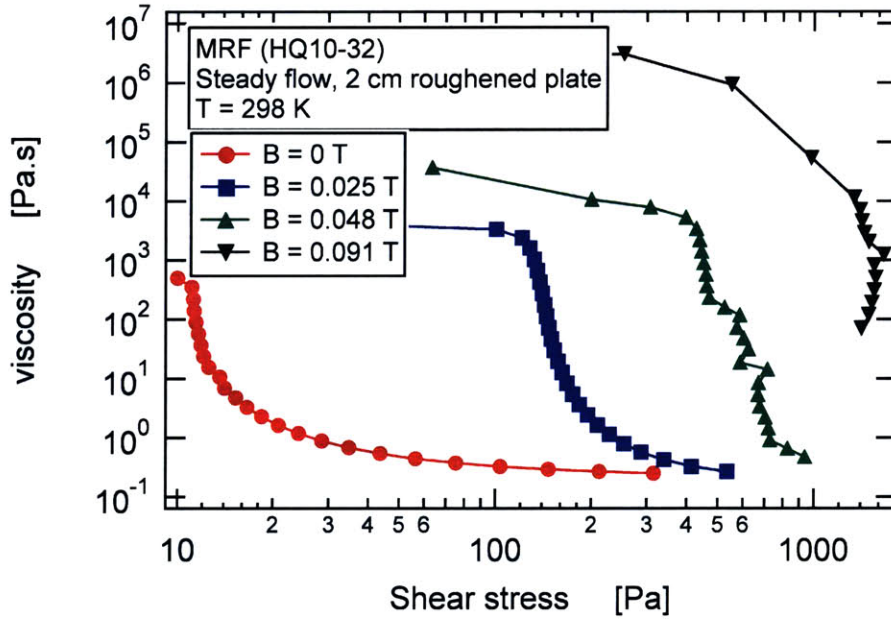


Figure 4.5 Rheological properties of the Ossur MR fluid measured in steady shear flow plotted as viscosity against shear stress for various magnetic field strengths.

#### 4.1.2.2 Laboratory synthesis of MR fluid

A severe limitation of commercially available MR fluids for industrial applications is their high cost (\$600/ litre). Also, these fluids are found to be plagued by stability issues as the particles settled over a period of time leaving a clear supernatant liquid. Hence, a highly stable magnetorheological fluid has been synthesized using in-house technology at a fraction of this cost and the rheological properties of the fluid compared with the commercial MR fluids.

Carbonyl iron particles (saturation magnetization  $\sim 2.03\text{T}$ ),  $1.1\ \mu\text{m}$  in size (BASF Corp.) at a volume fraction of 36% comprise the magnetizable matter in the synthesized MR fluid. Carbonyl iron powder (CIP) is obtained by thermal decomposition of iron pentacarbonyl

(Fe(CO)<sub>5</sub>) when spherical particles form on a nucleus thereby forming a shell structure<sup>2</sup>. The decomposition conditions decide the properties of the particles including the particle size distribution. Polydimethyl siloxane, trimethylsiloxy terminated (PDMS) with a viscosity of 0.1 Pa.s (Gelest Inc., DMS-T21) formed the carrier base of the MR fluid. Silicone oil has been used because of its low volatility, low viscosity dependence on temperature and inert nature towards other solid and liquid constituents. A surfactant, silanol terminated polydimethylsiloxane (Gelest Inc., DMS-S21), stabilizes the particles against agglomeration. This surfactant has a *-OH* terminal group which provides an affinity towards the carbonyl iron particles, while the PDMS part has an affinity towards the carrier fluid. A PDMS surfactant with an amine terminal group (Gelest Inc., AMS-132) has also been found to stabilize the particles in the fluid. A viscoplastic base, Dow Corning high vacuum grease, which blends well with the carrier fluid has also been utilized to provide a low off-state yield stress to the MR fluid and prevents the particles from settling under gravitational forces. Force balance gives the yield stress required in order to prevent the particles from settling

$$\sigma_y^{crit} (\pi r^2) \approx (\rho_p - \rho) \left( \frac{4}{3} \pi r^3 \right) g \quad (4.3)$$

where  $\sigma_y^{crit}$  is the critical yield stress to prevent settling,  $r$  is the radius of particle and  $\rho_p$  is the density of the particles. The critical yield stress works out to be nearly 0.5Pa for carbonyl iron particles with 1.1  $\mu m$  diameter ( $\rho_p$  of 7800 kg/m<sup>3</sup>).

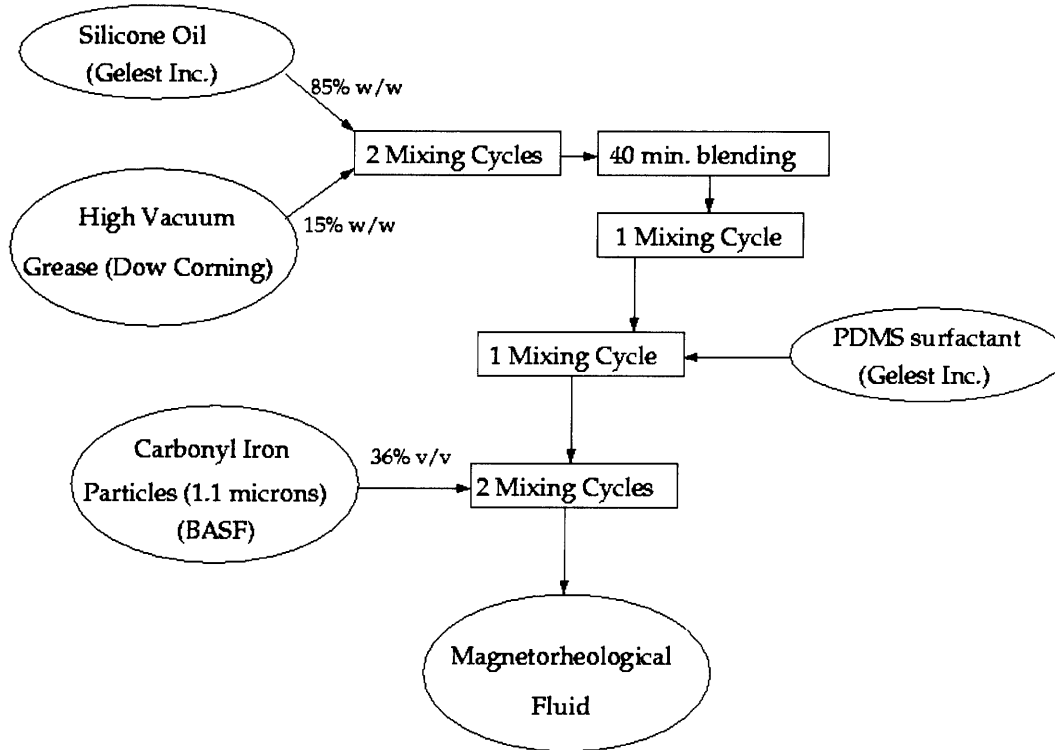
A step-by-step flowchart of the synthesis process is shown in figure 4.6. A conditioning mixer (Thinky Corp., AR-100) has been used for both mixing and degassing purposes. The mixing cycle of three minutes includes a one-minute combined rotation (160 rpm) and revolution (400 rpm) followed by a two-minute defoaming phase at a revolution speed of 2200 rpm. The

---

<sup>2</sup> <http://www.basf.com>



blend of 15wt% grease in silicone oil has a low field-off yield stress of approximately 1 Pa, which is sufficient to prevent the particles from settling.



1 Mixing Cycle is 3 min. Mixing + Degassing in Conditioning mixer

Figure 4.6 Magnetorheological fluid synthesis flowchart showing all the components and mixing steps.

The MR fluid thus formulated is observed to have a gel-like consistency and excellent long-term stability. The yield stress of the MR fluid at a particular magnetic field strength is expected to increase as the particle size increases (refer to section 2.1.4) but stability becomes a major concern then (Lemaire *et al.*, 1995). Using a carrier fluid with higher off-state yield stress, for example 25wt% blended grease in silicone oil which has a yield stress,  $\sigma_y \approx 5 Pa$ , instead of 15wt% blended grease, as shown in figure 4.7, can possibly eliminate this problem and will be studied in the future.

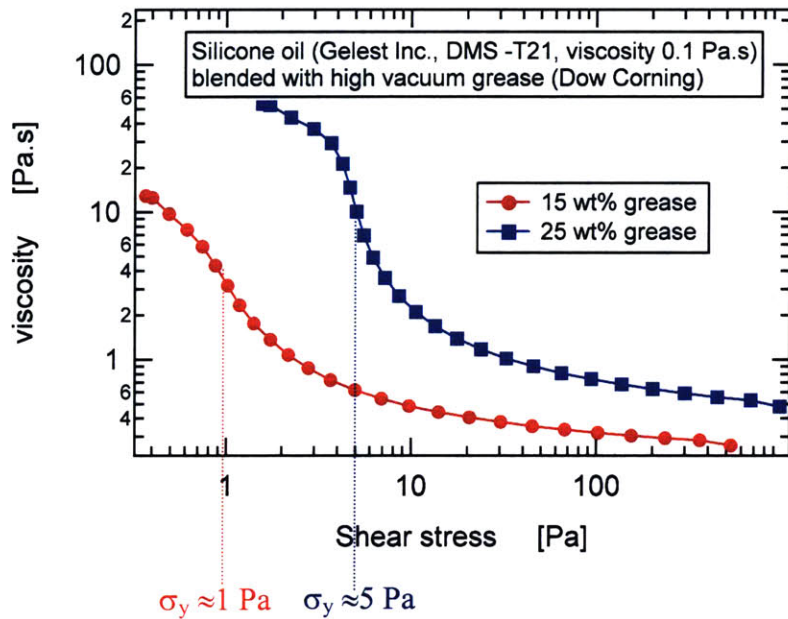


Figure 4.7 Steady shear data for silicone oil blended with grease at different weight fractions illustrating the low but finite yield stress in the field-off state.

The rheology of these laboratory-synthesized fluids in steady shear flow is shown in figure 4.8.

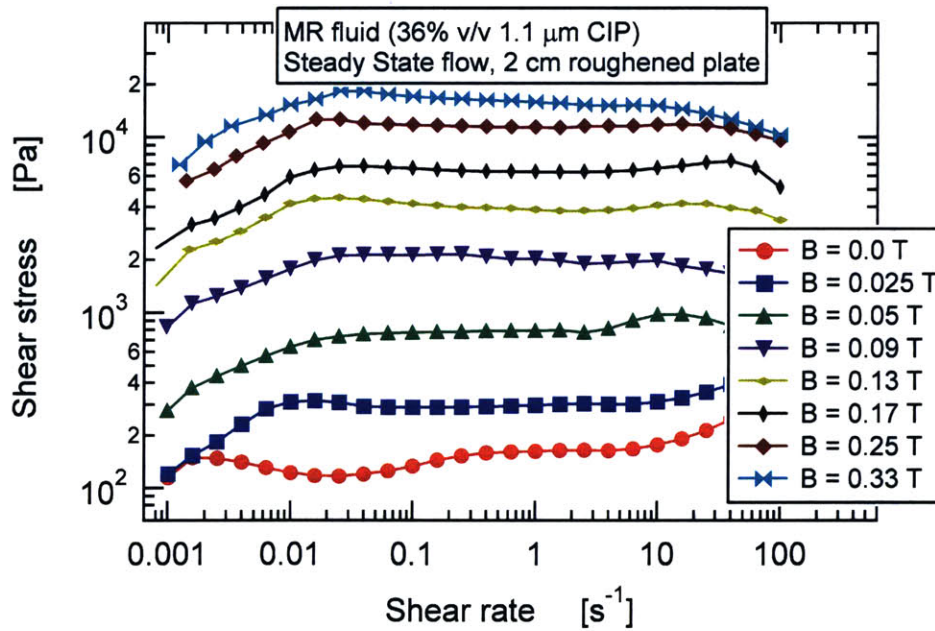


Figure 4.8 MR fluid (36% v/v, 1.1  $\mu\text{m}$  CIP) rheological properties under steady shear flow for different magnetic field strengths.

The experiments have been carried out using 2cm diameter roughened plates and the magnetic field is varied from 0 to 0.33 Tesla. The test protocol used on the AR2000 rheometer is a steady state flow step with the shear rate being controlled and varied from 0.001 to 2000 s<sup>-1</sup>. Five points are measured in a decade range of shear rate with the sample being sheared for 20 seconds before an average value of the torque is recorded. Steady state behavior similar to commercial fluids is seen with the yield stress increasing monotonically with the magnetic field. The shear stress has a constant value for a large shear rate range, which implies a 4-5 orders of magnitude drop in viscosity and also marks the yield stress for the fluid.

#### *4.1.2.3 Yield stress comparison of different MR fluids*

The magnitude of the yield stress of the MR fluid ( $\tau_y(B)$ ) is its defining characteristic for most applications and it can be extracted from the steady shear data as illustrated in figure 4.9. At the yielding point there is a sharp drop in the viscosity due to collapse of particle chains in MR fluids and this stress can be read from the viscosity versus shear stress plots (Barnes, 1999), as depicted below. MR fluids are observed to have a very sharp yield point at which the viscosity drops by 5-7 orders of magnitude. As an example, dotted lines in the figure mark the yield stress values for magnetic fields of 0.09 and 0.17 Tesla. The roughening of plates decreases but does not eliminate slip and at higher shear rates, the material starts apparent violation of the no-slip boundary condition causing the curves to bend over. A lower state viscosity after the yield point thus cannot be measured from these experiments.

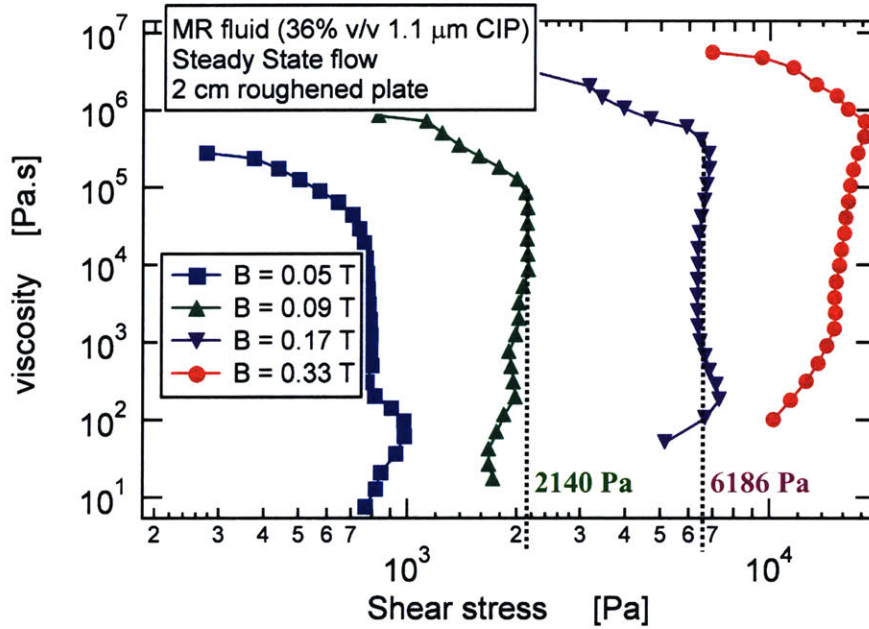


Figure 4.9 Yield stress determination from steady shear rheological properties for MR fluids. The dotted line marks the yield point.

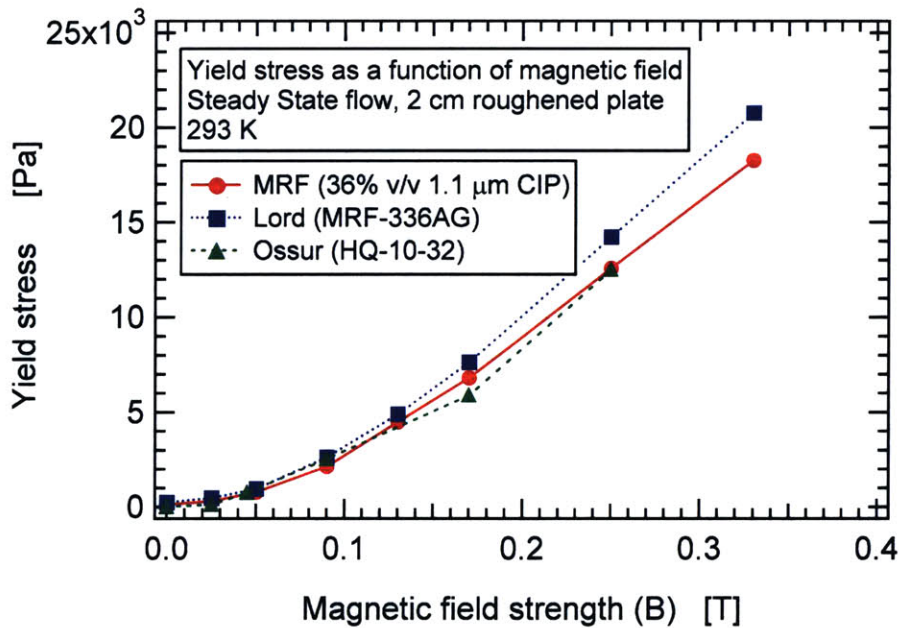


Figure 4.10 Yield stress comparison for the three fluids, two from industrial sources and one synthesized in our laboratory.

The variation in the yield stress calculated for the three fluids is thus found to be comparable (figure 4.10) and slight differences can be attributed to different particle sizes and volume fractions. Yield stress plotted against the magnetic field strength provides valuable information about forces, energy absorption capacity and flow properties of MR fluids and its composites (Klingenberg, 2001; Carlson, 2000; Jolly *et al.*, 1999).

### 4.1.3 Time-dependent rheology: Creep

Viscoelastic properties of a material are dependent on the structure formation (and collapse) of chains of induced dipoles in the case of MR fluids. The creep test is a very useful method of studying them (Li *et al.*, 2002). In a creep experiment, strain is recorded with time at a constant applied shear stress. A yield stress material will creep below the yield point implying that even though for all practical purposes the material does not flow (see Barnes 1999 for further discussion on material flow at the yield stress), the sample shows irreversible plastic deformation in response to the applied stress and the strain increases with time. A part of this time-dependent deformation is recovered when the applied stress is removed which provides a measure of the elastic properties of the material. The most vital information derived from a creep test however is the 'time-response' of the material or the time required for structure formation and deformation in the material. Applications involving impact require a very-fast (millisecond) time response, which makes MR fluids a viable option (Gast and Zukoski, 1989; Parthasarthy and Klingenberg, 1996).

Creep behavior of a MR fluid at an applied shear stress ( $\sigma$ ) below the yield stress ( $\sigma_y$ ) is shown in figure 4.11. The strain increases as the applied stress increases and approaches the yield stress, which is held constant by maintaining field strength of 0.17 Tesla. The magnetic field is applied and maintained at the constant value before the start of the creep test so that the time response for structure deformation and collapse is measured from the creep test. The response time of the material can be obtained from the plot as the time required for the total strain the

reach a steady value. The response time varies from 3-15 milliseconds as the applied stress increases approaching the yield stress.

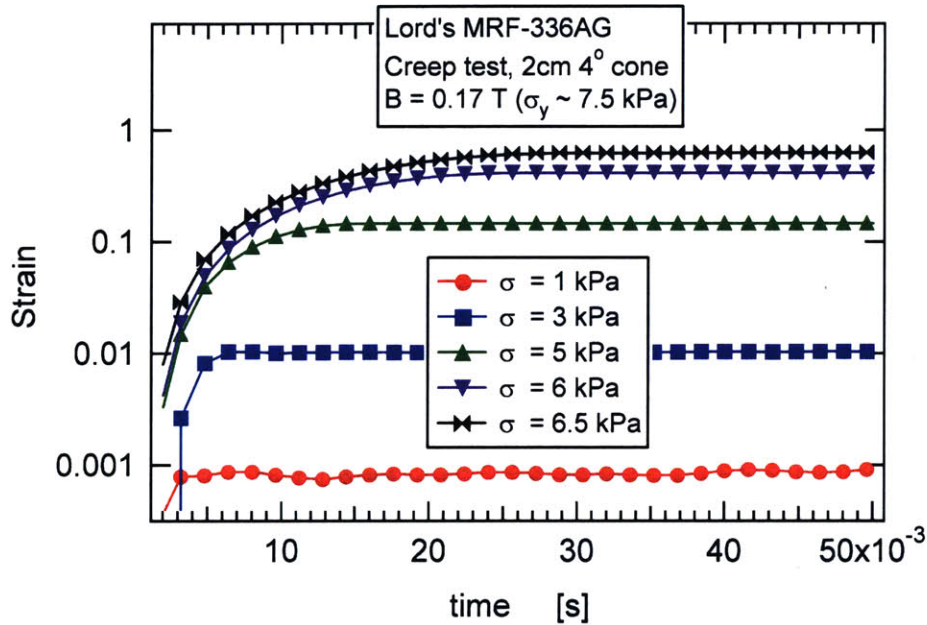


Figure 4.11 Creep behavior of MRF-336AG sample at different applied stresses below the yield stress.

Since, MR fluids have a magnetic field dependent yield stress, a creep experiment wherein the applied stress is held constant but the magnetic field strength is varied such that  $\sigma_y > \sigma$  has also been carried out and is shown in figure 4.12. The short time response of the material when the strain climbs to its steady value is shown in the first section of the figure. The total strain decreases as the magnetic field strength or effectively the yield stress is increased. This suggests a collapse of data with a model considering the total strain as a function of a scaled stress  $s = \left( \frac{\sigma}{\sigma_y} \right)$ , and would be interesting to study in the future. The recovery phase of the fluid after the removal of the applied stress is also shown and is found to be minimal suggesting that the viscoplastic response of fluid is dominant.

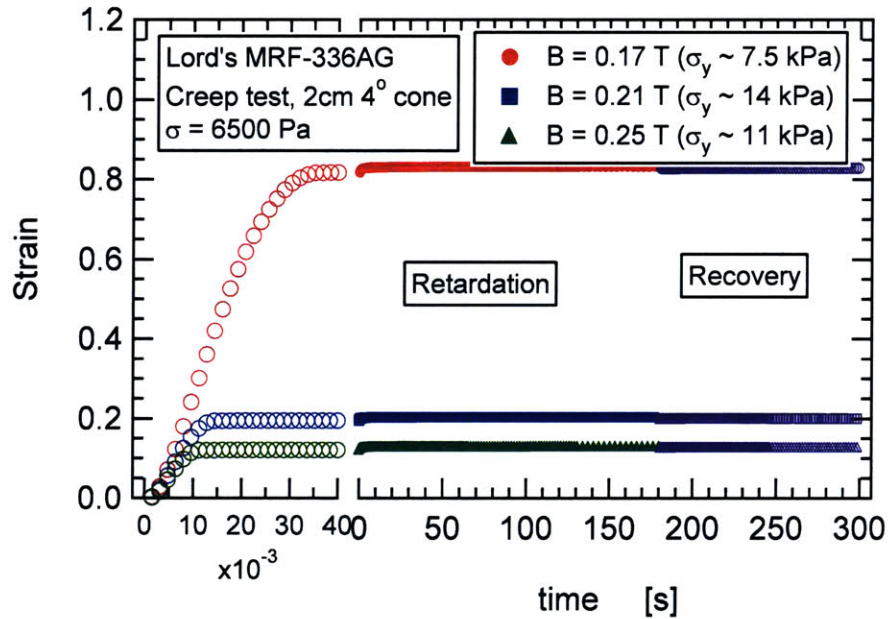


Figure 4.12 Creep experiment for different magnetic field strengths at an applied shear stress showing both the creep and recovery phase.

## 4.2 Shear-Thickening Fluids

The term 'shear-thickening' typically refers to the increase in shear stress or apparent viscosity when the applied shear-rate is increased and these deformation-rate responsive fluids could provide a cheap alternative to magnetorheological fluids for adaptive energy absorption. During impact, shear-thickening fluids can spontaneously (without the presence of an external field) change and show solid-like behavior. Study of rheological properties of shear-thickening fluids is essential for elucidating the subsequent behavior in a composite material.

### 4.2.1 Experimental Methods and Materials

Corn starch has been used for analysis since it shows extreme shear thickening and forms one of the few dispersions that have been reported to show a sharp discontinuity (Hoffman,

1972). Corn starch is used as purchased from Fisher Scientific and deionised water forms the continuous phase in the dispersions.

All rheological measurements have been carried out on TA Instruments' AR 1000N rheometer. A cone and plate arrangement with 4 cm diameter and 2 degree cone angle and 2 cm diameter and 4 degree cone angle has been used for the measurements. The sample was freshly prepared for every run to minimize effects of solvent evaporation, bio-degradation and each sample was pre-sheared to eliminate any time effects. A very high volume fraction of solids in the suspension, an essential condition for shear thickening, has been used.

#### **4.2.2 Steady Shear Rheology**

Corn starch in water at 53 % and 56 % weight fractions has been analyzed under steady shear flow as extreme shear thickening had been observed earlier at these fractions (Hoffman, 1972). A stepped ramp shear flow procedure with a 4cm parallel plate arrangement at a gap of 1mm has been used. The steady shear response (figure 4.13) shows extreme shear thickening with 2-3 orders of magnitude increase in viscosity at a critical shear rate. The jump in viscosity is observed to increase while the critical shear rate decreases as the volume fraction of corn-starch in water is increased. The sharp discontinuity makes data reproducibility in the critical shear rate regime difficult. A number of investigators have reported in the past of marked time-dependence and hysteresis as well as the effects of instrument geometry (Laun et al, 1991, Boersma et al, 1991).



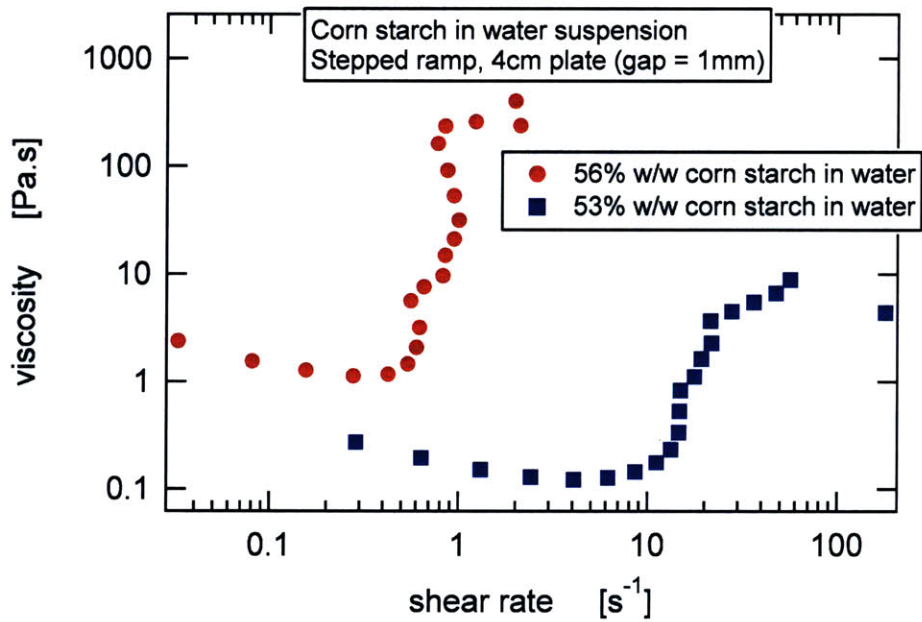


Figure 4.13 Steady shear data for corn starch and water dispersions plotted as viscosity versus shear rate for two different volume fractions.

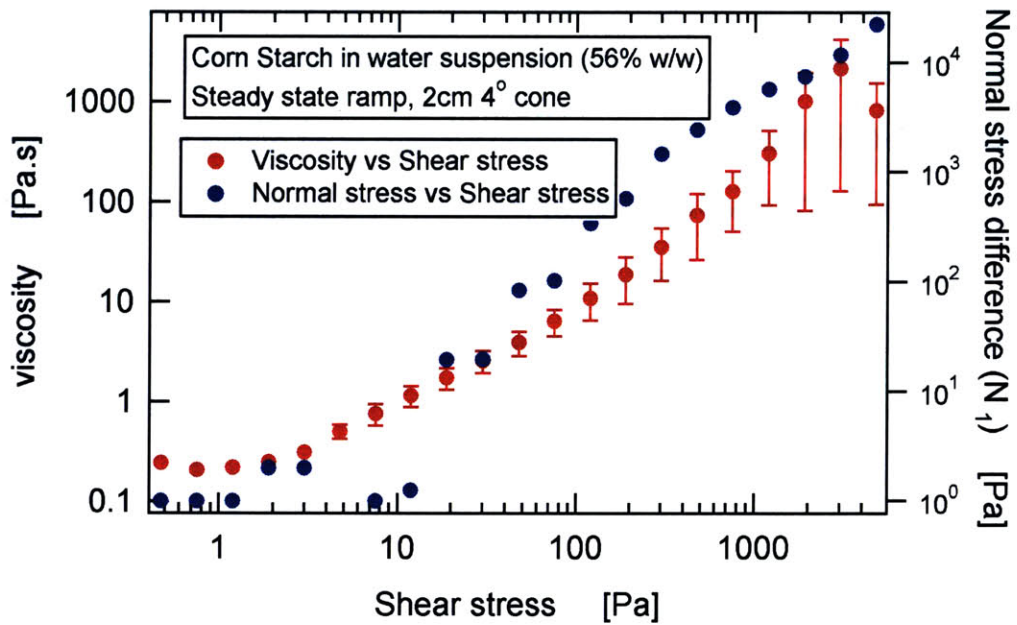


Figure 4.14 Viscosity and normal stress plotted as a function of the shear stress for steady shear flow with a cone-plate arrangement.

Measurements obtained in steady shear flow using a cone-plate arrangement for 56% w/w corn-starch suspension have been plotted as apparent viscosity against shear stress in figure 4.14. The experimental measurements are for a controlled stress ramp with the data being averaged for 20s before recording. The critical shear stress,  $\tau_c \sim 1.5$  Pa is clearly seen in the figure when the viscosity starts climbing up and is reproducible to within 10% error as can be seen from the figure. The first normal stress difference, which has not been reported earlier in literature, also shows a clear trend with an instability, as detected by fluctuations in the stress difference, setting in at the critical shear stress before it starts monotonically increasing.

### 4.2.3 Time-dependent rheology: Creep

Creep tests, recording strain while keeping the applied shear stress constant, have also been carried out to elucidate any time effects in the suspension behavior as shown in figure 4.14. These tests have been carried out with a 2cm  $4^\circ$  cone arrangement and freshly prepared samples.

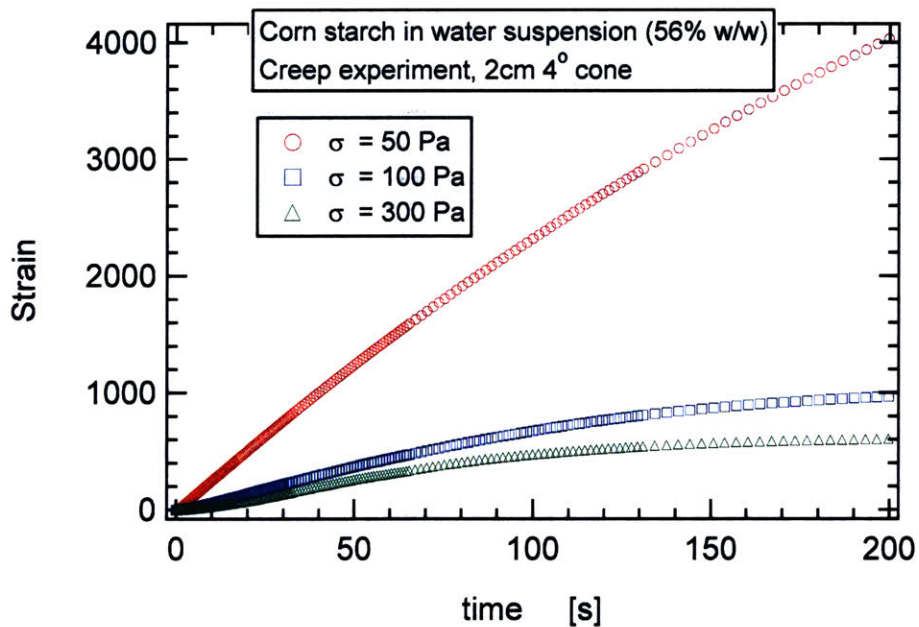


Figure 4.15 Creep experiments for corn starch in water suspensions (56% w/w) illustrating increase in viscosity and decreasing strain with increasing applied shear stress.

Creep results show an increase in viscosity and hence a decrease in the total strain with increase in applied stress. The shear rate  $\left(\dot{\gamma} = \frac{d\gamma}{dt}\right)$  can be approximated as the slope of the curve and is observed to be decreasing with time at the same applied stress. This indicates an increase in viscosity in the corn-starch/ water suspension over long times also known as ‘rheopexy’.

### **4.3 Summary**

Steady shear flow and creep experiments have been carried out on commercial and laboratory-based MR fluids to measure the rheological properties of these field-responsive fluids. Inexpensive MR fluids with excellent stability and yield stress comparable to commercially available fluids have been synthesized in the laboratory and these can now be used as the fluid phase for impregnating open-cell foams for energy absorption studies.

Corn-starch and water suspensions show extreme shear thickening and are easily and cheaply formulated. However, issues of stability and time dependence plague these fluids with ‘rheopexy’ complicating the shear-thickening effect. A synthetic shear-thickening fluid showing extreme shear-thickening, for example fluid based on monodisperse colloidal silica spheres in glycols (Bender and Wagner, 1996), could possibly eliminate these concerns and prove beneficial for energy absorbing applications.

## CHAPTER 5

# Fluid–Filled Cellular Solids: Mechanical Properties and Theoretical Modeling

Open-celled foams impregnated with viscous fluids have different mechanical and thermal properties depending on the viscosity and filling fraction of the fluid. The expulsion of these fluids, as the foam is compressed, increases the stress and the energy dissipated. A novel application of using field responsive fluids to control the energy absorbed by foams is explored and experimental results are discussed in this chapter.

### ***5.1 Experimental Setup: Mechanical Properties***

The Texture Analyzer (TA.XT2i), a programmable ‘low’ strain-rate testing instrument, has been used to characterize dry and fluid–filled foams. ‘Low’ strain rates roughly range from  $10^{-8}$  to  $10^{-2}$  /s and are obtained using laboratory tensile or compression-testing instruments. Impact velocities for auto design or ‘intermediate’ strain rates (up to 40 /s) are obtained using ‘Drop-ball’, Izod impact or servo-hydraulic testing equipment and are discussed in detail in chapter 6.

A fixture for the Texture Analyzer has been designed, as shown in figure 5.1, so that compression studies of foams can be carried out in presence of a pre-set magnetic field. The fixture has been built from cast acrylic for easy visualization and video imaging purposes. The foam is confined in a piston-cylinder type of arrangement, so as to allow fluid flow only in one direction i.e. along the direction of compression and to prevent spontaneous deformation of the material on application of high magnetic field gradients. The Texture Analyzer controls the piston type compression probe and executes user-specified test protocols (constant velocity or constant

strain rate compression protocols) while measuring accurately the force, displacement and other dynamic quantities. A horseshoe type permanent magnet provides the desired magnetic field and can be moved along the vertical direction to obtain magnetic field gradients of varying magnitude along the direction of deformation.

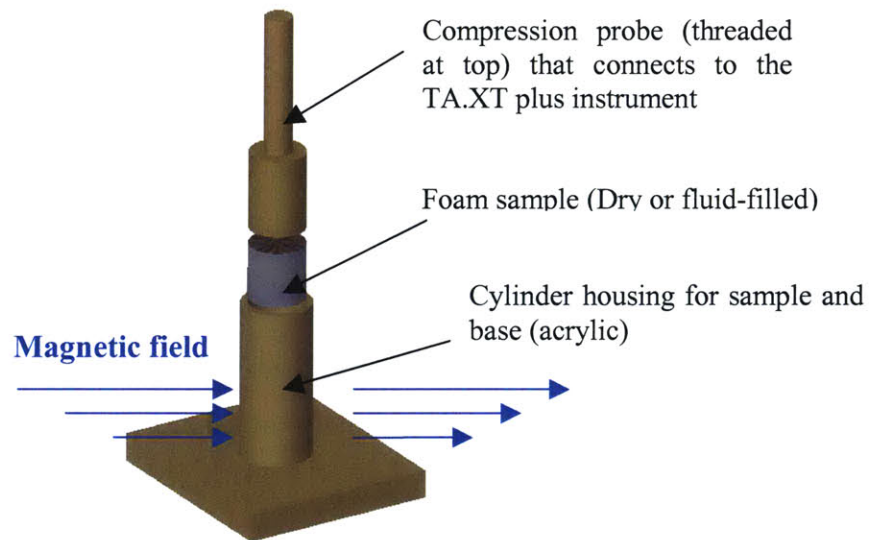


Figure 5.1 TA.XT plus instrument fixture (exploded view) for compression of samples to measure stress, strain and other mechanical properties under different test protocols.

A gaussmeter, F. W. Bell Model 5060, with an axial and transverse probe and a resolution of 1 mT (10 Gauss) has been used to accurately measure the applied magnetic field and its variation with sample height. Representative field gradient profiles used during experiments have been shown in figure 5.2. Figure 5.2a) illustrates a profile that arises as a result of positioning the centerline of magnet, represented by a Y distance of 0.0 cm on the plots, along the top surface of the foam sample giving a high field gradient while figure 5.2b) is obtained when the centerline of the magnet lies exactly in between the top and the bottom surfaces of the sample and is more uniform.

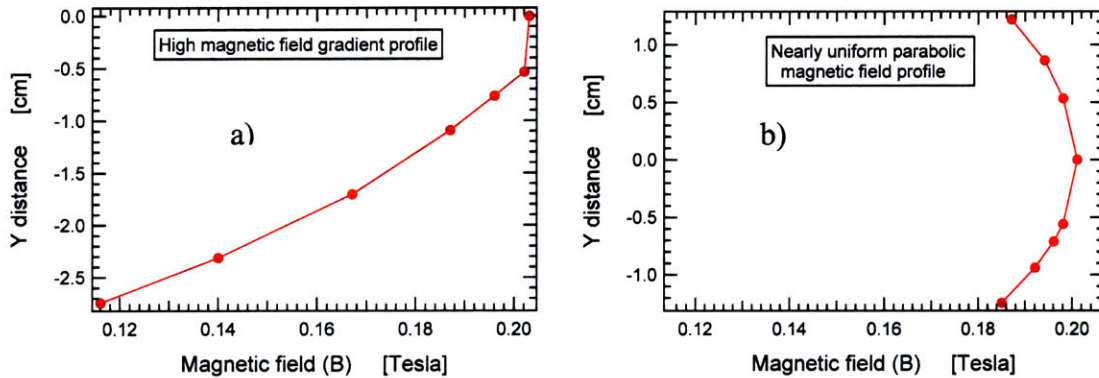
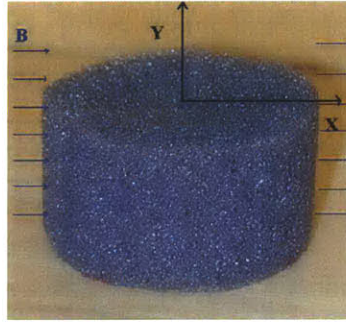


Figure 5.2 Illustrative examples of magnetic field gradients used in experiments, obtained using different arrangements of the magnetic field source a) high field gradient profile b) parabolic but nearly uniform magnetic field profile.

## 5.2 Mechanical Properties: Dry and Impregnated Foams

Cellular solids have widespread use as energy absorbing materials and their mechanical characterization when subjected to deformations is important. Many in depth studies discussing the mechanical properties of ‘dry’ foams (not impregnated with any field responsive fluids and only air fills the porous spaces) exist and these have been reviewed in chapter 3.

### 5.2.1 Dry foams under compression

Stress-strain behavior of ‘dry’ foams has been determined which forms the standard for comparison of fluid-impregnated foam properties. Further, its comparison with literature results has helped validate measurements from this modified instrument setup.

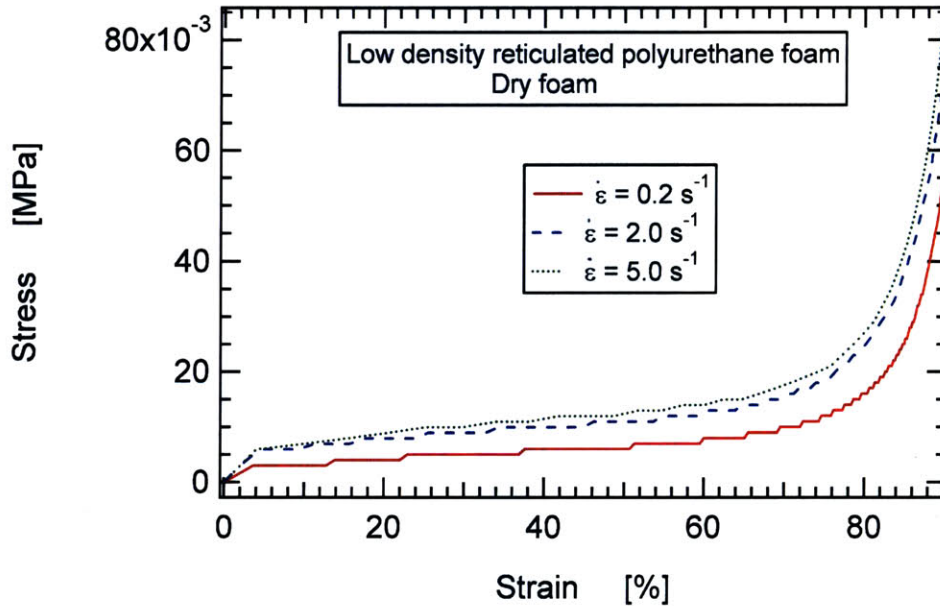


Figure 5.3 Stress-strain curves for a dry reticulated polyurethane foam sample illustrating the dependence on strain rate.

Stress-strain curves for low-density reticulated polyurethane foams in dry condition shown in figure 5.3 are in excellent agreement with the schematic compression curves for elastomeric foams reported earlier in figure 3.3. The foams are flexible and hence have a low compressive strength and a small linear elastic region as can be observed from the figure. The plateau stress is approximately 7 kPa and weakly increases to nearly 10 kPa, with two orders of magnitude increase in strain rate, due to dynamic (inertial) effects discussed in detail earlier in chapter 3.

## 5.2.2 Foams Impregnated with Newtonian Fluids

Newtonian fluids (in general terms, fluids whose viscosity remains constant with shear rate) have been used as reference fluids to characterize the effect of partially impregnating fluids inside a cellular solid. Air, a Newtonian fluid, fills the cellular solid under ordinary conditions but because of its low viscosity has little effect on the stress-strain characteristics of the foam. Glycerol is used as the test fluid, since glycerol-water systems provide access to a large viscosity

range and furthermore glycerol has been studied previously in order to characterize strain-rate dependence of the plateau modulus (figure 3.4).

The cellular solid is impregnated with glycerol by applying suction. Subsequently the fluid is held in place by capillary effects. Squeezing out and sucking in the excess fluid using a compression device repeatedly ensures a homogenous distribution of the fluid impregnating the foam. Since a few non-uniformities are still present, the measured value of stress when the foam is compressed should be considered an average value.

As shown in figure 5.4, glycerol impregnating a cellular solid, at low to medium strain rates, only slightly increases the plateau stress and provides little or no advantage for energy absorption. Also, due to fluid-solid incompressibility effects, the densification region is encountered at much lower strains with increasing volume fraction of glycerol. The reduced densification strain ( $\varepsilon_r$ ) for impregnated foams can be approximated as a function of the volume fraction of the impregnating fluid as follows

$$\varepsilon_r \sim \varepsilon_D (1 - \phi_f) \quad (5.1)$$

where  $\varepsilon_D$  is the densification strain for a 'dry' foam which is derived from classical theory (equation 3.4) and  $\phi_f$  is the fluid volume fraction. The scaling is based on the expression for free volume that determines the densification strain when incompressibility effects set in. The scaled densification strains thus calculated are illustrated in the figure with dotted arrow lines and are within reasonable accuracy of the experimental values.

However, at higher strain rates, the plateau stress is expected to slightly increase due to dynamic crushing and inertial effects of the solid foam structure and thus possibly glycerol-filled foams could provide better energy management or cushioning for a larger dynamic range as compared to commercially available dry foams.



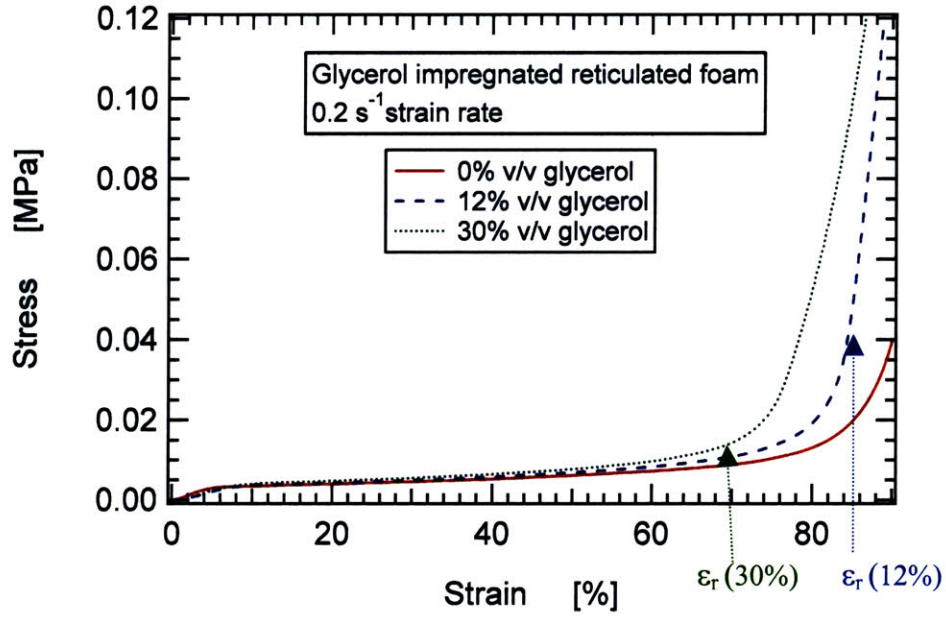


Figure 5.4 Characteristic stress-strain curves for glycerol-filled reticulated foams at varying volume-fractions of the fluid at low strain rates.

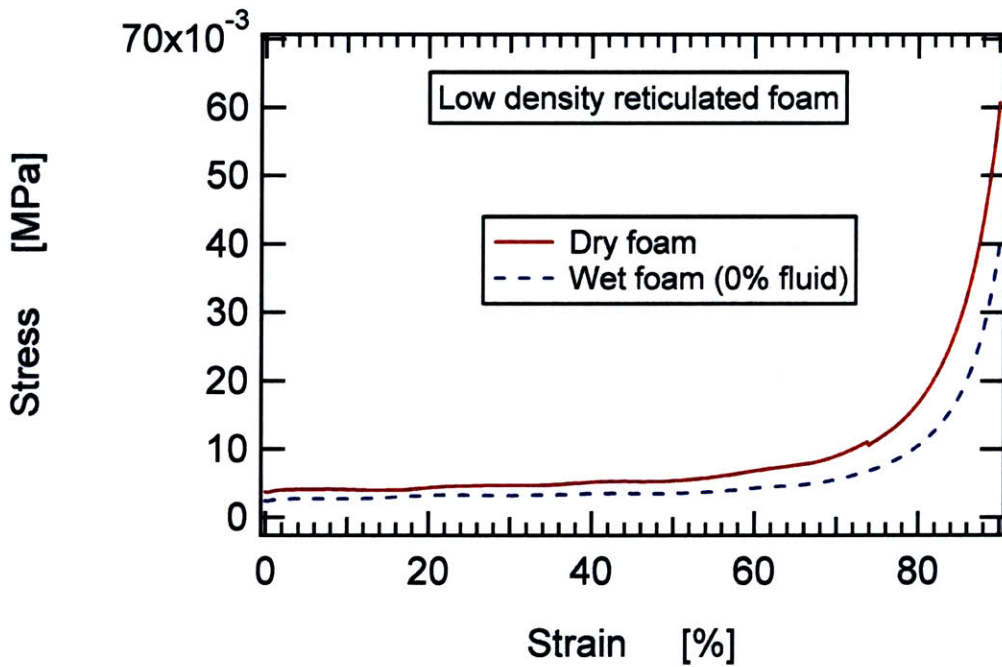


Figure 5.5 Comparison of stress-strain response for low-density reticulated dry and wet foam subjected to a constant strain rate test protocol.

Solid cellular edges of reticulated polyurethane foams, when in contact with small amounts of fluid get softened and are expected to have a lower solid modulus of elasticity ( $E_S$ ). This phenomenon of ‘wetting’ of the solid material present in cell edges leads to a decrease in the plateau stress and hence the ‘wet’ foam has a lower stress-strain curve as shown in figure 5.5. Also, it is observed that the compression apparatus fixture type (whether with or without lateral constraints on the sample side) determines the direction of the fluid flow, either along or normal to the compression direction. Hence all experimental data that follows has been compared to ‘wet’ foam compressed with fluid flow along the same direction.

### 5.2.3 Shear-thickening Fluid Impregnated Foam

Shear-thickening fluids show an increase in viscosity with shear rate as described in detail earlier in section 2.2. The shear-thickening fluid effect showing the sharp jump in viscosity at a critical shear rate is illustrated in figure 5.6.

The internal shear rate ( $\dot{\gamma}$ ) is expected to be a function of the volume fraction ( $\phi$ ) of the fluid, the external deformation rate ( $\dot{\epsilon}$ ) of the foam and the geometry of the foam cells. An approximate analysis by considering the cellular solid to be a bundle of capillaries of diameter ( $d$ ) gives the average velocity as

$$u_{avg} = \phi \dot{\epsilon} (1 - \epsilon) L_0 \quad (5.2)$$

where  $\epsilon$  is the strain in the foam sample and  $L_0$  is the initial height of the sample.

The shear rate of the fluid inside the capillary can then be expressed as

$$\dot{\gamma} = \left( \frac{\partial v_z}{\partial r} \right) \sim \left( \frac{2u_{avg}}{d/2} \right) = \left( \frac{4\phi \dot{\epsilon} (1 - \epsilon) L_0}{d} \right) \quad (5.3)$$

where  $d$  is the characteristic diameter of a cellular solid pore.

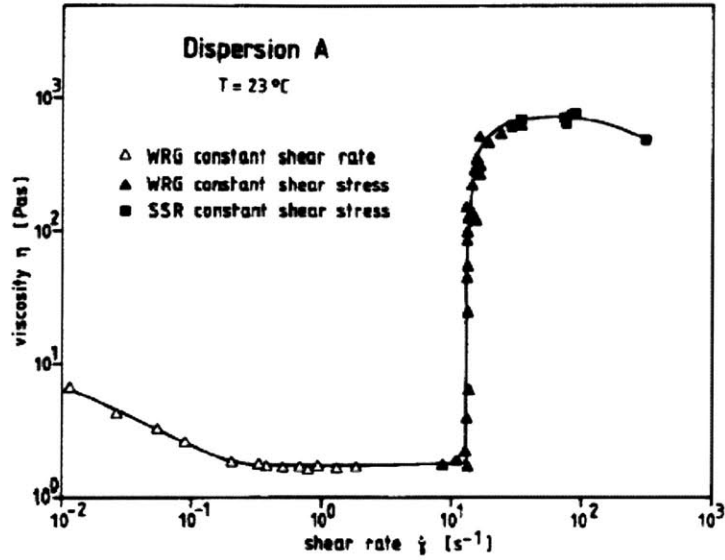


Figure 5.6 Illustrative example of viscosity versus shear rate data for a shear-thickening fluid (Laun *et al.*, 1991).

The energy absorbed by foams impregnated with these fluids under compression will vary as the shear rate of the fluid flowing inside the foam cell changes since it can be expressed per unit volume as

$$\underline{\underline{\tau}} : \underline{\underline{\dot{\gamma}}} = \eta(\dot{\gamma}) \dot{\gamma}^2 \quad (5.4)$$

where  $\underline{\underline{\tau}}$  is the stress tensor,  $\underline{\underline{\dot{\gamma}}}$  is the rate tensor and  $\eta(\dot{\gamma})$  is the shear-rate dependent viscosity (Bird *et al.*, 1987).

If a non-Newtonian fluid is utilized in which viscosity is a function of this shear-rate then we may expect from equations 5.2 and 5.4 that the dissipation rate will increase as the deformation rate of the sample or the volume fraction of the fluid is increased or the cell pore size is decreased.

The stress-strain behavior for shear-thickening fluid impregnated foam as the volume fraction of the fluid increases is shown in figure 5.7. The increase in plateau stress and the energy absorption due to the shear-thickening effect is limited and the densification region is attained at

smaller strains due to fluid incompressibility effects. This is because the critical shear rate ( $\dot{\gamma}_c$ ) for shear-thickening effect to be observed is attained only at very high strains (~95%) as is illustrated below for the 15% v/v STF impregnated foam

$$(1 - \varepsilon_c) = \frac{\dot{\gamma}_c d}{4\phi \dot{\varepsilon} L_0} = \frac{10(0.0003)}{4(0.15)(0.2)(2)(0.0254)} \approx 0.05 \quad (5.5)$$

where  $\varepsilon_c$  is the critical strain for shear-thickening to occur,  $d = 300$  microns is the pore diameter,  $\dot{\varepsilon} = 0.2 \text{ s}^{-1}$  is the strain rate and  $L_0 = 2$  inches is the foam sample height.

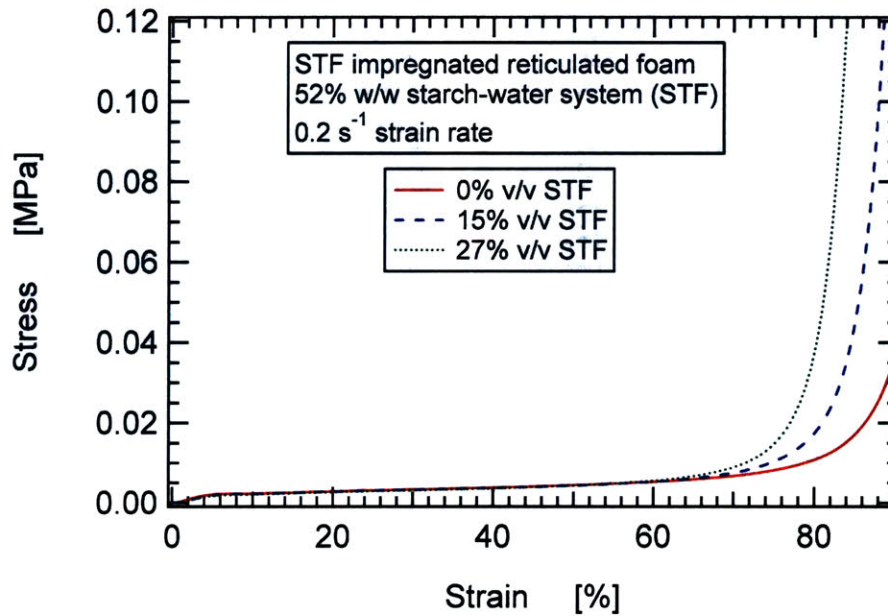


Figure 5.7 Stress-strain behavior of reticulated open-cell foam impregnated with shear-thickening fluid (52% corn-starch/ water solution) at varying volume fractions.

## 5.2.4 Magnetorheological Fluid Impregnated Foam

Magnetorheological fluids are ‘smart fluids’ with controllable yield stress, and these were impregnated in a cellular solid to obtain user-controllable foam characteristics, in particular stress-strain behavior and the energy absorption capacity. The experimental setup, as described in

the section 5.1, allows instrumented studies while varying different control parameters such as strain rate and magnetic field in order to control the mechanical behavior of these foams. Fluid, in the required volume fraction, is impregnated inside the foam by suction and is spatially homogenized by repeated compression and relaxation of the filled foam. The fluid forms a secondary layer covering the solid edges of the foam where it is held in place, owing to its yield stress, as shown in the optical micrograph (figure 5.8). The yield stress of the fluid phase is a function of the magnetic field and hence, the elastic modulus of the composite cell edges can be modulated by changing the magnetic field strength.

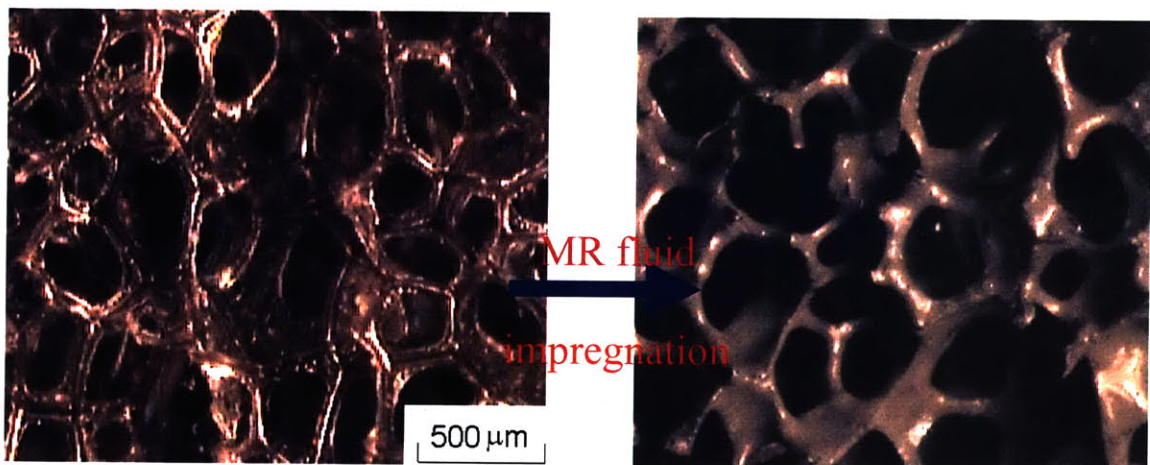


Figure 5.8 Optical micrograph (*Olympus SZX9 microscope*) of a dry low-density reticulated foam before and after impregnation with a commercially available MR fluid (*LORD's MRF-336AG*).

The stress-strain behavior of MRF impregnated foam in the presence of a very low magnetic field is compared with the no-field case in figure 5.9 a). The solid cellular edges of the foam stiffen as the yield stress of the MR fluid increases in presence of a magnetic field and the stress-strain curve shifts upward. The reduced densification strain ( $\epsilon_r$ ) for fluid impregnated foams can be expressed similar to equation 5.1 earlier and is shown in the figure for 12% v/v with

a dotted arrow line. The densification strain ( $\epsilon_D$ ) for 0% v/v fluid in an open cell polyurethane foam works out to be ~98% strain due to a very low solid fraction (~2%) in the cell edges.

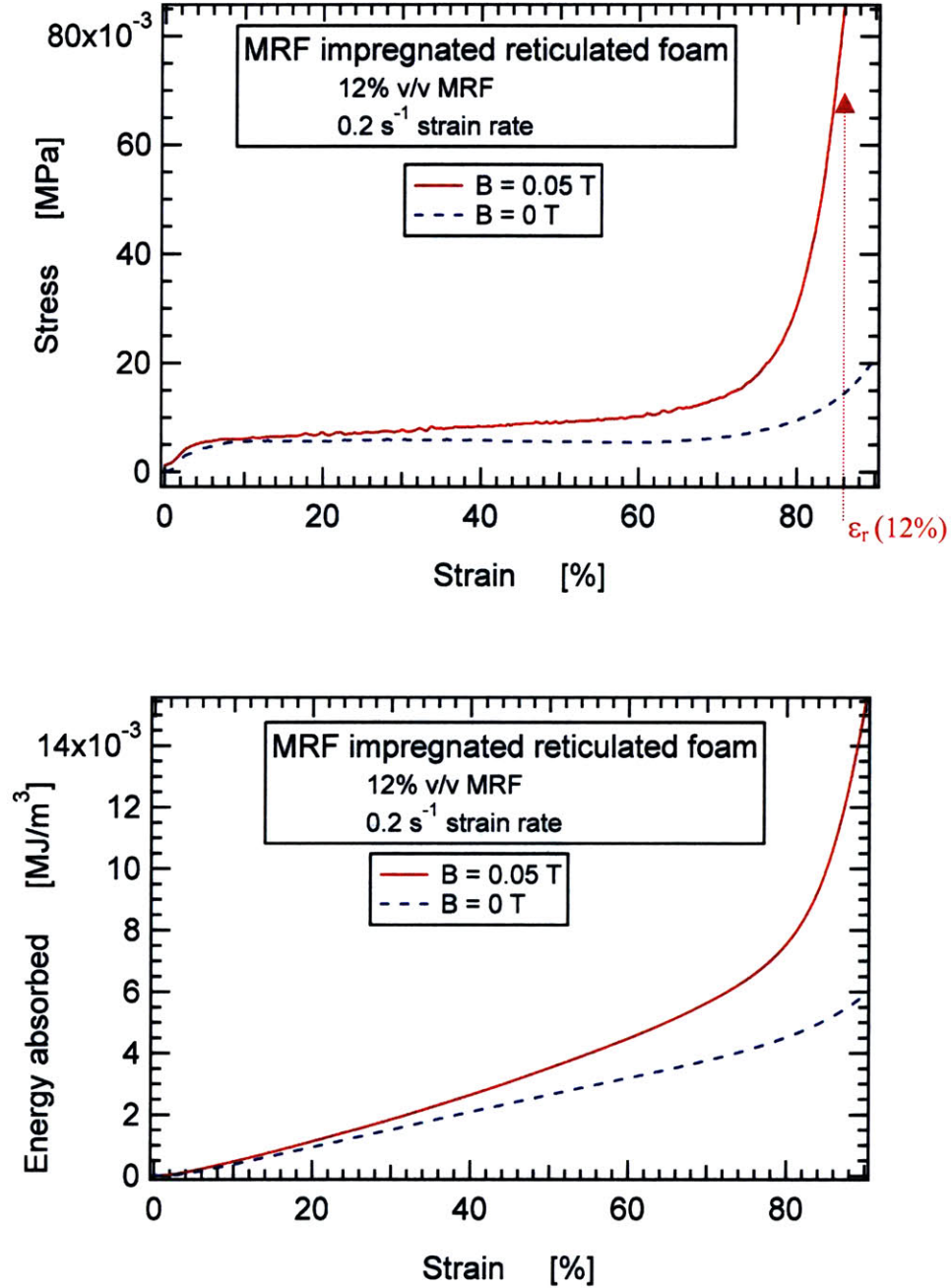


Figure 5.9 MRF impregnated open-cell foam at 12% volume fraction and 0.05 T magnetic field a) stress-strain behavior b) energy absorption curve.

The energy absorbed by this cellular solid is given by the area under the stress-strain curve and is shown in figure 5.9 b). The energy absorbed, even at low volume fractions and magnetic fields, is seen to increase by 40-50% (as compared with the no-field case) well before the densification region is reached.

In the case of glycerol or shear-thickening fluids impregnating the cellular solid, the plateau modulus ( $\sigma^*$ ) hardly changes and only the shift in the densification region is observed. The energy absorption is only due to the viscosity of the flowing fluid (fluid being squeezed out at higher strains) and is thus a strong function of the shear rate. In the case of MR fluid impregnated foams, because of the fluids' yield stress, the cell edges stiffen and the plateau modulus itself increases leading to a dramatic increase in the energy absorption besides the enhancement due to fluid flowing at higher strains. We now proceed to characterize the material response in detail.

### **5.3 'Novel' Energy-Absorbing Material: MRF Impregnated Foam**

A 'smart' energy-absorbing material has thus been conceptualized by using field-responsive fluids such as MR fluids to control the foam characteristics. The important control variables for this novel material are the magnetic field strength ( $B$ ), volume fraction of the fluid ( $\phi$ ), deformation rate ( $\dot{\epsilon}$ ) and the geometrical parameters of the cellular solid. Experiments to determine the material properties under compression have been carried out while varying the different control variables one at a time. Open-cell reticulated polyurethane foam (solid elastic modulus ( $E_s$ ) equal to 45 MPa, density of solid ( $\rho_s$ ) equal to 1200 kg/m<sup>3</sup>, relative density ( $\rho^*/\rho_s$ ) equal to 0.0155, tetrakaidecahedron cells of  $\sim 300$   $\mu\text{m}$  pore size) has been used in all experiments as the control matrix for impregnation by LORD's MRF-336AG to study the effect of parameters.

### 5.3.1 Effect of Magnetic field strength

The magnetic field strength determines the yield stress of the MRF, which in turn controls the plateau modulus ( $\sigma^*$ ) of the composite cellular solid and its energy absorption capacity. Hence, as the magnetic field is increased to moderate levels of  $\sim 0.2$  Tesla, while keeping the volume fraction, strain rate and other parameters constant, the yield stress of the MRF increases sub-quadratically and a progressive shift in the plateau stress is observed. Figure 5.10 depicts this jump and compares it with the stress-strain behavior observed at lower and zero magnetic fields.

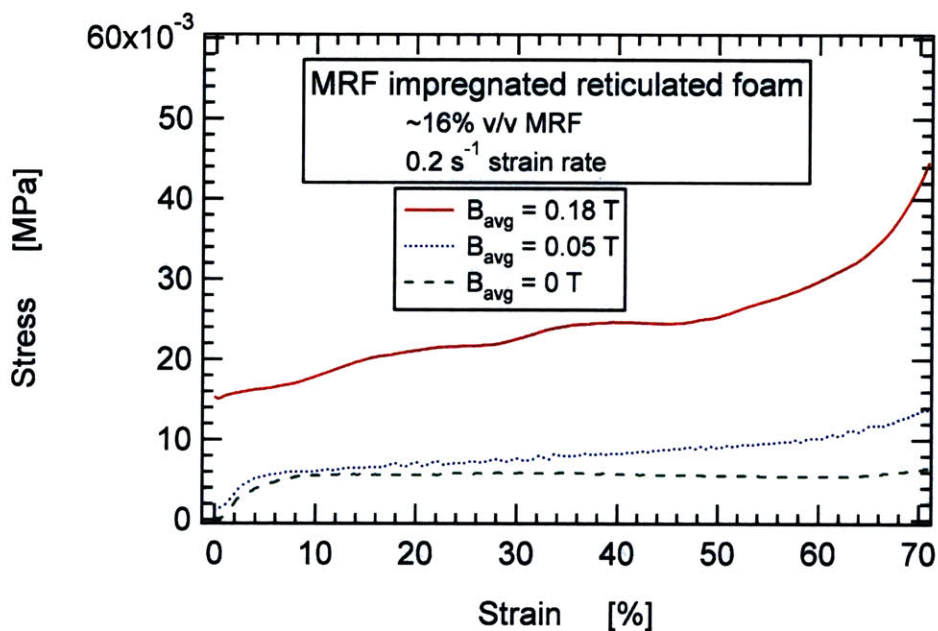


Figure 5.10 Stress-strain curves for varying magnetic field at 16% volume fraction of MR fluid impregnated in open-cell foam.

The energy absorbed by this impregnated foam material even at moderate magnetic fields and low volume fractions of the fluid increases tremendously and can go up by nearly 30-50 times the energy absorbed at zero-field. The energy absorbed by the MRF impregnated foam can



thus be modulated by controlling the magnetic field and figure 5.11 demonstrates this controlled energy absorption for three magnetic field strengths.

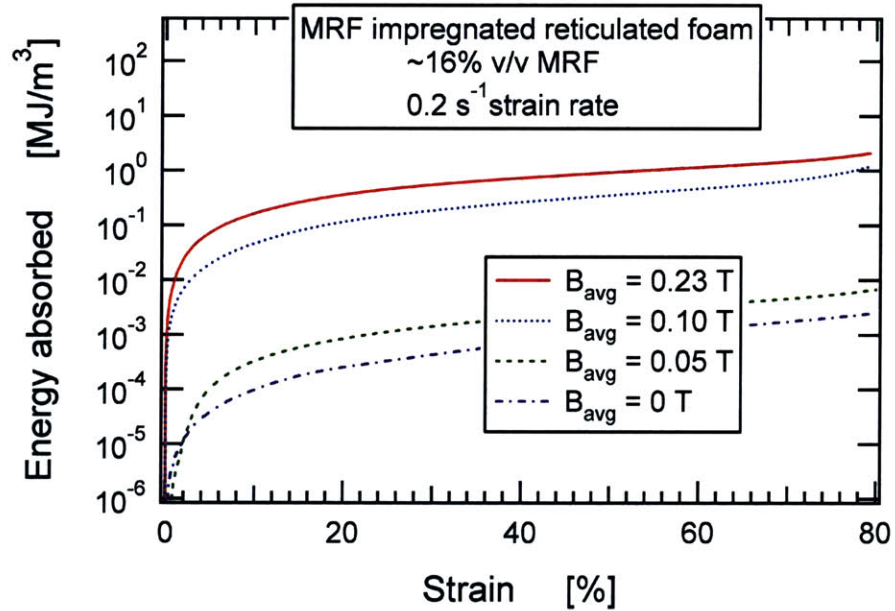


Figure 5.11 Variation of energy absorption capacity by modulating the magnetic field strength for 16% v/v MR fluid-filled open cell foam.

All the experimental results shown above as well as those below have been recorded when a high magnetic field gradient was imposed on the foam sample (as illustrated in figure 5.2 a)) and only the average magnetic field strength is indicated in the plots. The magnetic field gradient is observed to be an important factor determining the stress-strain behavior of the MR fluid-filled foam sample. As the sample is compressed either against or along the magnetic field gradient, an additional force is experienced called the ponderomotive magnetic force. The energy absorption thus varies with strain as the magnetic field profile is changed and figure 5.12 illustrates this difference for an average magnetic field of 0.23 Tesla. Although, the total energy absorption is nearly the same, in case of the uniform magnetic field shown by the blue dotted curve in the figure (profile according to conditions illustrated in figure 5.2 (b)), the plateau region

is absent and the continuously increasing stress is generally not desirable unless a higher dynamic range is required by the application.

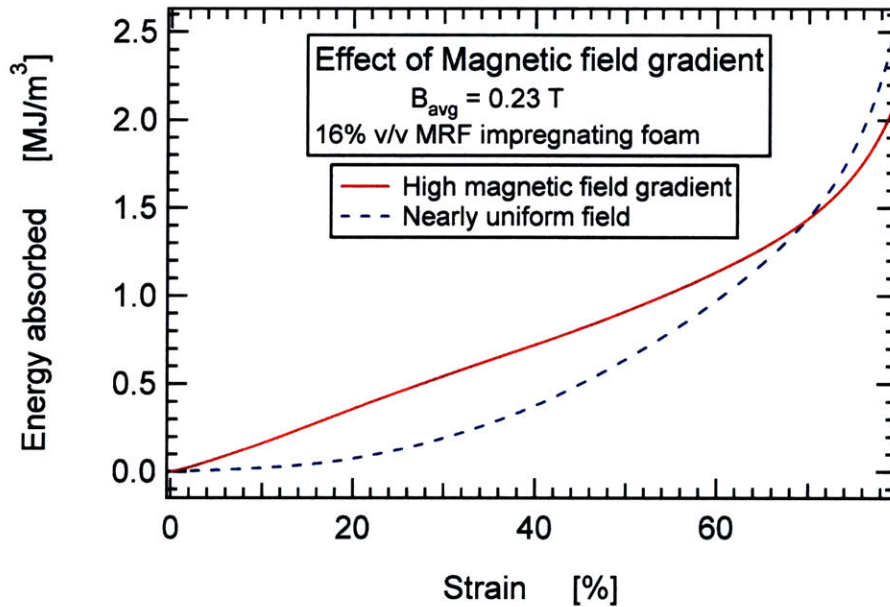


Figure 5.12 Effect of the magnetic field profile (in accordance with the conditions illustrated in figure 5.2 (a) for high magnetic field gradient and figure 5.2 (b) for nearly uniform field) on the amount of energy absorbed by an impregnated foam sample.

Despite the heterogeneity in the MR fluid impregnating the cellular solid, the results are reproducible to a high degree. The Texture Analyzer instrument has a high resolution of  $10^{-6}$  MPa and introduces little error into the result. However, it is highly impractical to have control on the volume fraction of the fluid impregnating the foam as it undergoes compression-relaxation cycles. The fluid is repeatedly squeezed out and sucked in during these cycles and a variation of  $\pm 2\%$  v/v MRF is observed under test conditions. The nature of the stress-strain curve for the material is robust under these conditions and is illustrated for five compression-relaxation cycles in figure 5.13.

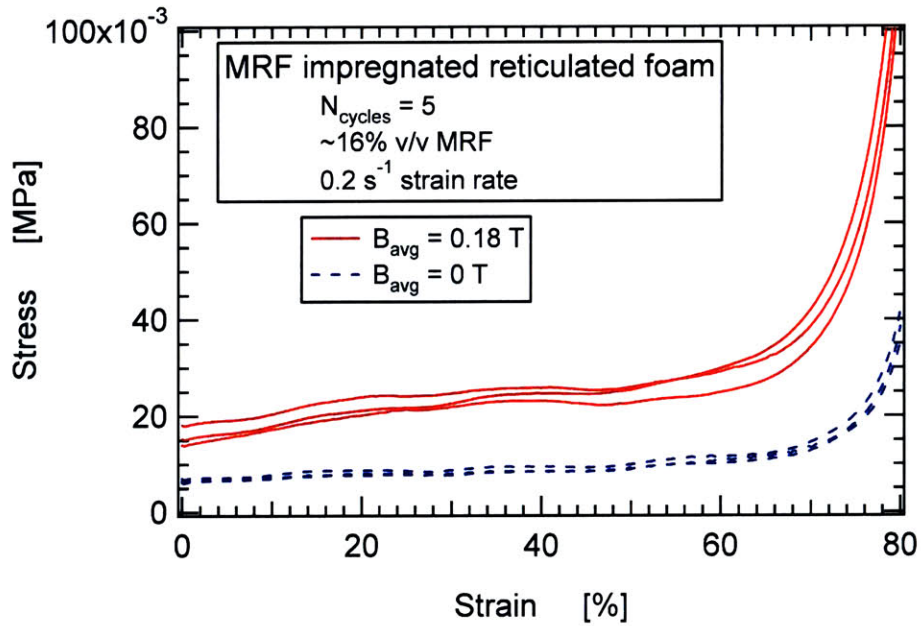


Figure 5.13 Robustness of the mechanical behavior observed for an impregnated foam sample undergoing compression-relaxation and field off-on cycles.

### 5.3.2 Effect of volume fraction of the MR fluid

Varying the volume fraction of the MR fluid impregnating the foam affects the mechanical properties of impregnated foam in two ways. Firstly, it increases the thickness of the secondary layer of MR fluid on the foam edges and hence the plateau stress. Secondly, more fluid needs to be squeezed out as the sample undergoes compression and hence the stress increases at lower densification strains, as illustrated in figure 5.14 for a few volume fractions with dotted arrow lines. These reduced densification strains ( $\epsilon_r$ ) are approximated by scaling the densification strain for ‘dry’ foams by the free volume as described earlier in section 5.2.2.

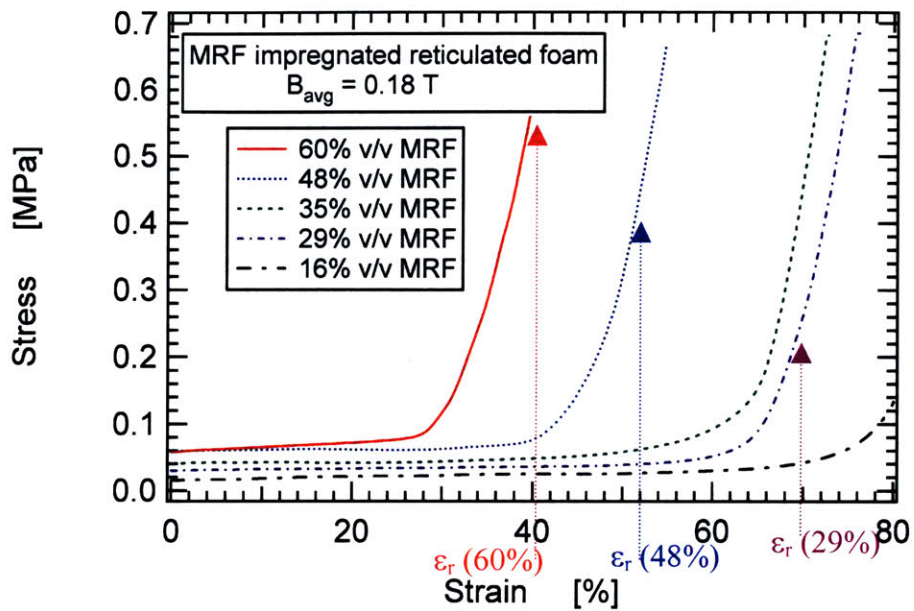


Figure 5.14 Stress-strain curves for MR fluid impregnated foam at 0.18 Tesla (average) depicting increase in the plateau stress ( $\sigma^*$ ) and shift in the densification region as the volume fraction of the fluid is varied from 15 to 60%.

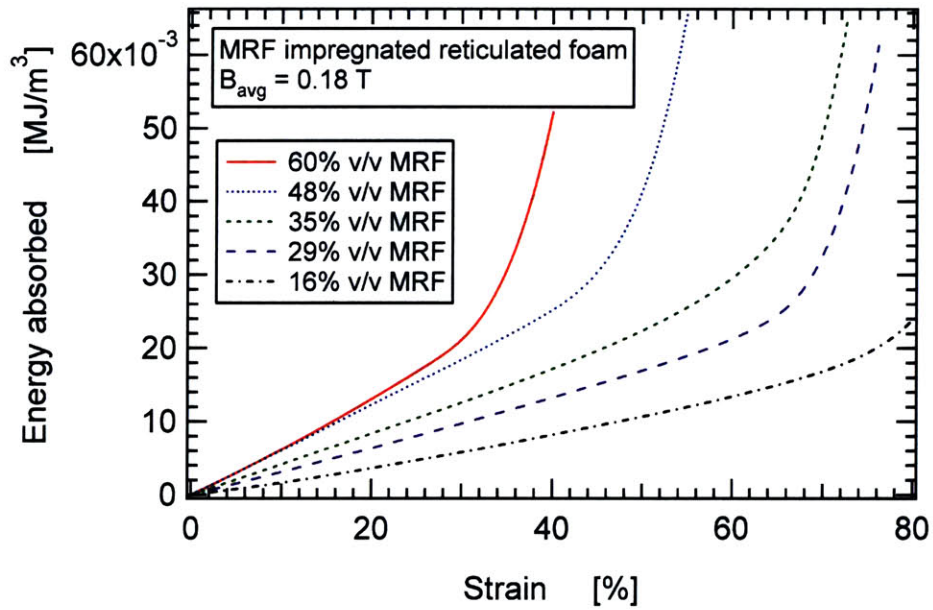


Figure 5.15 Energy absorbed as a function of volume fraction of the MR fluid impregnating the open-cell foam.

The plateau stress increases almost linearly at low volume fractions and the slope of the line is a function of the magnetic field as shown with the model fit later in figure 5.18. The energy absorbed by the material is strongly dependent on the volume fraction as can be observed from figure 5.15. This composite material can be optimized for the volume fraction and magnetic field and its energy absorption capacity can be user-specified using these two control parameters.

### 5.3.3 Effects of strain-rate on mechanical properties

Varying the imposed compressive strain rate ( $\dot{\epsilon}$ ) has minimal effect on the mechanical properties of elastomeric foams (dry or impregnated) at ‘low’ to ‘intermediate’ strain rates, as shown in figure 5.16.

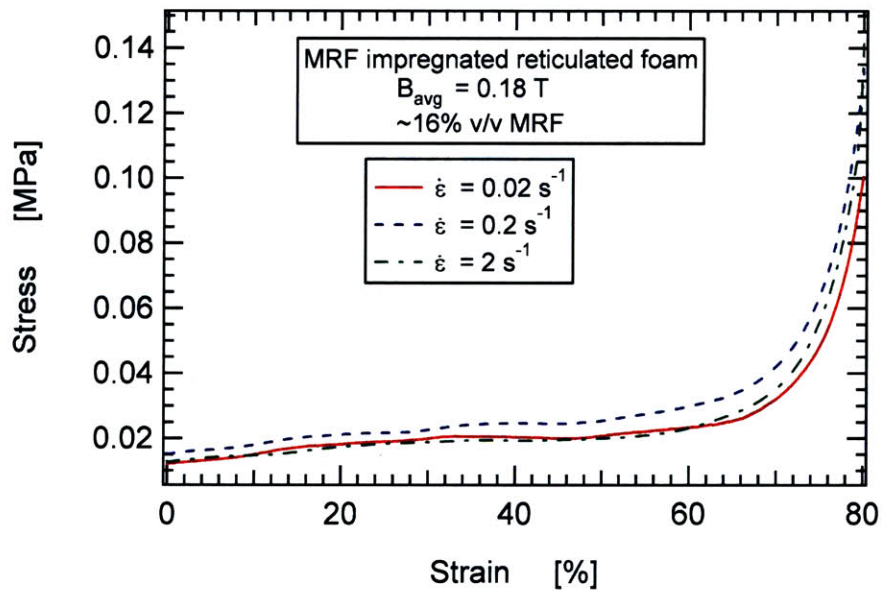


Figure 5.16 Effect of strain rate (‘low’ strain rates) on the stress-strain behavior of MR fluid impregnated reticulated foam.

At higher strain-rates, for example under impact conditions, dynamic (inertial) effects cause the stress-strain curve to shift upwards. This is due to ‘localization’ of stress into a thin band close to the impact face and ‘micro-inertia’ associated with rotation and lateral motion of cell walls when they buckle (Gibson and Ashby, 1997). ‘Drop-ball’ test is a convenient test-

method to realize these auto impact design ('intermediate) strain rates and is discussed in detail in the next chapter.

#### **5.4 Theoretical Modeling: Proposed Scaling Model**

The energy absorption capacity of MR fluid impregnated foam is a complex function of the control variables,  $B$ ,  $\phi$ ,  $\dot{\epsilon}$  and foam-cell parameters. A model in the spirit of the classic scaling model developed by Gibson and Ashby (1997) for dry elastomeric foams is proposed to determine the plateau modulus as a function of the different control parameters. The model, coined the 'two-layer' model, is based on the assumption that a fraction of the MR fluid filling the cellular solid covers its cell edges to form a uniform secondary fluid layer as was also observed in the optical micrographs (figure 5.8). The portion of the impregnated MR fluid volume not forming the secondary layer has little effect on the plateau stress and only shifts the densification region similar to a Newtonian fluid case. The fraction ( $f$ ) is a single fitting parameter that depends on the type and geometry of cellular solid. The model takes into account the changes in the elastic properties and also the geometric parameters, namely  $t$ , thickness and  $l$ , length of the cell edge. The schematic of a typical tetrakaidecahedron cell of impregnated open-cell foam is shown in figure 5.17. The thickness of the cell edge changes from  $t_{dry}$  to  $t_{composite}$  due to fluid impregnation while there is negligible change in length of the cell edge ( $l$ ).

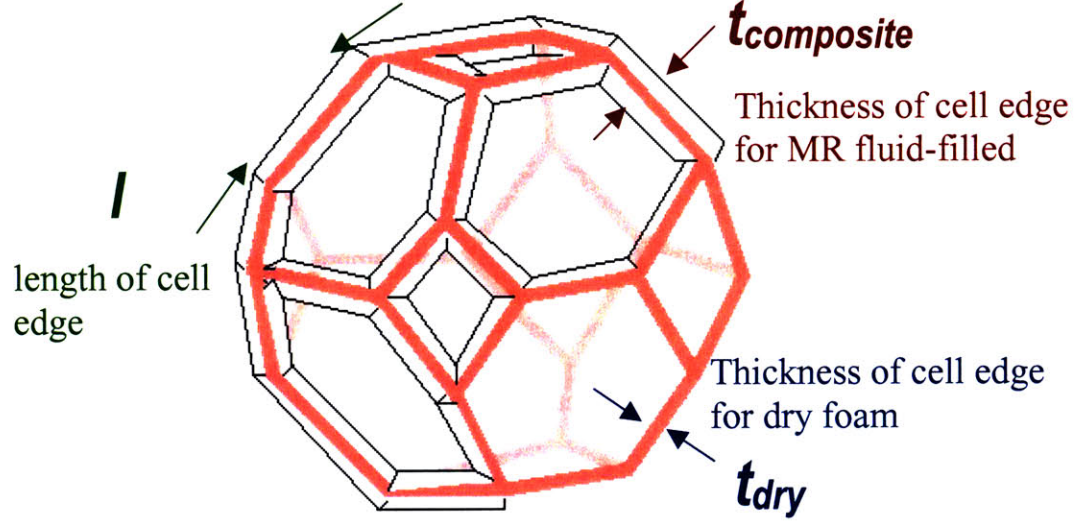


Figure 5.17 Schematic of a single tetrakaidecahedron cell of the MR fluid-foam composite showing a secondary layer of MRF on the solid foam cell edges.

The plateau modulus of open-cell elastomeric dry foam is given by equation 3.2 as

$$\sigma^*_{dry} \propto E_s \left( \frac{\rho^*}{\rho_s} \right)^2 \left[ 1 + \left( \frac{\rho^*}{\rho_s} \right)^{0.5} \right]^2 \quad (5.6)$$

The elastic modulus  $E_s$  of the solid changes as the amount of MR fluid forming the secondary layer on the cell edges varies with  $\phi_f$ . This can be determined by the 'rule of mixtures' for composites as follows

$$E_{composite} = \left( \frac{\phi_s E_s + \phi_f E_{mrf}}{\phi_s + \phi_f} \right) \quad (5.7)$$

$$E_{mrf} \approx 3G_{mrf} (B) \quad \phi_f = f \phi_{mrf}$$

where  $\phi_s$  is the solid volume fraction in cell edges,  $\phi_f$  is the fluid volume fraction in the cell edges,  $\phi_{mrf}$  is the total volume fraction of the MRF impregnating the solid,  $f$  is the fraction of MR fluid located on cell edges,  $E_{mrf}$  is the elastic modulus of the MR fluid and  $G_{mrf}$  is the shear modulus of the MR fluid.

The elastic modulus of the MR fluid  $E_{mrf}$  in the secondary layer can be computed from its shear modulus  $G_{mrf}$ , which is experimentally determined on a rheometer as a function of the magnetic field strength.

Although the elastic modulus of the mixture decreases since  $E_{mrf} < E_s$ , there is an effective increase in the plateau modulus as the relative density of the composite ( $\rho^*/\rho_s$ ) increases according to the following relation

$$\left(\frac{\rho^*_{dry}}{\rho_s}\right) \propto \left(\frac{t_{dry}}{l}\right)^2 \quad \left(\frac{\rho^*_{composite}}{\rho_s}\right) \propto \left(\frac{t_{composite}}{l}\right)^2 \quad (5.8)$$

where  $t_{dry}$  is the thickness of the dry foam cell and  $t_{composite}$  is the thickness of the impregnated foam cell which can be computed from the volume fraction of the MR fluid  $\phi_{mrf}$  as follows

$$\left(\frac{\pi/4(t_{composite})^2 l}{\pi/4(t_{dry})^2 l}\right) \approx \left(\frac{\phi_f + \phi_s}{\phi_s}\right) \quad \left(\frac{t_{composite}}{t_{dry}}\right) \approx \sqrt{\frac{\phi_f + \phi_s}{\phi_s}} \quad (5.9)$$

The plateau stress  $\sigma^*$  can thus be determined as a function of the magnetic field strength  $B$ , volume fraction of the MR fluid covering the cell edges  $\phi_f$  and the plateau stress of the dry cellular solid  $\sigma^*_{dry}$ .



$$\left(\frac{\sigma^*}{\sigma^*_{dry}}\right) = \left(\frac{E_{composite}}{E_s}\right) \left(\frac{\rho^*_{composite}}{\rho^*_{dry}}\right)^2 \left(\frac{1 + \sqrt{\left(\frac{\rho^*_{composite}}{\rho^*_{dry}}\right) \left(\frac{\rho^*_{dry}}{\rho_s}\right)}}{1 + \sqrt{\left(\frac{\rho^*_{dry}}{\rho_s}\right)}}\right)^2 \quad (5.10)$$

$$\left(\frac{E_{composite}}{E_s}\right) = \left(\frac{1 + \left(\frac{\phi_f}{\phi_s}\right) \left(\frac{3G_{mrf}}{E_s}\right)}{1 + \left(\frac{\phi_f}{\phi_s}\right)}\right) \quad \left(\frac{\rho^*_{composite}}{\rho^*_{dry}}\right) = 1 + \frac{\phi_f}{\phi_s}$$

where the *dry* values depend on the open-cell structure and solid material.

At low volume fractions of the MR fluid, this plateau stress  $\sigma^*$  can be shown to vary almost linearly with the volume fraction ( $\phi_f$ ) as is also observed in figure 5.18 below. For collapse of data onto a single curve a shift factor ( $a_f$ ) is thus defined as follows

$$a_f = \left(\frac{\sigma^*}{\sigma^*_{dry}}\right) = \zeta \left[1 + C_1(\zeta - 1)\right] \left[\frac{1 + \sqrt{C_2 \zeta}}{1 + \sqrt{C_2}}\right] \quad (5.11)$$

where  $\zeta = 1 + \frac{\phi_f}{\phi_s}$ ,  $C_1$  is a function of  $B$  and  $E_s$  and  $C_2$  depends on the foam

structure.

A ponderomotive magnetic force is exerted on the foam sample due to the presence of a magnetic field gradient. This also shifts the plateau stress according to the following expression:

$$f_v = \left(\frac{\chi}{\mu_0}\right) B_{avg} \frac{dB}{dz} \quad (5.12)$$

where  $f_v$  is the force exerted per unit volume,  $\chi$  is the magnetic susceptibility of the composite material,  $\mu_0$  is the magnetic permeability of free space and  $(dB/dz)$  is the magnetic field gradient experienced by the sample.

The plateau stress can thus be expressed as a sum of these two effects as follows

$$\sigma^*_{observed} = \sigma^* + \left( f_v \left( \frac{V}{A} \right) \right) \quad (5.13)$$

$$\sigma^* = a_f \sigma^*_{dry}$$

where  $\sigma^*_{observed}$  is the observed plateau stress value,  $a_f$  is the shift factor from equation 5.11,  $f_v$  is the ponderomotive magnetic force per unit volume obtain from equation 5.12,  $V$  is the total volume of MR fluid in the sample and  $A$  is the cross-sectional area of the foam. The stress part due to the ponderomotive force can be expressed in terms of volume fraction of MR fluid ( $\phi_{mrf}$ ) and the magnetic field as follows

$$\left( f_v \frac{V}{A} \right) = \left( \frac{\chi}{\mu_0} \right) \left( B_{avg} \frac{dB}{dz} \right) (\phi_{mrf} H_0) \quad (5.14)$$

where  $H_0$  is the height of the foam sample,  $\chi = 5$  for a MR fluid and  $\mu_0 = 4\pi \times 10^{-7}$  is the permeability of free space. Model fit to experimentally observed plateau stress values based on calculations shown above for different volume fractions and magnetic fields are shown in figure 5.18.

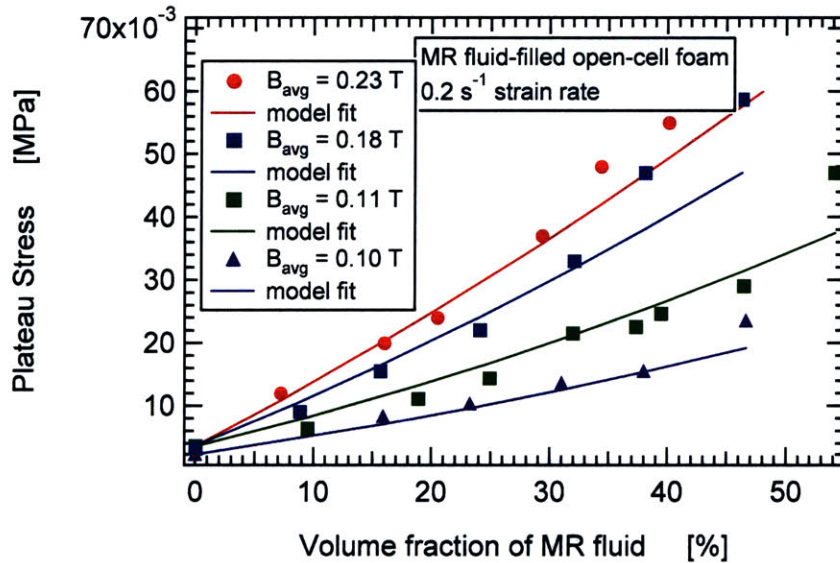


Figure 5.18 'Two-layer' model fit to observed values of the plateau stress for MR fluid-filled open-cell foam samples.

Since, the plateau region is much larger than the linear elastic region in reticulated polyurethane foam samples, it is possible to shift all the stress-strain curves to a single volume fraction. All the data has been collapsed onto a single curve using expressions for shift factor ( $a_f$ ) and ponderomotive magnetic force ( $f_v$ ) and figure 5.19 illustrates this stress shifting for different volume fractions and two magnetic fields. A single plateau stress curve is observed until the densification region thus validating the model propositions.

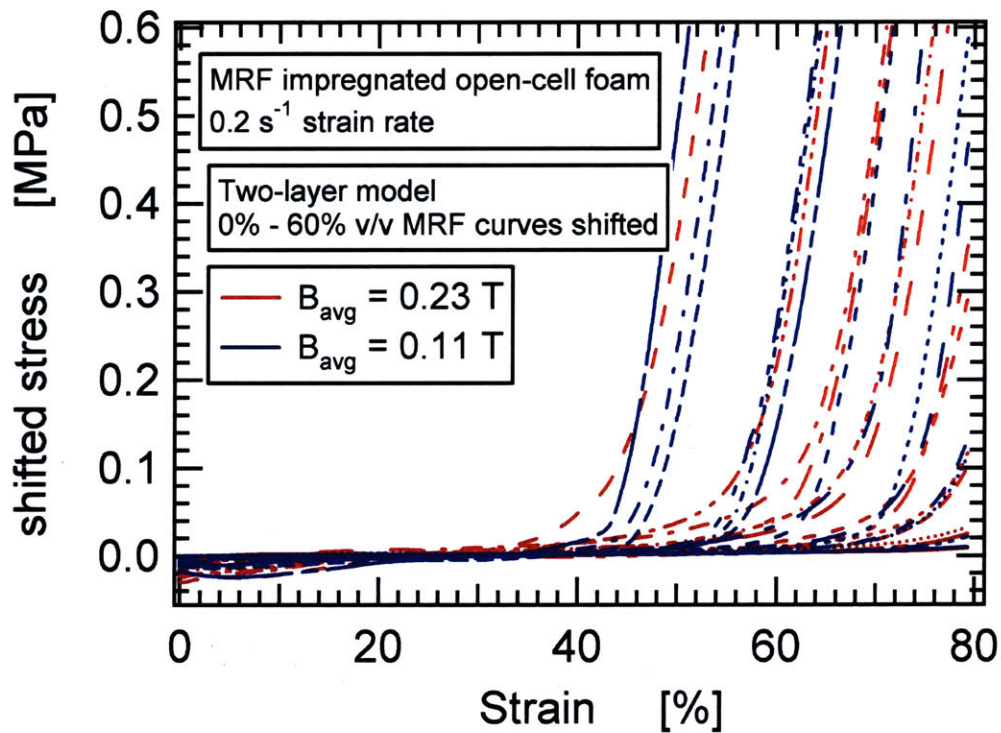


Figure 5.19 ‘Two-layer’ model based stress shift to dry foam plateau stress ( $\sigma^*_{dry}$ ) for 0% to 60% v/v MR fluid impregnated foam.

The shift in plateau stress, however, does not take into account the densification region, which is also a function of the volume fraction of the MR fluid. As the amount of fluid impregnating the cellular solid changes the strain can be scaled in accordance with the free volume available for compression as follows

$$\varepsilon_r = \left( \frac{\varepsilon}{1 - \phi_s \zeta} \right) \quad (5.15)$$

where  $\varepsilon_r$  is the scaled or ‘reduced’ strain,  $\phi_s$  is the solid volume fraction and  $\phi_f$  is the MR fluid volume fraction in the composite. The reduced strain against the shifted stress for different volume fractions of MR fluid impregnating the foam at a field strength of 0.18 Tesla is illustrated in figure 5.20.

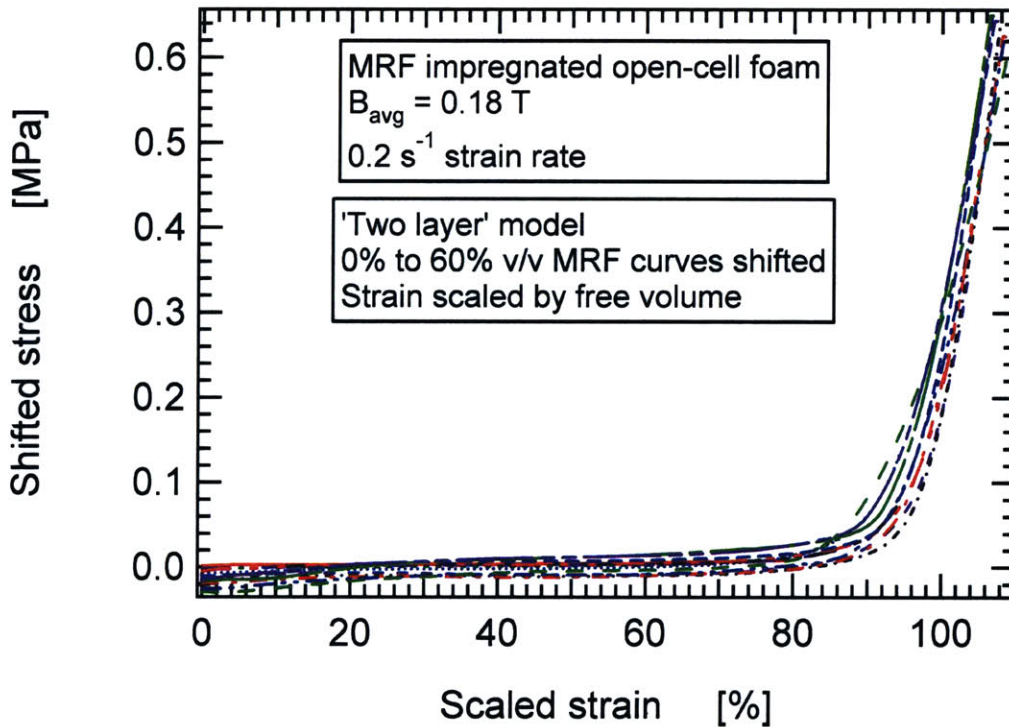


Figure 5.20 Master curve for all control variables using the ‘two-layer’ model.

Thus a master curve has been obtained as a consequence of the ‘two-layer’ model which shows excellent agreement between the experimental data and the theoretical. It can be used to determine the mechanical properties of MR fluid impregnated foams for different parameter values, like  $B$ ,  $\phi_{mrf}$  etc. and also provides an effective tool for optimizing the energy absorption capacity in tune with any application requirements. As a case example in order to explain the

procedure, the observed plateau stress value ( $\sigma^*_{observed}$ ) for a reticulated polyurethane foam impregnated with MR fluid at a volume fraction ( $\phi_{mrf}$ ) of 31% when an average magnetic field ( $B_{avg}$ ) of 0.10 Tesla has been applied will be determined from this master curve. First the shift factor ( $a_f$ ) is calculated from equation 5.10 as follows

$$\begin{aligned} \left( \frac{\rho^*_{composite}}{\rho^*_{dry}} \right) &= \zeta = 1 + \frac{\phi_f}{\phi_s} = 1 + \frac{f\phi_{mrf}}{\phi_s} = 1 + \frac{0.1(0.31)}{0.0145} = 2.78 \\ \left( \frac{E_{composite}}{E_s} \right) &= \left( \frac{1 + (\zeta - 1) \left( \frac{3G_{mrf}}{E_s} \right)}{\zeta} \right) = \frac{1 + 1.78 \left( \frac{3(2.3)}{45} \right)}{2.78} = 0.458 \\ a_f &= \left( \frac{\sigma^*}{\sigma^*_{dry}} \right) = \left( \frac{E_{composite}}{E_s} \right) \left( \frac{\rho^*_{composite}}{\rho^*_{dry}} \right)^2 \left( \frac{1 + \sqrt{\left( \frac{\rho^*_{composite}}{\rho^*_{dry}} \right) \left( \frac{\rho^*_{dry}}{\rho_s} \right)}}{1 + \sqrt{\left( \frac{\rho^*_{dry}}{\rho_s} \right)}} \right)^2 \quad (5.16) \\ a_f &= 0.458(2.78)^2 \left( \frac{1 + \sqrt{2.78(0.0155)}}{1 + \sqrt{0.0155}} \right) = 4.076 \\ \sigma^* &= a_f (\sigma^*_{dry}) = 4.076(0.00225) = 0.009172 \text{ MPa} \end{aligned}$$

where  $f = 0.1$  is the fitting parameter assuming about 10% of the total volume fraction of MR fluid coats the cell edges,  $\phi_s = 0.0145$  is the solids volume fraction in a reticulated polyurethane foam sample,  $G_{mrf} = 2.3$  MPa is the shear modulus of MR fluid at 0.1 Tesla field,  $E_s = 45$  MPa is the solid elastic modulus of flexible polyurethane and  $\sigma^*_{dry} = 0.00225$  MPa is the plateau modulus for 0% volume fraction of MR fluid impregnating the foam. Hence, the first part of the plateau stress has been calculated from the shift factor and material properties and the second part, the ponderomotive magnetic force based on equation 5.14 is calculated as follows

$$\begin{aligned} \left( f_v \frac{V}{A} \right) &= \left( \frac{\chi}{\mu_0} \right) \left( B_{avg} \frac{dB}{dz} \right) (\phi_{mrf} H_0) \\ \left( f_v \frac{V}{A} \right) &= \left( \frac{5}{4\pi \times 10^{-7}} \right) \left( 0.1 \left( \frac{0.03}{0.0254} \right) \right) (0.31(0.0254)) \times 10^{-6} \text{ MPa} \\ \left( f_v \frac{V}{A} \right) &= 0.003368 \text{ MPa} \end{aligned} \quad (5.17)$$

where  $\chi = 5$  is the magnetic susceptibility of MR fluid,  $\mu_0$  is the magnetic permeability of free space,  $\frac{dB}{dz}$  is the magnetic field gradient observed over 1.0 inch height of the sample and  $H_0 = 0.0254$  m is the initial height of the foam sample. Thus, the observed plateau stress can be calculated to be

$$\sigma^*_{observed} = 0.009172 + 0.003368 = 0.01254 \text{ MPa} \quad (5.18)$$

The experimental value for this particular case from figure 5.18 is 0.0136 MPa. Hence, the plateau stress value for a given volume fraction and magnetic field has been obtained from the master curve and the scaling model within 8% error which is a good engineering estimate.

## 5.5 Summary

Texture Analyzer with a custom-built fixture has been used for dry and fluid-filled cellular solid characterization at low strain rates. Magnetorheological fluid-filled foams have magnetic field dependent controllable stiffness and energy absorption. Volume fraction of the fluid impregnating the foam controls the densification region and to a small extent the plateau stress while the strain rate has insignificant effects on energy absorption. A scaling model has been proposed for the plateau stress, which assumes on the basis of micrographs and comparison of data on glycerol and shear-thickening fluid impregnated foams that MR fluid, due to its field-dependent yield stress, forms a secondary layer on the foam edges. The magnetic field gradient is also important as a negative gradient induces a ponderomotive magnetic force, which adds to the amount of energy absorption. Excellent collapse of experimental data onto a single master curve

is observed using these theoretical propositions. Thus, a novel adaptive energy absorbing material has been conceptualized, tested and modeled successfully for use in automotive applications.

## CHAPTER 6

### Applications: Concept and Design

'Smart' materials can be controlled through associated electronics and control algorithms to change their rheological properties in response to the environment. A 'smart' energy-absorbing material consisting of a cellular solid impregnated with a field-responsive fluid impregnated cellular solid has been conceptualized and tested in the previous chapter. The present chapter deals with potential applications in design and concept, which utilize the controllable stiffness and energy-absorbing properties of such a 'smart' material, especially automotive components and ballistic armor.

#### **6.1 Application Potential**

New incoming Federal and European community legislations (FMVSS 201/202, EURO NCAP, EEVC WG 17) introduce stringent impact protection requirements and this is a major concern in the automotive industry (Ullrich 2001). The automobile parts need to provide protection for two distinctly different sizes (adult and child) of pedestrian and passenger, which presents many 'conflict areas' with different stiffness requirements under different conditions (Courtney and Oyadiji 2001). This 'conflict of stiffness' problem is also evident in other components due to varying design, utility and impact absorption requirements (Ullrich 2001).

The 'smart' material conceptualized in the present work because of its adaptive properties could prove beneficial in overcoming the energy absorption conflicts and challenges in the automobile. Various automotive components have been designed using this 'novel' material and are discussed in the following sections.



## 6.2 Impact absorbing Headrest

Whiplash injuries to a passenger in a rear-end crash result in a total annual cost of \$5.2 billion to the automotive industry<sup>1</sup>. Many of these associated disorders could be mitigated if the occupant head acceleration and motion is reduced. The neck injury criterion (NIC) is hypothesized to be

$$NIC = (a_{rel} * 0.2) + (v_{rel})^2 > 15 \text{ m}^2/\text{s}^2 \quad (1.1)$$

where  $a_{rel}$  and  $v_{rel}$  are the relative T1-C1 vertebrae acceleration and velocity (Bostrom *et al.*, 2000).

Seat-back and head-restraint properties influence the head-neck relative movement and acceleration and the forward rebound into the seat belt during rear impacts (Svensson *et al.*, 1996). A soft compliant headrest though comfortable would imply a high risk for injury because of large relative motion between the occupant head and leading to a NIC value greater than 15. A field-responsive fluid-impregnated headrest would allow the same headrest to be soft under normal driving conditions but a high impact energy absorbing stiff material during a crash.

The impact-absorbing headrest with the supporting electronics is depicted in figure 6.1(a). As an example of the concept, referring to figure 6.1(b), a zero field under ordinary conditions would ensure the headrest is compliant and follows the dotted curve but a crash, through associated electronics, would trigger a high field of ~0.2 Tesla for 150-200 milliseconds in the headrest area so that the solid red curve is followed and headrest drastically reduces occupant acceleration and movement.

---

<sup>1</sup> <http://www.nhtsa.dot.gov/cars/rules/CrashWorthy/status9.html#13>

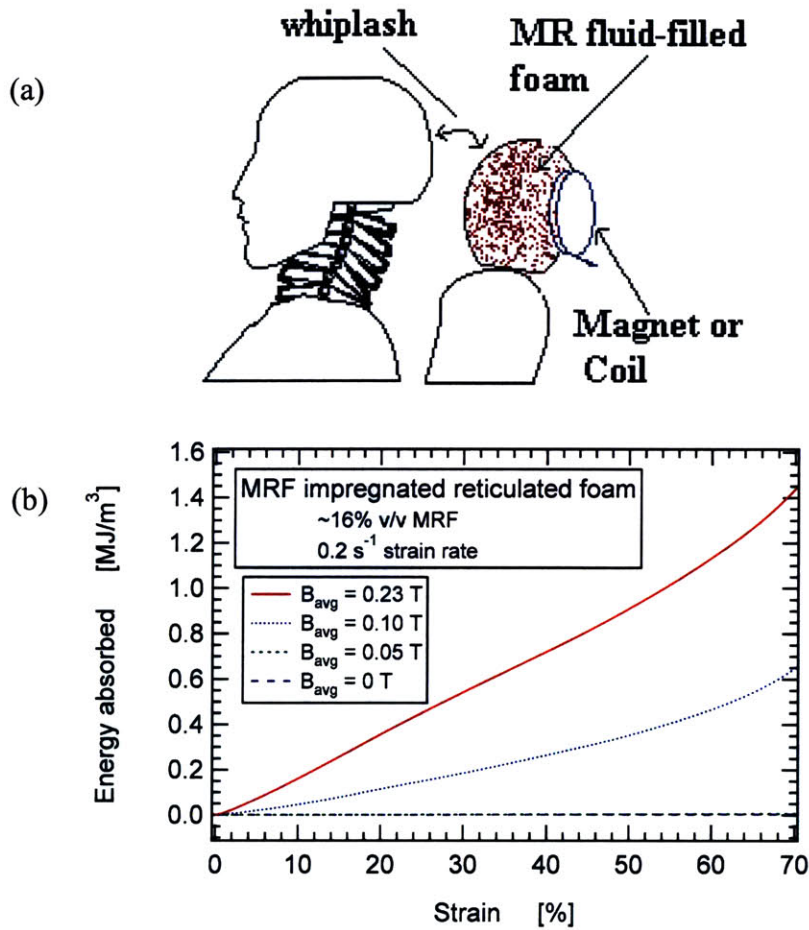


Figure 6.1 (a) Illustration of a MR fluid impregnated headrest in an automobile to satisfy the NIC requirement and prevent whiplash-associated disorders (WAD). (b) Energy absorbed per unit volume by MR fluid impregnated foam at different magnetic fields.

An important consideration for this or any other application is the rapid generation of a strong magnetic field for active energy absorption. The field can be created normal to or along the direction of the impact. An inexpensive, simple but highly effective way of realizing this is by the use of a permanent magnet. It can be used in circuit with magnetically permeable parts so that the field lines are concentrated and directed through the energy absorbing material during an impact. The magnetic field decays inversely to the square of the distance which implies that the magnet in

a facing-away orientation would have a negligible field and can simply be rotated or oriented so as to concentrate field lines in the material during impact conditions as shown in figure 6.2.

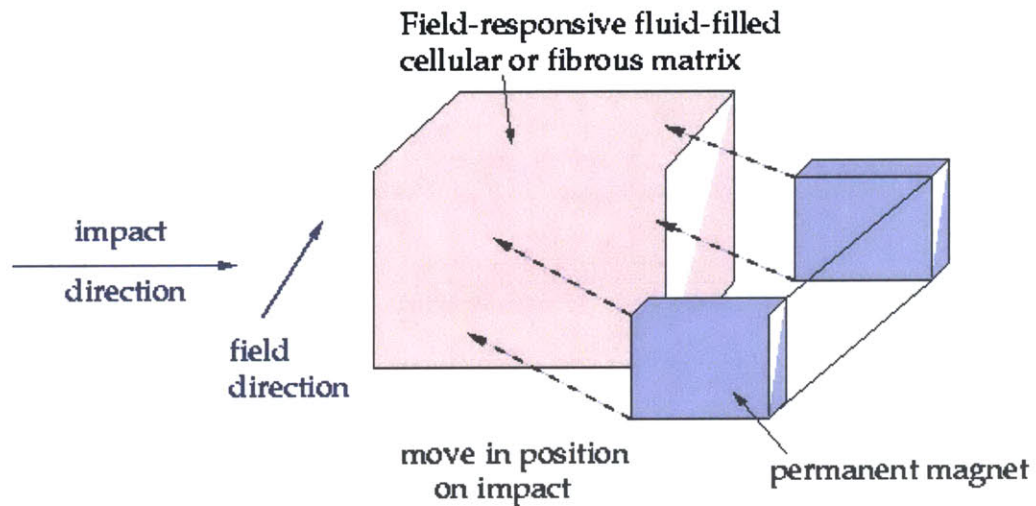


Figure 6.2 An embodiment for inexpensive generation of magnetic field near a headrest using a permanent magnet.

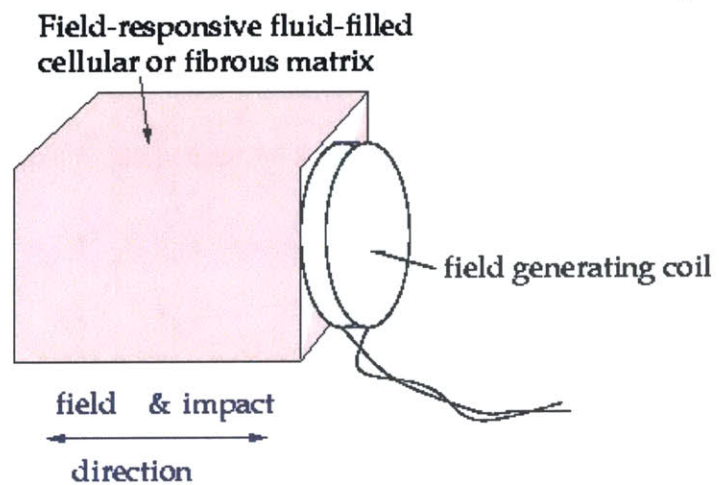


Figure 6.3 An embodiment of a variable field-generating device, using a coil and associated circuitry that are aligned in the direction of the impact.

A magnet coil can also be used to generate a varying magnetic field, and hence resulting variable energy absorption in a MR fluid-filled matrix as shown in figure 6.3. Preferably, the coil is placed such that the line of action of impact is along the decreasing magnetic field direction, since work done against the ponderomotive force, discussed earlier in chapter 5 (equation 5.10) enhances the amount of energy absorption. The ponderomotive force and the associated energy absorption increase as the magnetic field strength ( $B$ ) or the magnetic field gradient ( $dB/dz$ ) increases. A transistor or a SCR (semiconductor-diode capacitor resistor) circuit can be used to send a high current pulse through the coil for short times, which is particularly useful in case of a vehicle crash, since the time of the event is 150-200 milliseconds but a high amount of energy absorption is required in this small time.

### **6.3 Impact Testing: Drop Ball Test Apparatus**

Experimentation using ‘low’ strain rate ( $10^{-8}$  to  $10^{-2}$  /s) testing equipment such as the Texture Analyzer, has been discussed in chapter 5 with an accompanying scaling model. However, real-time testing at ‘intermediate’ strain rates ( $10^{-2}$  to 40 /s) that are usually seen in automobile impacts is essential. These strain rates are simulated in the laboratory using drop-hammer, drop ball, izod impact or high-speed servo-hydraulic tests (Gibson and Ashby, 1997; Robinovitch *et al.*, 1995; Larson *et al.*, 1996).

A ‘drop-ball’ test apparatus has been custom-built in the laboratory for simulating auto design impacts and is shown in figure 6.4. The experimental technique consists of dropping a guided ball from a variable height through a guide rail onto the middle of a specimen and measuring the velocity, acceleration and the amount of energy absorbed. A clear acrylic tube has been used as the guide rail and sleeve for the sample in order to allow easy visualization. A high-speed video camera (Phantom v5.0, Vision Research Inc.) connected to a computer has been used to record the impact of the ball on the sample at 1900 frames per second.

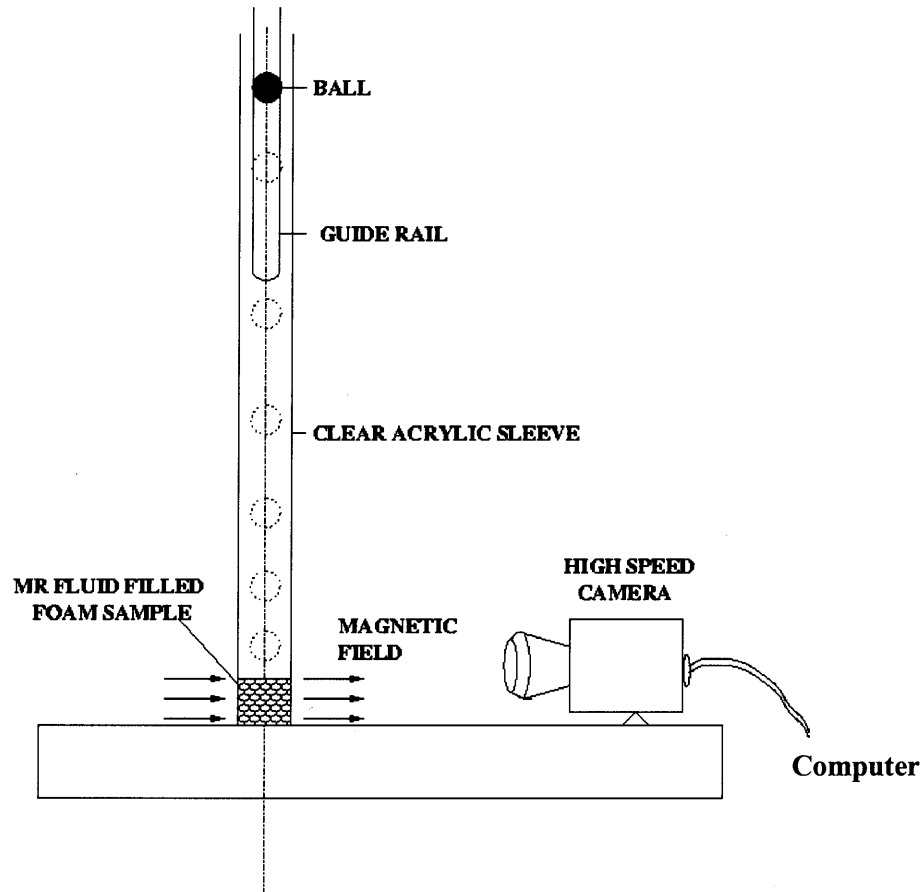


Figure 6.4 Custom-built 'Drop ball' test apparatus with an associated high-speed camera for real-time impact testing.

Experiments using the 'drop-ball' test apparatus have been carried out for a scaled down headrest. The energy absorbed by the impregnated headrest ( $W$ ) is a function of a number of parameters depending on the initial impact energy, foam structural and mechanical properties and dimensions of the head model.

$$W = f^n \left( E_i, d, t, \phi_f, B_{avg}, \left( \frac{\rho^*}{\rho_s} \right) \right) \quad (1.2)$$

where  $E_i$  is the kinetic energy of the head model before impact,  $d$  is the characteristic diameter of the head model,  $t$  is the thickness of the foam,  $\phi_f$  is the volume fraction of the fluid

impregnating the foam,  $B_{avg}$  is the magnetic field applied and  $\rho^*/\rho_s$  is the relative density of foam. The MR fluid-impregnated foam parameters are however interdependent and can be expressed in terms of the plateau stress ( $\sigma^*$ ) as described in equation 5.8. Dimensional analysis for the amount of energy absorbed then gives

$$\left(\frac{W}{E_i}\right) = f^n \left( \left(\frac{d}{t}\right), \left(\frac{\sigma^*}{\sigma^*_{dry}}\right) \right) \quad (1.3)$$

where  $(W/E_i)$  is the fraction of impact energy absorbed or in related terms the coefficient of restitution  $e$  which gives a feel of the unabsorbed fraction of impact energy and  $(\sigma^*/\sigma^*_{dry})$  characterizes the impregnated foam parameters.

The adult head impact on a car headrest during a rear-end crash has been scaled down while maintaining geometric and kinematic similarity. Thus, an average human head that weighs around 4.5-5.0 kg with a characteristic diameter of 165 mm (Jacobsson *et al.*, 2000) has been scaled down to a 0.5 inches Aluminum ball with a weight of 3.0 grams. The dimensions of the magnetorheological fluid-filled cylindrical sample used, 1.5 inches diameter and 0.75 inches height, is a scale down from a car headrest such that the initial impact energy per unit volume is the same for dynamic similarity.

$$\begin{aligned} W^m &= \frac{1}{2} \frac{mv^2}{At} \\ W^m_{actual} &= \frac{1}{2} \frac{4.5v^2}{\pi (0.0825)^2 0.17} = 619v^2 \\ W^m_{drop-ball} &= \frac{1}{2} \frac{0.003v^2}{\pi (0.00635)^2 0.01905} = 621v^2 \end{aligned} \quad (1.4)$$

where  $W^m$  is the impact energy per unit volume,  $m$  is the mass of the head,  $v$  is the impact velocity,  $A$  is the area of contact between the head and the headrest and  $t$  is the thickness of the foam.

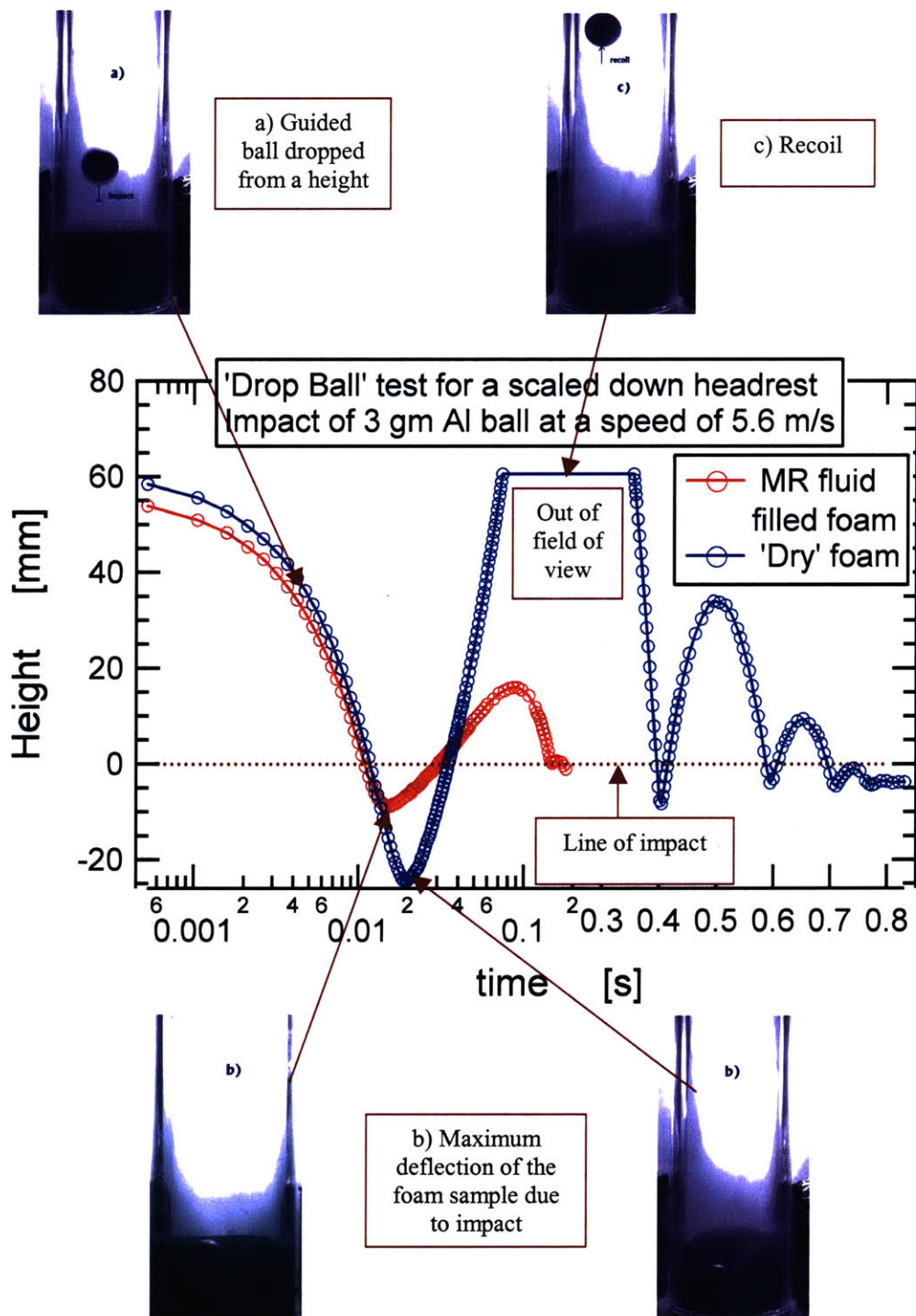


Figure 6.5 Real-time impact testing of a geometrically scaled adult headform onto a car headrest using a 'Drop ball' test apparatus.

The ball is dropped from an average height of 1.5 m and impacts at an average velocity of 5.3 m/s (~20 kmph) which is the maximum velocity used in automobile rear-end crash design. An average magnetic field strength ( $B_{avg}$ ) of 0.15 Tesla is applied to the foam sample that is impregnated with MR fluid at 35% volume fraction. The ball motion against time is plotted in figure 6.5 with corresponding image captures at maximum deflection and recoil positions. The figure shows the initial 300 ms in log scale to bring out the features on impact and is presented on a linear scale for later times. The origin (represented as the line of impact in the figure) is taken to be the top of the foam sample so that the maximum deflection of the scaled headrests can be compared. The maximum compression of the foam would correspond to the relative movement between the neck and the head in an actual crash and needs to be minimized. While the MR fluid-filled foam shows only 30% compression, the 'dry' foam sample 'bottoms out' with ~ 100% compression on impact. The rebound velocity is 1.72 m/s for the unfilled foam sample as compared to 0.5 m/s for the MR fluid filled foam sample. The rebound velocity corresponds to the forward rebound of the passenger into the seat belt in an actual rear-end crash which is a vital consideration for whiplash injury minimization (Jakobsson *et al.*, 2000). The coefficient of restitution  $e$  is 0.1 for the MR fluid filled foam as compared to 0.32 for the unfilled foam even at more than three times the maximum deflection. Also, the time when the ball finally comes to rest is 800 ms for the 'dry' foam sample as compared to 150 ms for the MR fluid filled foam sample. All these comparisons prove in principle the effectiveness of using a field-responsive fluid impregnated headrest for protection of passengers in a rear-end impact

## **6.4 Automotive energy management structures**

A number of automotive components, such as the A/B/C pillar trims, knee bolster, bumpers, head-liners and side-impact parts, are also required by the new legislations to absorb energy 'smartly' so as to cause minimum injury to adult and child occupants and passengers alike. Similar to the adaptive headrest to protect from whiplash, these structures can be



impregnated with field-responsive fluids and controlled to have desired energy management. As an example, a knee bolster is required to absorb varying amounts of energy ranging from 100 to 1000 J depending on the occupant and structures similar to those shown earlier in figures 6.2 and 6.3 can be suitably packaged to give required energy absorption capacities.

A piston-cylinder arrangement can also be used to house the field-responsive fluid-filled matrix, wherein energy is absorbed as the impact pushes the piston compressing the composite material. Further for MR fluids, the magnetic field-generating device, can be housed within the piston or the cylinder so that the field lines travel through the fluid-filled matrix. Various energy absorbing structure designs using a piston-cylinder type arrangement and magnetic coils or permanent magnets are shown in figure 6.6. The viscous dissipation due to flow of the fluid through orifices or holes in the piston-cylinder arrangement adds to the energy absorption due to the fluid flow inside the solid or fibrous network as shown in figure 6.6 b). In figure 6.6 c) permanent magnets are placed in the cylinder housing such that compression of the material would give enhanced energy absorption due to an increasing field as the magnets are pushed closer. Also, if the arrangement of magnets is such that a repulsive force is exerted on bringing the magnets closer, the impactor would experience an additional stress thus giving a large dynamic range of energy absorption. As shown in figure 6.6 d) a series of coils can be used in place of the permanent magnets so that compression would decrease the distance between the coils leading to enhanced energy absorption from the increased field strength and higher repulsive force. Thus, a variety of field generating devices can be designed depending on the application structure and requirements.

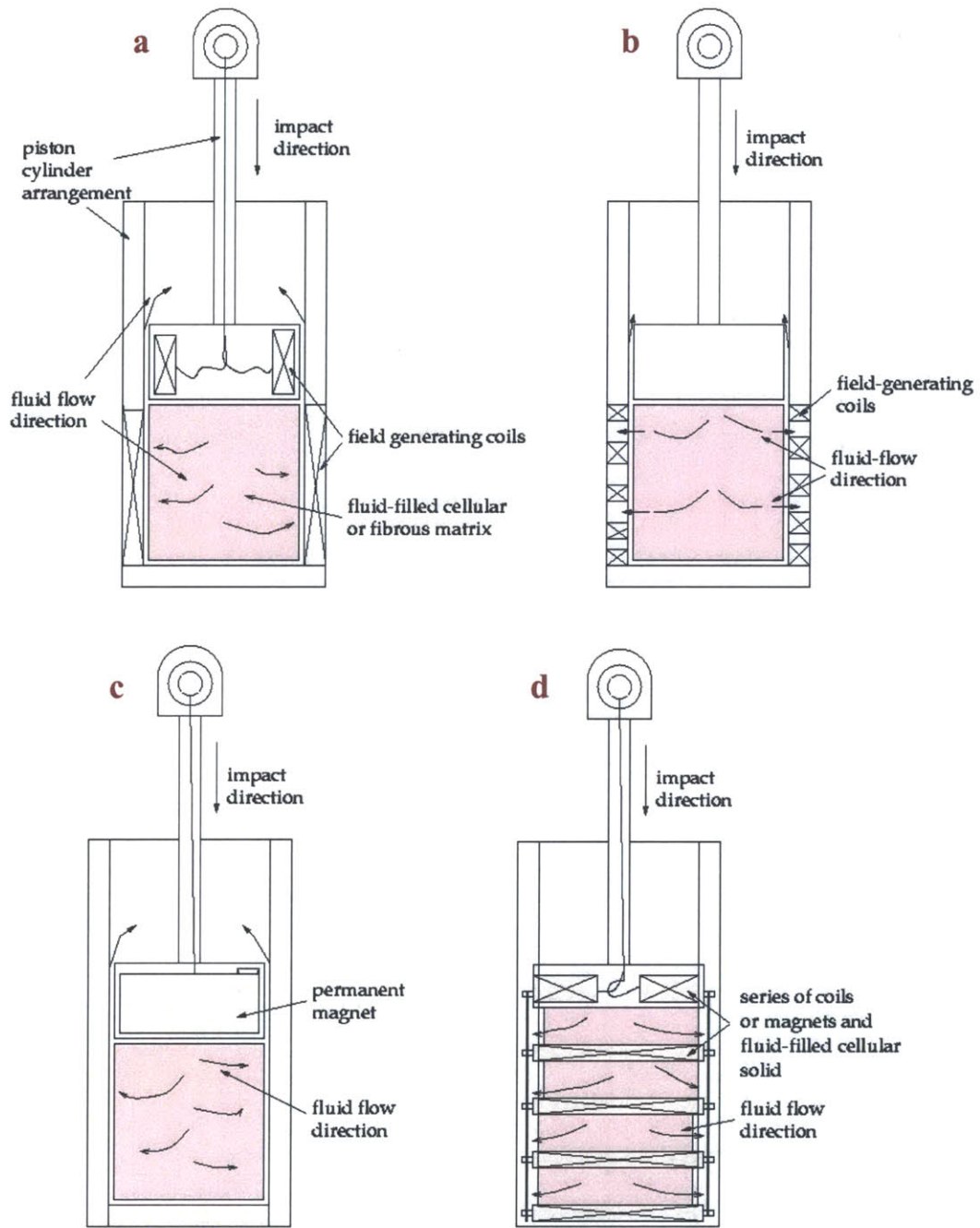


Figure 6.6 Various embodiments of a piston-cylinder arrangement used for controllable energy absorption.

## **6.5 Summary**

New incoming legislations present a 'conflict of stiffness' problem in a number of automotive components that can possibly be dealt with by use of a field-responsive fluid impregnated cellular solid. An exemplary application of this composite is the car headrest that can be converted from a soft, compliant foam into a rigid, energy absorbing material during a rear-end crash so as to protect the occupant from whiplash injuries. A 'Drop ball test' apparatus has been built and material testing at realistic impact conditions has been carried out. Dimensional analysis of impact energy absorbed forms the basis for scaling down the head and the headrest while maintaining geometric and dynamic similarity. The maximum deflection of the foam has been found to decrease to a third (30%) while the coefficient of restitution decreases to 0.1 for the scaled down headrest when impregnated with a MR fluid. Finally, various embodiments of energy management structures using permanent magnets or field coils depending on the application constraints have been discussed in the chapter.

# CHAPTER 7

## Conclusions and Future Work

### **7.1 Conclusions**

Energy management is a vital concern for automobiles and a number of components are required to be occupant and pedestrian ‘safe’ according to new standards and legislations (FMVSS 201/202, EEVC WG 17). These requirements usually conflict with passenger and design demands of thin, more compliant and comfortable materials. Also, energy absorption criteria vary depending on whether the occupant is an adult or a child. A ‘novel’ energy absorbing material which provides the automotive industry with a solution to this ‘conflict of stiffness’ problem has been conceptualized, designed and tested in this work. The material consists of a cellular solid or a fibrous matrix impregnated with a field-responsive fluid like a magnetorheological (MR) fluid. This fluid-solid composite has magnetic-field-dependent energy absorption and stiffness and can be user-controlled in tune with the application requirements.

Field-responsive fluids undergo large changes in rheological properties in the presence of a field. In particular, magnetorheological fluids have a magnetic-field-dependent yield stress (stress at which appreciable deformation takes place without any appreciable change in stress). Rheological properties, models and applications of field-responsive fluids’ (FRFs) have been reviewed in chapter 2. MR fluids have had a lot of commercial success in damping applications and these have also been studied extensively (refer to sections 2.1.3 to 2.1.7). In spite of commercial usage these fluids have limitations in terms of cost and stability against gravitational forces. Hence, a cheap MR fluid with excellent stability w.r.t. sedimentation has been synthesized in our laboratory (figure 4.6). A viscoplastic grease-like base has been added to the fluid to

provide a low yield stress in the field off-state and to prevent the particles from settling (equation 4.3).

Steady shear rheological experiments and transient creep tests have been performed on both the laboratory synthesized and other commercially available fluids using the TA Instruments' AR 1000/ 2000 rheometers with a custom-built fixture. The fixture has been designed and built to generate a magnetic field of 0.0 to 0.4 Tesla in the fluid sample space between the top and the bottom plates (figure 4.2). It consists of a magnetic coil with 1300 turns and a steel housing and can support a maximum current of 3.0 Amperes without the use of a cooling water system (figure 4.1). The in-house formulated MR fluid has been found to have a field-dependent yield stress (as an example, ~2 kPa at 0.09 Tesla and ~20 kPa at 0.33 Tesla), which is comparable to other commercial and research stage fluids (figure 4.10). Creep tests have provided us with useful information on the time response of the fluids, which varies from 3-15 ms depending on the magnetic field and the applied stress (figure 4.11). Also, experimental data suggests a dependence of the total strain on the scaled stress  $(\sigma/\sigma_y)$ . These large, reversible and fast changes in the rheological properties have been utilized to modulate the energy-absorbing properties of a cellular solid.

Shear-thickening fluids (STF), a class of field-responsive fluids with a shear-rate dependent viscosity, have also been reviewed extensively in chapter 2 with emphasis on parameters controlling this critical point behavior and also challenges foreseen in using these STFs as a cheap alternative to MR fluids filling the cellular solid. An inexpensive shear-thickening fluid consisting of corn-starch in water suspension (56% w/w) has been studied under steady shear and creep flow. The fluid shows a 2-3 orders of magnitude jump in viscosity at a critical shear rate or stress, which can possibly be controlled by varying different parameters like particle size, phase volume and particle size distribution (figure 4.13). Normal stress difference measurements also show instability at the critical stress after which it monotonically increases

(figure 4.14). However, 'rheopexy' or increasing viscosity over long periods of time undermine the utility of this particular system as a spontaneously responding, cheap substitute to MR fluids filling the cellular solids.

Cellular solids, i.e. porous interconnected networks of solid material forming edges and faces of cells, have a variety of uses, high impact energy absorption being one of them. The cell structure, mechanical properties, energy absorption curves and applications of cellular solids have been reviewed in chapter 3. The properties of 'dry' foam in which only air fills the pores serve as a standard for characterization of field-responsive fluid impregnated cellular solids. The mechanical properties of reticulated (open-cell) foams have also been tested in our laboratory using the Texture Analyzer (TA.XT2i), a programmable 'low' strain rate ( $10^{-8}$  to  $10^{-2}$ ) testing instrument and compared with data from the literature. A piston-cylinder rig has been built for the Texture Analyzer in order to test fluid-filled foams (figure 5.1). The fixture spatially constrains the sample in space and directs the flow of fluid along the impact direction.

The foams are impregnated with the field-responsive fluid by repeated compression and relaxation to ensure spatial homogenization of the fluid. Foams filled with glycerol, a Newtonian fluid, show no appreciable change in the plateau region of the stress-strain curve (figure 5.4). The densification strain however depends on the volume fraction of the fluid impregnating the foam and shifts to a lower value as the volume fraction increases. The densification strain has been found to be a function of the total free volume available for compression, i.e. total volume minus the solid and fluid volume. Magnetorheological (MR) fluid-impregnated foams, on the other hand, show a strong dependence of the plateau stress on the magnetic field. It is proposed that a fraction of the MR fluid forms a secondary layer covering the solid edges of the foam due to the presence of a yield-stress. This proposition has been corroborated by optical micrographs of fluid impregnated foams (figure 5.8). The elastic modulus of the composite cell edge is thus a function of the magnetic field dependent yield stress. The plateau stress hence increases dramatically as the yield stress increases with the magnetic field and energy absorbed per unit volume (calculated

as the area under the stress-strain curve) has been found to increase, at moderate magnetic fields ( $B \approx 0.2$  T), by 30-50 times compared to the energy absorbed at zero-field (figure 5.11). The energy absorption capacity of this fluid-solid composite can thus be modulated from 1 to 50 times by varying the magnetic field from 0 to 0.2 Tesla. Magnetic field gradients have been observed to play an important role in controlling the extent of energy absorption: an additional force known as the ponderomotive magnetic force is exerted when the fluid-filled composite is compressed in the direction of decreasing magnetic field. The volume fraction of MR fluid impregnating the foam determines the densification strain, which scales with the free volume available for compression (figure 5.14). Experiments to characterize the mechanical properties of fluid-filled foams as a function of these control parameters have been carried out by varying the magnetic field strength from 0.0 to 0.25 Tesla and varying the volume fraction from 0 to 60% at each of these field strengths. Also, the strain rate imposed in experiments has been varied from 0.02 to 2  $s^{-1}$  to study its effect on the properties of fluid-filled foams (figure 5.16). The strain rate-dependence has been found to be minimal though at impact strain rates these properties could appreciably change.

A scaling model, in the spirit of the model developed by Gibson and Ashby (1997) for 'dry' foams has been proposed (equation 5.10). The model is based on the assumption that the elastic modulus of the solid cell edge changes depending on the magnetic field strength and the fraction of MR fluid forming a secondary layer on it (equation 5.7). The cell structural parameters, mainly the thickness of the cell edge and hence the relative density, change with the volume fraction, which in turn affect the plateau modulus (equation 5.8). All experimental data for different control parameters, magnetic field strength and gradient, volume fraction and strain rate can be collapsed onto a single master curve (figure 5.20) using appropriate shift factors. The design curve can be used to optimize the energy absorption needed to satisfy the application requirements.

A 'Drop Ball' test apparatus has been custom-built for real-time impact testing. A high-speed video camera records the impact event and testing up to speeds of ~20 kmph has been carried out. Designs for various automotive components such as the headrest, pillar trims, knee bolsters, side impact parts have been presented. An impact-absorbing headrest that is soft and comfortable to use under normal driving conditions but becomes rigid enough to absorb large amounts of kinetic energy during a crash has been described in detail (figure 6.1). Magnetic field generation presents many challenges for the headrest and other applications due to additional cost, bulk and design issues and various designs using permanent magnets or field coils to obtain high fields for impact times (milliseconds) have been discussed to overcome these problems (figure 6.2; figure 6.3). A scaled down field-responsive fluid-filled headrest, based on geometric and kinematic similarity, has been proved in principle to be more effective than the present headrest for minimization of crash injuries.

## **7.2 Future Work**

Stable and inexpensive magnetorheological fluids have been synthesized but improving the yield stress response would go a long way in improving the feasibility of many other applications. MR fluids with larger constituent particles are expected to improve this response and stable fluids need to be formulated and characterized as discussed in detail in section 4.1.2.2. An in-depth study of the MR fluid response in creep and oscillatory flow could further our understanding of the field-induced dipolar chain-structure formation and convolution in field-responsive fluids. Synthetic shear-thickening fluids with good stability and extreme viscosity changes could provide a cheap alternative to MR fluids in impact absorbing applications and more research work is required in this direction.

Field-responsive fluid-filled cellular solids have adaptive stiffness, energy absorption and a number of applications that need to be conformable but respond to environmental conditions, for example ballistic armor, could be made feasible with future research. In-depth studies to



examine the effects of the cellular structure by use of different open and closed-cell foams could also be performed in the future. Auxetic foams i.e. foams that have a negative Poisson's ratio and expand in all directions on compression, can possibly enhance the energy absorption gain obtained from fluid impregnation and require an in-depth study. Magnetic field generation presents many challenges and improvements in design and magnetic field strength would prove beneficial. Future research initiatives in actual prototype development and testing in simulated car crashes would prove advantageous in commercialization of prospective designs.

## Bibliography

- Barnes, H. A. "Shear-Thickening (Dilatancy) in Suspensions of Nonaggregating Solid Particles Dispersed in Newtonian Liquids." *Journal of Rheology* **33**(2): 329-366 (1989).
- Barnes, H. A. "The yield stress - a review or 'παντα ρει' - everything flows?" *Journal of Non-Newtonian Fluid Mechanics* **81**(1-2): 133-178 (1999).
- Bender, J. and Wagner, N. J. "Reversible shear thickening in monodisperse and bidisperse colloidal dispersions." *Journal of Rheology* **40**(5): 899-916 (1996).
- Bird, R. B., Stewart, W. E. and Lightfoot, E. N. "Transport Phenomena", John Wiley and Sons. (1987).
- Boersma, W. H., Laven, J. and Stein, H. N. "Shear Thickening (Dilatancy) in Concentrated Dispersions." *AIChE Journal* **36**(3): 321-332 (1990).
- Boersma, W. H., Baets, P. J. M., Laven J. and Stein, H. N. "Time-Dependent Behavior and Wall Slip in Concentrated Shear Thickening Dispersions." *Journal of Rheology* **35**(6): 1093-1120 (1991).
- Boersma, W. H., Laven, J. and Stein, H. N. "Viscoelastic Properties of Concentrated Shear-Thickening Dispersions." *Journal of Colloid and Interface Science* **149**(1): 10-22 (1992).
- Bostrom, O., Fredriksson, R., Haland, Y., Jakobsson, L., Krafft, M., Lovsund, P., Muser, M. H. and Svensson, M. Y. "Comparison of car seats in low speed rear-end impacts using the BioRID dummy and the new neck injury criterion (NIC)." *Accid Anal Prev* **32**(2): 321-328 (2000).
- Brady, J. F. and Bossis, G. "Stokesian Dynamics." *Annual Review of Fluid Mechanics* **10**(4-5): 555-569 (2000).
- Carlson, J. D. "Low-cost MR fluid sponge devices." *Journal of Intelligent Material Systems and Structures* **10**(8): 589-594 (1999).

- Carlson, J. D. and Jolly, M. R. "MR fluid, foam and elastomer devices." *Mechatronics* **10**(4-5): 555-569 (2000).
- Carlson, J. D. (2001). "What makes a good MR fluid". 8th International Conference on Electrorheological (ER) Fluids and Magnetorheological (MR) Suspensions., Nice, France.
- Carriere, C. J. "Network development during shear-thickening in semi-dilute solutions of gently solubilized starches." *Journal of Polymer Science Part B-Polymer Physics* **36**(12): 2085-2093 (1998).
- Chin, B. D., Park, J. H., Kwon, M. H. and Park, O. O. "Rheological properties and dispersion stability of magnetorheological (MR) suspensions." *Rheologica Acta* **40**(3): 211-219 (2001).
- Chow, M. K. and Zukoski, C. F. "Gap-size and shear history dependencies in shear thickening of a suspension ordered at rest." *Journal of Rheology* **39**(1): 15-32 (1995).
- Chrzan, M. J. and Carlson, J. D. "MR Fluid Sponge Devices and Their Use in Vibration Control of Washing Machines." *Proceedings of the 8<sup>th</sup> Annual Symposium on Smart Structures and Materials* Newport Beach, CA (2001).
- Courtney, W. A. "Improved elastomeric impact absorber with viscous damping". **WO9949236** (1999).
- Courtney, W. A. and S. O. Oyadiji "Preliminary investigations into the mechanical properties of a novel shock absorbing elastomeric composite." *Journal of Materials Processing Technology* **119**(1-3): 379-386 (2001).
- Cutillas, S., Bossis, G. and Cebers, A. "Flow-induced transition from cylindrical to layered patterns in magnetorheological suspensions." *Physical Review E* **57**(1): 804-811 (1998).
- Davis, L. C. "Model of magnetorheological elastomers." *Journal of Applied Physics* **85**(6): 3348-3351 (1999).

- de Gans, B. J., Hoekstra, H. and Mellema, J. "Non-linear magnetorheological behaviour of an inverse ferrofluid." *Faraday Discussions*(112): 209-224 (1999).
- Dunger, U., Weber, H. and Buggisch, H. "A simple model for a fluid-filled open-cell foam." *Transport in Porous Media* **34**(1-3): 269-284 (1999).
- Dyke, S. J., Spencer, B. F., Sain, M. K. and Carlson, J. D. "An experimental study of MR dampers for seismic protection." *Smart Materials & Structures* **7**(5): 693-703 (1998).
- Eastwood, A. R. and H. A. Barnes "Superposition of Oscillatory on Steady Shear for Non-Newtonian Suspensions." *Rheologica Acta* **14**(9): 795-800 (1975).
- Fermigier, M. and Gast, A. P. "Structure evolution in a paramagnetic latex suspension." *Journal of Colloid and Interface Science* **154**(2): 522-539 (1992).
- Frith, W. J. and Lips, A. "The Rheology of Concentrated Suspensions of Deformable Particles." *Advances in Colloid and Interface Science* **61**: 161-189 (1995).
- Gast, A. P. and Zukoski, C. F. "Electrorheological Fluids as colloidal suspensions." *Advances in Colloid And Interface Science* **30**(3-4): 153-202 (1989).
- Genc, S. and Phule, P. P. "Rheological properties of magnetorheological fluids." *Smart Materials & Structures* **11**(1): 140-146 (2002).
- Gibson, L. J. and Ashby, M. F. "Cellular solids : structure and properties". Cambridge [England]; New York, Cambridge University Press (1997).
- Goldsmith, W. and Sackman, J. L. "An experimental study of energy absorption in impact on sandwich plates." *International Journal of Impact Engineering* **12**(2): 241-262.(1992).
- Gooding, E. "Adaptive, energy absorbing structure". US **5915819** (1999).
- Gotoh, M., Yamashita, M. and Kawakita, A. "Crush behavior of honeycomb structure impacted by drop-hammer and its numerical analysis." *Materials Science Research International* **2**(4): 261-266 (1996).

- Green, R. G. and Griskey, R. G. "Rheological Behavior of Dilatant (Shear-thickening) Fluids. Part I. Experimental and Data." *Transactions of the Society of Rheology* **12**(1): 13-25 (1968).
- Hayes, W. C., Robinovitch, S. N. and McMahon, T. A. "Bone fracture prevention method". US **5545128 A** (1996).
- Head, D. A., Ajdari, A. and Cates, M. E. "Rheological instability in a simple shear-thickening model." *Europhysics Letters* **57**(1): 120-126 (2002).
- Hoffman, R. L. "Discontinuous and Dilatant viscosity behavior in concentrated suspensions. I. Observation of a flow instability." *Transactions of the Society of Rheology* **16**(1): 155-173 (1972).
- Hoffman, R. L. "Discontinuous and Dilatant Viscosity Behavior in Concentrated Suspensions .3. Necessary Conditions for Their Occurrence in Viscometric Flows." *Advances in Colloid and Interface Science* **17**(AUG): 161-184 (1982).
- Jakobsson, L., Lundell, B., Norin, H. and Isaksson-Hellman, I. "WHIPS--Volvo's Whiplash Protection Study." *Accid Anal Prev* **32**(2): 307-19 (2000).
- Jolly, M. R., Carlson, J. D. and Munoz, B. C. "A model of the behaviour of magnetorheological materials." *Smart Materials & Structures* **5**(5): 607-614 (1996).
- Jolly, M. R., Bender, J. W. and Carlson, J. D. "Properties and applications of commercial magnetorheological fluids." *Journal of Intelligent Material Systems and Structures* **10**(1): 5-13 (1999).
- Kanianthra, J. N. "Side impact energy absorber". US **5564535** (1996).
- Kormann, C., Laun, H. M. and Richter, H. J. "MR fluids with nano-sized magnetic particles" *Int. J. Mod. Phys. B* **10**(23-24): 3167-3172 (1996).
- Klempner, D. and Frisch, K. C. "Handbook of polymeric foams and foam technology." Oxford University Press. (1991).

- Klingenberg, D. J. "Magnetorheology: Applications and challenges." *AICHE Journal* **47**(2): 246-249 (2001).
- Larson, R. G., Goyal, S. and Aloisio, C. " A predictive model for impact response of viscoelastic polymers in drop tests." *Rheologica Acta* **35**(3): 252-264 (1996).
- Larson, R. G. "The Structure and Rheology of Complex Fluids", Oxford University Press. (1999).
- Laun, H. M., Bung, R. and Schmidt, F. "Rheology of Extremely Shear Thickening Polymer Dispersions (Passively Viscosity Switching Fluids)." *Journal of Rheology* **35**(6): 999-1034 (1991).
- Laun, H. M. "Normal Stresses in Extremely Shear Thickening Polymer Dispersions." *Journal of Non-Newtonian Fluid Mechanics* **54**: 87-108 (1994).
- Lee, Y. S. and Wagner, N. J. "Dynamic properties of shear thickening colloidal suspensions." *Rheologica Acta* **42**(3): 199-208 (2003).
- Lemaire, E., Meunier, A. and Bossis, G. "Influence of the Particle-Size on the Rheology of Magnetorheological Fluids." *Journal of Rheology* **39**(5): 1011-1020 (1995).
- Li, W. H., Chen, G. and Yeo, S. H. "Viscoelastic properties of MR fluids." *Smart Materials & Structures* **8**(4): 460-468 (1999).
- Li, W. H., Yao, G. Z., Chen, G., Yeo, S. H. and Yap, F. F. "Testing and steady state modeling of a linear MR damper under sinusoidal loading." *Smart Materials & Structures* **9**(1): 95-102 (2000).
- Li, W. H., Du, H., Chen, G. and Yeo, S. H. "Nonlinear rheological behavior of magnetorheological fluids: step-strain experiments." *Smart Materials & Structures* **11**(2): 209-217 (2002).
- Linder, A. "A new mathematical neck model for a low-velocity rear-end impact dummy: evaluation of components influencing head kinematics." *Accid Anal Prev* **32**(2): 261-269 (2000).

- Lopatnikov, S. and A. H. D. Cheng "A thermodynamically consistent formulation of magnetoporoelasticity." *International Journal of Solids and Structures* **35**(34-35): 4637-4657 (1998).
- Lopatnikov, S. L. "Dynamic equations of the new materials: Porous media saturated with ferromagnetic or electrorheological liquids." *Doklady Akademii Nauk* **360**(5): 637-639 (1998).
- Maiti, S. K., Ashby M. F. and Gibson, L. J. " Fracture-toughness of brittle cellular solids." *Scripta Metallurgica* **18**(3): 213-217 (1984).
- Park, J. H., Kwon, M. H. and Park, O. O. "Rheological properties and stability of magnetorheological fluids using viscoelastic medium and nanoadditives." *Korean J. Chem. Eng.* **18**(5): 580-585 (2001).
- Parthasarathy, M. and D. J. Klingenberg "Electrorheology: Mechanisms and models." *Materials Science & Engineering R-Reports* **17**(2): 57-103 (1996).
- Pearson, J. R. A. and P. M. J. Tardy "Models for flow of non-Newtonian and complex fluids through porous media." *Journal of Non-Newtonian Fluid Mechanics* **102**(2): 447-473 (2002).
- Phule, P. P. "Magnetorheological Fluid". **US 5985168A** (1999).
- Phule, P. P. and Ginder, J. M. "Synthesis and properties of novel magnetorheological fluids having improved stability and redispersibility." *Int. J. Mod. Phys. B* **13**(14-16): 2019-2027 (1999).
- Raghavan, S. R. and S. A. Khan "Shear-thickening response of fumed silica suspensions under steady and oscillatory shear." *Journal of Colloid and Interface Science* **185**(1): 57-67 (1997).
- Rankin, P. J., A. T. Horvath, et al. "Magnetorheology in viscoplastic media." *Rheologica Acta* **38**(5): 471-477 (1999).

- Rosenfeld, N., Wereley, N. M., Radakrishnan, R., et al. "Behavior of magnetorheological fluids utilizing nanopowder iron *Int. J. Mod. Phys. B* **16**(17-18): 2392-2398 (2002).
- Sandrin, G. and J. D. Carlson "Controllable device having a matrix medium retaining structure". **US 6202806 B1** (2001).
- Spencer, B. F., Dyke, S. J., Sain, M. K. and Carlson, J. D. "Phenomenological model for magnetorheological dampers." *Journal of Engineering Mechanics-ASCE* **123**(3): 230-238 (1997).
- Svensson, M. Y., Lovsund, P., Haland, Y. and Larsson, S. "The influence of seat-back and head-restraint properties on the head-neck motion during rear-impact." *Accid Anal Prev* **28**(2): 221-227 (1996).
- Tang, X., Zhang, X., Tao, R. and Rong, Y. "Structure-enhanced yield stress of magnetorheological fluids." *Journal of Applied Physics* **87**(5): 2634-2638 (2000).
- Tattiyakul, J. and M. A. Rao "Rheological behavior of cross-linked waxy maize starch dispersions during and after heating." *Carbohydrate Polymers* **43**(3): 215-222 (2000).
- Ullrich, M. "Caught between the constraints of interior design and safety." *IVehE* 26-27 (2003).
- Van Egmond J. W. "Shear-thickening in suspensions, associating polymers, worm-like micelles, and poor polymer solutions." *Current Opinion in Colloid & Interface Science* **3**(4): 385-390 (1998).
- Wang, J. and G. Meng "Magnetorheological fluid devices: principles, characteristics and applications in mechanical engineering." *Proceedings of the Institution of Mechanical Engineers Part L- Journal of Materials-Design and Applications* **215**(L3): 165-174 (2001).
- Warner, M., Thiel, B. L. and Donald, A. M. "The elasticity and failure of fluid-filled cellular solids: Theory and experiment." *Proceedings of the National Academy of Sciences of the United States of America* **97**(4): 1370-1375 (2000).
- Weaire, D. L. and Hutzler, S. "The physics of foams", Oxford University Press (1999).



- Weiss, K. D., Carlson, J. D. and Nixon, D. A. "Viscoelastic Properties of Magnetorheological and Electrorheological Fluids." *Journal of Intelligent Material Systems and Structures* **5**(6): 772-775 (1994).
- Welcher, J. B. and T. J. Szabo "Relationships between seat properties and human subject kinematics in rear impact tests." *Accid Anal Prev* **33**(3): 289-304 (2001).
- Yang, G., Spencer, B. F., Carlson, J. D. and Sain, M. K. "Large-scale MR fluid dampers: modeling and dynamic performance considerations." *Engineering Structures* **24**(3): 309-323 (2002).
- Young, B. O. "Liquid shock absorbing buffer". US **3672657** (1972).